FIRST-PRINCIPLES QUANTUM TRANSPORT IN 2D MATERIALS FOR NANOELECTRONICS

Thèse présentée en vue de l'obtention du grade de Docteur en Sciences de l'Ingénieur

SAMUEL DECHAMPS

SUPERVISOR:

Prof. Jean-Christophe Charlier

MEMBERS OF THE JURY:

Prof. David Beljonne
Prof. Philippe Dollfus
Prof. Benoit Hackens (secretary)
Dr. Viet-Hung Nguyen
Prof. Xavier Urbain (chairman)

UCLouvain
Institute of Condensed Matter and Nanosciences

February 2022

ABSTRACT

Over the past decades, continued improvement in transistors density, performance and energy efficiency have been sustained by technological innovations. This exponential development predicted by Moore in the 60s transformed the first crude computers from the 70s into the ubiquitous and high-performance sophisticated machines of nowadays. This trend is however coming to end as the size of transistors is reaching the quantum limit.

In the last decade, two-dimensional (2D) crystals have emerged as a disruptive materials platform. Those layered crystals are excellent candidates for next-generation technologies due to their ultimate thinness and dangling-bonds-free surface. In addition, they offer better scaling than traditional 2D electron gas based on III-V compounds. In spite of the aforementioned advantages, some technological obstacles still hinder the industrial integration of 2D materials in electronics. The most important ones are the growth and the post-processing of wafer-scale high-quality crystals, robust passivation schemes and device-related aspects such as the contact resistance or doping.

In this thesis, first-principles simulations are performed on systems composed of graphene or transition metal dichalcogenides (TMDs). Their transport properties are computed using the *OpenMX* code based on the Green's functions formalism. First, metal-graphene interfaces are studied in the top-contacted geometry. Charge injection from metal to graphene is understood through the lens of a semi-empirical transport model so that the transport mechanisms impeding the contact resistance are identified. Afterwards, quantum transport is investigated inside the graphene channel. The objective is to benchmark the transport characteristics of polycrystalline samples resembling the ones produced by the industry. Finally, the operation of a TMDs-based atomically thin FET is investigated. Stain-induced current modulation is predicted through nano-scale quantum engineering, a mechanism not yet observed in TMDs-based lateral junctions.

The overall objective is to provide a deeper understanding of some degrading factors in the low-dimensional limit while proposing novel functionalities for 2D crystals architectures.

ACKNOWLEDGMENTS

A tout seigneur, tout honneur, j'aimerais donc adresser en premier lieu mes sincères remerciements à mon promoteur, Jean-Christophe Charlier. Cette thèse marque l'achèvement de 6 années de collaboration. Le Prof. J.-C. Charlier est à la fois un chercheur de renommé internationale et un individu avec une fibre sociale et humaine exceptionnelle. Ainsi, il a ma profonde reconnaissance pour son soutient continu, autant sur le plan personnel que professionnel.

Je tiens ensuite à adresser mes remerciements aux lecteurs de ma thèse, dont le contenu a grandement bénéficié de leurs commentaires. Je remercie le Prof. D. Beljonne pour son dynamisme et son analyse physico-chimique, le Prof. Ph. Dollfus pour le partage de son expertise du transport électronique et des dispositifs électroniques et le Prof. B. Hackens pour la pertinence et la justesse de ses remarques orientées du point de vue de l'expérience. Enfin, et non des moindres, le Dr. V.-H. Nguyen a toute mon estime et ma reconnaissance pour le colossal travail collaboratif abattu lors de mon doctorat. Sa vivacité d'esprit et ses compétences techniques ont défini à jamais mes standards de recherche en plaçant la barre très haute.

Il me faut ensuite évidemment évoquer le reste des charbonniers. Je tiens à remercier du fond du cœur Simon et Aurélien pour leur conseils lors de mon séjour au parc météo. Leur contribution technique à mon travail de recherche et humaine à mon épanouissement personnel est tout simplement inestimable. Benoit, mettons les choses au clair, tu es *de facto* un charbonnier ! A toi, un énorme merci pour m'avoir éclairé à la fois de l'intelligence de tes remarques et de l'authenticité de nos discussions à cœur ouvert. Même si notre cohabitation fût plus brève, je n'en oublie pas moins Jean-Jo, qui m'a énormément aidé dans tous les aspects informatiques de ma thèse. Les conseils et le professionnalisme d'Andrés sont aussi à mettre en exergue. Enfin, je remercie Aurélie, Jiaqi et Laura pour leur bonne humeur et la subtile touche féminine apportée au groupe. A vous tous, merci d'être vous, tout simplement ! J'espère vous revoir sur les pistes de bowling pour partager une bonne tranche de rire tout en étanchant notre soif de mousse houblonnée

Tout naturellement, j'enchaîne mes remerciements avec le Sc17 dans son ensemble. Je remercie les Profs. G.-M. Rignanese et X. Gonze pour

m'avoir éclairé de leurs judicieuses remarques scientifiques tout au long de ma thèse. Similairement, Matteo and Michiel ont toute ma reconnaissance. Jean-Mi, tu as toute ma gratitude pour m'avoir aidé dans mes galères informatiques. Je remercie aussi le Dr. C. Collignon pour son soutient technique sur les clusters du CECI, plus particulièrement nic4.

Parmi l'abondance de gens talentueux étant passés par le labo, j'aimerais en évoquer quelques uns. Guillaume, ce fut un réel plaisir de te côtoyer pendant toutes ces années. Tes (trop) nombreuses qualités ne sont plus à démontrer. Nicolas, j'ai énormément apprécié les conférences passées ensemble, les séances de badminton ou nos débats engagées sur l'état du monde. Ton esprit libre est à mes yeux un modèle de vertu. Bogdan, ta présence au labo m'emplit toujours autant de joie. J'aspire à montrer un jour ta justesse et ta sensibilité émotionnelle. Enfin, gardons le meilleur pour la fin. Raghed, ta rencontre fut une faveur du destin. Je ne serais jamais devenu aussi bon à Stratego ou Civ sans toi !

A tout ceux qu'il reste à énumérer, l'ensemble des (anciens) collègues, les compagnons du Black, les partenaires de foot ou de barbecue, les membres de l'ACIM, à vous tous, merci d'avoir enchanté ces années de recherche.

Enfin, d'un point de vue plus personnel, j'aimerais évoquer ici quelques personnes en particulier. Mumske, tu es la meilleure, je te dois tellement... Elise, ton grand frère sera toujours la pour toi. Charlotte, je n'oublierai jamais les moments passés ensemble. Ana, merci pour ton soutient lors de ces (difficiles) mois d'écriture.

PUBLICATIONS

All the publications authored during this PhD thesis are listed below, ordered by publication date.

- VH Nguyen, **S Dechamps**, P Dollfus, JC Charlier, Valley filtering and electronic optics using polycrystalline graphene, Physical Review Letters, **117**, 247702 (2016)
- **S Dechamps**, VH Nguyen, JC Charlier, Ab initio quantum transport in polycrystalline graphene, Nanoscale, **10**, 7759-7768 (2018)
- A Champagne, **S Dechamps**, SMM Dubois, A Lherbier, VH Nguyen, JC Charlier, Computational atomistic modeling in carbon flatland and other 2D nano-materials, Applied Sciences, **10**, 1724 (2020)
- **S Dechamps**, VH Nguyen, JC Charlier, Quantum transport in metal-graphene nano-junctions, in preparation (2022)
- **S Dechamps**, VH Nguyen, JC Charlier, Straintronics in ballistic 2D lateral junction transistors, in preparation (2022)

CONTENTS

1 INTRODUCTION 1
- 1.1 Two-dimensional materials . . . 3
- 1.2 Graphene . . . 5
- 1.3 Polycrystalline graphene . . . 7
- 1.4 The contact resistance . . . 9
- 1.5 Transition metal dichalcogenides . . . 11
- 1.6 2DMs-based heterostructures . . . 12
- 1.7 Outline of the thesis . . . 13

2 QUANTUM TRANSPORT 15
- 2.1 Diffusive transport . . . 15
- 2.2 The transport regimes . . . 16
- 2.3 The Landauer formalism . . . 17
- 2.4 The Green's functions formalism . . . 21
- 2.5 The Green's functions formalism in OpenMX . . . 27

3 ELECTRONIC PROPERTIES OF GRAPHENE 33
- 3.1 The structure of graphene . . . 34
- 3.2 A tight-binding model of graphene . . . 36
- 3.3 Low energy linearization . . . 42
- 3.4 First-principles calculations in graphene . . . 43

4 METAL-GRAPHENE CONTACTS 45
- 4.1 Trilayer graphene on metal surfaces . . . 49
- 4.2 Doping of graphene on metal surfaces . . . 55
- 4.3 Doping of graphene on realistic metal surfaces . . . 62
- 4.4 Quantum transport in metal-TLG junctions . . . 68
- 4.5 Transport model in metal-TLG junctions . . . 74
- 4.6 Quantum transport in realistic metal-TLG junctions . . . 84
- 4.7 Conclusion . . . 87

5 POLYCRYSTALLINE GRAPHENE 91
- 5.1 Quantum transport through GBs . . . 93
- 5.2 Quantum transport through extended GBs . . . 98
- 5.3 Quantum transport through disordered GBs . . . 101
- 5.4 Conclusion . . . 104

6 TMDS-BASED LATERAL JUNCTIONS 107
- 6.1 Transition metal dichalcogenides . . . 109
- 6.2 Lateral heterojunctions of TMDs . . . 111

6.3 Straintronics in lateral TMDs junctions 115
6.4 Field-effect transistor of lateral TMDs junctions 119
6.5 Conclusion 130
7 CONCLUSION 133
7.1 Polycrystalline graphene 133
7.2 The contact resistance 135
7.3 2DMs-based heterostructures 136
A DENSITY FUNCTION THEORY 143
A.1 The many-body problem 143
A.2 The Born-Oppenheimer approximation 144
A.3 The Hohenberg-Kohn theorems 145
A.4 The Kohn-Sham equations 146
A.5 The Exchange-correlation functionals 149
B SEMI-EMPIRICAL TRANSPORT MODELS 151
B.1 The Wentzel-Kramers-Brillouin approximation 151
B.2 Transport model in metal-graphene junctions 154
Bibliography 155

LIST OF FIGURES

Figure 1.1 Moore's law in integrated circuits. 2
Figure 1.2 Band gap of 2D semiconductors. 4
Figure 1.3 STEM image of a graphene GB. 8
Figure 1.4 Interface geometries of metal-2D contacts. 9
Figure 1.5 Imaging a $MoSe_2$-WSe_2 lateral junction. 13
Figure 2.1 The Landauer picture for electronic transport. . 18
Figure 2.2 The two-terminal transport setup. 23
Figure 3.1 The orbitals in graphene. 35
Figure 3.2 The structure of graphene. 36
Figure 3.3 Electronic bands of graphene. 39
Figure 3.4 Electronic bands of graphene. 42
Figure 4.1 Key parameters used to model graphene-based devices. 48
Figure 4.2 Structural properties of TLG upon adsorption. . 50
Figure 4.3 Electronic properties of TLG upon physisorption. 52
Figure 4.4 Electronic properties of TLG upon chemisorption. 53
Figure 4.5 Key parameters used to model doping at the metal-graphene interface. 55
Figure 4.6 Work functions in metal-TLG junctions. 58
Figure 4.7 Charge transfer in metal-TLG junctions. 61
Figure 4.8 Fermi level shifts in metal-TLG junctions. 62
Figure 4.9 Atomistic models for realistic metal-TLG junctions. 64
Figure 4.10 Energy profiles of realistic metal-TLG junctions. 66
Figure 4.11 Quantum transport in metal-graphene junctions. 69
Figure 4.12 First-principles transport through metal-TLG junctions. 73
Figure 4.13 Energy surface projected in momentum space for TLG and various metals. 75
Figure 4.14 Density of states of Ag, Au and Cu. 79
Figure 4.15 First-principles transport through a potential barrier at the metal-graphene interface. 81
Figure 4.16 Transport properties of metal-TLG junction within the transport model. 85
Figure 4.17 Comparison between the transport model and the Green's functions approach 87

Figure 5.1 Atomic structure of a graphene GB. 94
Figure 5.2 First-principles transport through ideal GBs. . . 96
Figure 5.3 First-principles transport through a realistic GB. 99
Figure 5.4 First-principles transport through realistic GBs with peridioc disorder. 100
Figure 5.5 First-principles transport through disordered GBs.103
Figure 5.6 First-principles transmission map for disordered GBs. 105
Figure 6.1 FET-device based on 2D lateral junctions. 110
Figure 6.2 Electronic properties of monolayer TMDs. 111
Figure 6.3 Atomic structures of MoS_2-WSe_2 lateral junctions.112
Figure 6.4 Interfacial properties of MoS_2-WSe_2 lateral junctions. 114
Figure 6.5 Strain effects on electronic transmissions through MoS_2-WSe_2 lateral junctions. 117
Figure 6.6 Spin effects on electronic transmissions through MoS_2-WSe_2 lateral junctions. 118
Figure 6.7 Transport properties of a MoS_2-WSe_2 based FET. 121
Figure 6.8 Transport properties and carrier statistics of a MoS_2-WSe_2 based FET. 123
Figure 6.9 Electronic properties of strained WSe_2. 124
Figure 6.10 Electronic structure modifications of strained TMDs-based systems. 125
Figure 6.11 Quantum tunneling model for MoS_2-WSe_2 lateral junctions. 127
Figure 6.12 Transport properties of a MoS_2-WSe_2 based FET at various channel and gate lengths. 128
Figure 6.13 Transport properties of a uniformly strained MoS_2-WSe_2 based FET. 129
Figure A.1 Kohn-Sham algorithm for convergence. 148

ACRONYMS

2DMs 2D materials

BTH Bardeen transfer Hamiltonian

BZ Brillouin zone

CBM Conduction band minimum

CBO Conduction band offset

CVD Chemical vapor deposition

DFT Density-functional theory

DoS Density of states

FET Field-effect transistor

GB Grain boundary

GB-HET Graphene-based hot electron transistor

GGA Generalized-gradient approximation

HS Heterostructure

KS Kohn-Sham

LCAO Linear combination of atomic orbitals

LCR Left lead - channel - right lead

LDA Local density approximation

LDoS Local density of states

MOSFET Metal-oxide semiconductor field-effect transistor

NEGF Non-equilibrium Green's function

PAO Pseudo-atomic orbitals

PBE Perdew-Burke-Ernzerhof

PG Polycrystalline graphene

QTG Quasi transport gap

RTG Real transport gap

SOC Spin-orbit coupling

STEM Scanning tunneling electron microscopy

STS Scanning tunneling spectroscopy

TB Tight-binding

TLG Trilayer graphene

TMD Transition metal dichalcogenide

VBM Valence band maximum

VBO Valence band offset

vdW Van der Waals

WKB Wentzel-Kramers-Brillouin

1 INTRODUCTION

Moore's law [1] refers to the prediction that the number of transistors on integrated circuits doubles approximately every two years. This empirical observation has been consistent with projections from the semiconductor industry for more than five decades, as illustrated in Fig.1.1. Over this period, continued improvement in transistors density, performance and energy efficiency have been sustained by technological innovations and scientific breakthroughs. This exponential development transformed the first crude computers from the 70s into the ubiquitous and high-performance sophisticated machines of nowadays. At the same time, the semiconductor industry has grown into a worldwide market with an addressable revenue of $ 550 billion in 2021 [2].

As the elemental building block of modern electronics, the metal-oxide-semiconductor (MOSFET) lies at the foundation of the semiconductor revolution. Interestingly, the logic characteristics of the MOSFET improves as its dimensions are reduced. Over the decades, its switching speed has increased drastically following a geometrical law, while its switching energy has decreased in a similar fashion [4]. The transistor revolution has therefore been powered by the combined improvement in density and logic operations. This exponential trend in increased performance is however starting to falter [5]. As the dimension of the channel drops to the tens of nanometers, leakage currents appear and impede the proper operation of the transistor. The principal issue resides in the dissipation rate of the heat generated by such leakage currents. The size scaling of MOSFET becomes impractical for most applications as the power density dissipated by the logic chips reaches about 100 W cm^{-2}[6]. Those disruptive phenomena are collectively termed as short-channel effects. The continued miniaturization of transistors by suppressing short-channel effects for the development of logic and memory electronics is often referred to as More Moore. In addition to More Moore, the semiconductor industry has recently been pursuing alternative strategies called More than Moore, where devices are improved through functional diversification by incorporating technologies that do not scale with Moore's law [7].

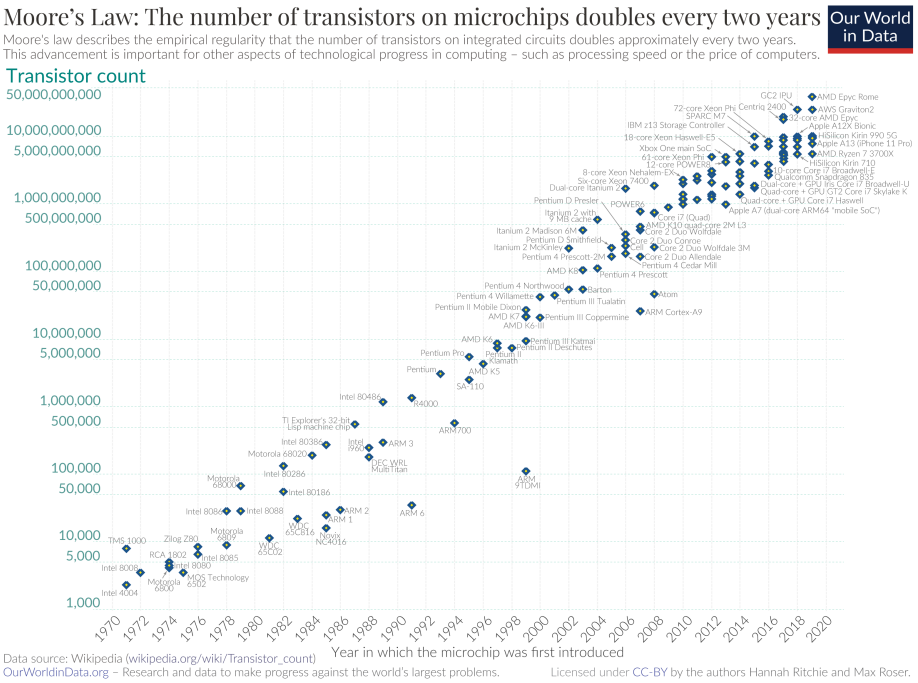

Figure 1.1: Illustration of Moore's law. Source: Our World in Data [3]

Concerning More Moore, 3D architectures, strained silicon channels or high-κ gate dielectrics currently stands as the most practical avenues for the continued improvement of silicon-based transistors. For example, the traditional planar geometry has been replaced by alternative technologies, such as the multiple gate transistors [8], FinFETs [9] and ultra-thin body transistors (UTB) [10]. Great efforts are also pursued on the search for novel materials to replace silicon-based technologies. In this regard, nano-materials[1] are of great interest for transistor applications as they offer many electrical and mechanical advantages compared to silicon [11]. For example, the III-V compound semiconductors such as GaAs or InAs exhibit outstanding electron transport properties. Transistors based on those materials were already demonstrated for high-speed and high-frequency electronic systems [12]. In fact, industrial manufacturing of III-V compounds integrated circuits is well established for applications as diverse as smartphones, cellular base stations, fiber-optic systems, wireless local-area networks, satellite communications, radar, radioastronomy and defense systems. Non-

1 The term nano-material applies to any material with at least one dimension below 100 nm

etheless, another class of nano-materials could represent an alternative for the continued scaling of electronic devices.

1.1 TWO-DIMENSIONAL MATERIALS

Two-dimensional materials (2DMs) are a subclass of materials that exhibit a singular set of electronic, optical and mechanical properties owing to their reduce dimensionality. 2DMs derive from layered structures, where in-plane chemical bonds are strong while inter-layer coupling is weak. At the monolayer limit, the unique electronic properties of 2DMs are determined by the confinement of electrons inside the sheet. The large surface-to-volume ratio provides the opportunity to tailor their properties by surface treatment, such as chemical functionalization [13]. The range of 2DMs for applications in electronic devices includes graphene, hexagonal boron nitride (hBN), transition metal dichalcogenides (TMDs), silicene and phosphorene [14]. On top of those materials with band gaps ranging from a few meV to several eV, there are potentially hundreds more that could be isolated in the near future. The broad catalogue of 2D semiconductors implies that optimal candidates can be associated to specific applications [15]. Fig.1.2 illustrates the rich diversity of 2DMs, whose electronic properties can be engineered by changing the number of layers, straining or alloying. This broad set of properties can be exploited for a wide range of photonics, optoelectronics and electronics applications. The interest of 2DMs is indeed not limited to integrated circuits but extends to non-computational systems [16] such as photodetectors and modulators for image sensors, light detection and ranging, data communication, lasers, piezoelectronics, thermoelectrics, nano-electro-mechanical systems, radio-frequency devices, magnetic devices and all sort of gas, chemical and biologicals sensors.

The fundamental and industrial research on 2DMs has shown phenomenal development in recent years [17]. For example, the production of layered materials has progressed tremendously in a short time, from the mechanical exfoliation of micrometer-scale mesas [18] to the direct synthesis of large scale flakes [19].

2DMs are excellent candidates for next-generation electronic devices due to their ultimate thinness and dangling-bonds-free surface. The ability to control the channel thickness with atomic accuracy translates into improved gate control over the channel and into reduced short-channel effects [20]. This contrasts with UTB 3D semiconductors which

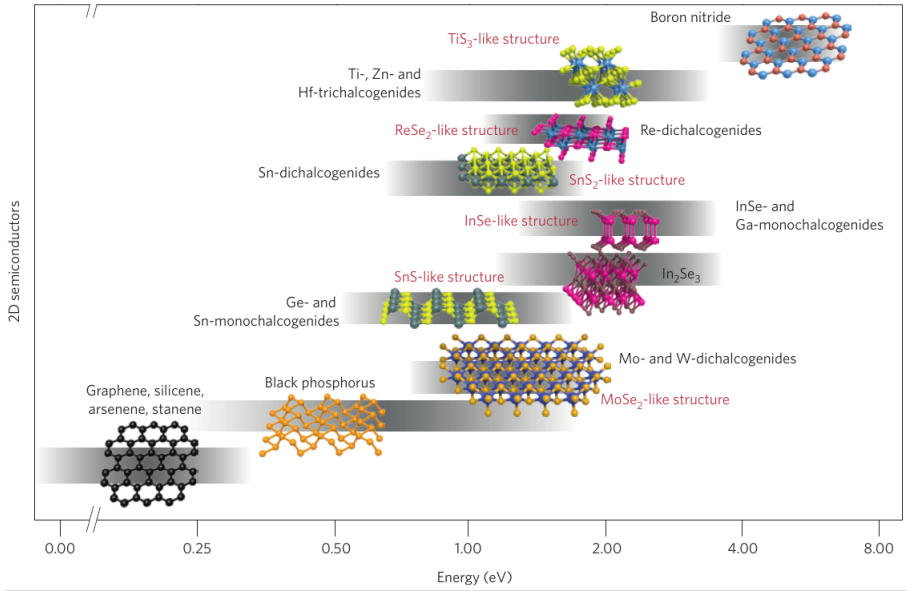

Figure 1.2: Illustration of the band gap for different 2D semiconductors, with the corresponding crystal structure of the subclass of 2DMs. The grey horizontal bar indicates the range of band gaps that are attainable by material engineering. Adapted from Ref.[15].

exhibit poor electrostatics and where the presence of dangling bonds and interfacial states results in a substantial decrease in performance. In addition, 2DMs offer better scaling than traditional 2D electron gas based on III-V compounds while their weak inter-layer interaction mitigate the lattice mismatch with the substrate.

In spite of the aforementioned advantages, some technological obstacles still hinder the industrial integration of 2DMs in electronic devices. The principal bottleneck for the high-volume manufacturing of 2DMs-based technologies resides in the growth of large-area single crystals of high quality [16]. The milestone is to produce wafer-scale layers that are comparable in quality to samples currently being synthesized in research rooms. The ideal growth methods would yield uniform crystals of controllable thickness. Afterwards, the synthesized 2D crystal needs to be transferred to the target substrate by nearly winkle-free and residue-free transfer processes. The development of a bottom-up methods enabling area-selective growth of 2DMs directly on the substrate is an alternative attractive option. Another critical issue towards practical applications is related to the contact resistance between 2DMs and metals. To comply with performance requirements, the contact

must be ohmic and show low resistance. At this time, the best results for metal-2DMs contacts are still at least one order of magnitude higher compared to technological standards in transistors [21]. Conventional techniques of contact engineering such as substitutional doping usually fail in 2DMs [22], requiring the realization of unconventional solutions in 2D contacts. Last but not least, some of the most promising 2DMs (silicene and phosphorene) are unstable under standard conditions. This chemical reactivity demands robust passivation techniques and effective processing strategies to retain the unique properties of these materials.

Two subclasses of 2DMs are investigated in this manuscript: graphene and transition metal dichalcogenides (TMDs), currently regarded as the most practical alternatives to silicon-based technologies [23]. Those materials offer a large set of properties and are chemically stable at ambient conditions while their production and post-processing methods are compatible with industrial requirements. In this regard, many outstanding graphene- and TMDs-based optoelectronic and electronic applications were already demonstrated.

1.2 GRAPHENE

Carbon is a widely abundant material that exhibits a rich variety of allotropic forms depending on its chemical bonding. Stemming from this structural abundance, carbon-based systems display an equally large diversity of physical features [24]. Carbon allotropes are organized as a function of their dimensionality, as this later characteristics determines a great deal of their physical properties. Fullerenes are 0D allotropes whose molecule consists of carbon atoms connected together in a closed mesh. 1D carbon-based systems exist in the form of carbon nanotubes or nanoribbons. Graphene is a 2D honeycomb lattice nanostructure, where carbon atoms are arranged in two triangular sublattices. Graphite results from the stacking of a significant number of graphene layers coupled together by van der Waals (vdW) forces, forming a 3D carbon-based system. As demonstrated by this latter example, graphene can provide the source material for the synthesis of those other carbon allotropes. Fullerenes can be synthesised by introducing pentagons in the hexagonal lattice, creating a positive curvatures that curls up the layer into a sphere. If graphene is cut along a certain direction, a nanoribbon is formed. Alternatively, a carbon nanotube is produced when the ribbon is rolled on itself and the edges are connected together.

In 2004, graphene was first isolated by mechanical exfoliation of small mesas of highly oriented pyrolytic graphite by Novoselov *et al.* [18]

The carbon atoms in graphene are sp^2-hybridized, with one s-orbital and two p-orbitals connecting each atom with its three nearest neighbors by a σ-bond. Such strong chemical bond is responsible for the robustness of the material. The third p-orbital is oriented perpendicularly to the plane in order to form π-bonds, similarly to aromatic molecules in organic compounds. The π-bonds are not localized and are responsible for electronic conduction properties in the graphitic structures.

Graphene displays unusual electronic properties due to the confinement of electrons in two dimensions and to its hexagonal lattice [24, 25]. Its low-energy excitations are massless, chiral, Dirac fermions. Such particles are characterized by a linear dispersion of the electronic bands, forming a conical dispersion near the corners of the Brillouin zone (BZ). Those charge carriers move through the lattice with a Fermi velocity (v_F) that is about 300 times smaller than the speed of light. Many of the unique properties of graphene originate from the particular energy dispersion of massless Dirac fermions. For example, the integer quantum Hall effect is observed under the application of a magnetic field at room temperature [26]. Charge carriers in graphene are insensitive to external electrostatic potentials due to the so-called Klein paradox, meaning that particles are transmitted through a potential barrier with a probability of 1 at normal incidence [27]. Other relativistic quantum mechanical effects include the appearance of a finite minimal conductivity [28] or Veselago lensing in graphene p-n junctions [29].

In neutral graphene, the chemical potential crosses the conical dispersion at the Dirac point, such that the density of states (DoS) is zero. For this reason, graphene is considered a gapless semiconductor or a zero-overlap semimetal. The vanishing DoS means that electronic conductivity is relatively low at the Fermi level (E_F). This inconvenient can be overcome by doping graphene, increasing greatly its conductivity. Experiments showed that electronic mobility of graphene is extremely high, with routinely reported results of about $10,000$ $\mathrm{cm^2V^{-1}s^{-1}}$ for graphene on SiO_2 substrate [30]. From a theoretical perspective, mobility is limited to $200,000$ $\mathrm{cm^2V^{-1}s^{-1}}$ due to phonon scattering [31]. Impurities present at the substrate surface are also an important source of scattering. For example, the highest mobility were measured experimentally as $200,000$ $\mathrm{cm^2V^{-1}s^{-1}}$ for suspended graphene at low temperature (~ 5 K) [32], in excellent agreement with theoretical prediction.

Similarly, the encapsulation of graphene in hBN yields comparable values due to its atomic smoothness and chemical inertia [33]. The large mobility means that charge carriers are able to travel over several micrometers without scattering.

A great deal of applications already exploited the extraordinary properties of graphene, such as gas sensors [34], photodectectors [35], solar cells [36], field-effect transistors [37], transparent electrodes [19, 38], flexible electronics [19, 39], electromechanical resonators [40, 41] and interconnects [42]. Owing to its structural flexibility, high electronic mobility, excellent gate controllability, low-energy linear dispersion with electron-hole symmetry and gapless character, graphene is an ideal platform for the design of novel electronic devices based on unconventional concepts, such as valleytronics [43, 44] or electronic optics [29, 45, 46].

In line with the enormous scientific and technological interests on graphene, the European Commission created the Graphene Flagship. With a budget of € 1 billion, the objective of the consortium is to coordinate research on an unprecedented scale, forming Europe's biggest ever research initiative. The Graphene Flagship is tasked with bringing together academic and industrial researchers to take graphene from the realm of academic laboratories into commercial applications. The core of the consortium consists of over 170 academic and industrial research groups in 22 countries [47].

1.3 POLYCRYSTALLINE GRAPHENE

The sources of disorder in graphene are abundant: ionized impurities in the substrate, adsorbates on the surface, vacancies, ripples, grain boundaries (GBs), ... The presence of such imperfections is inevitable due to the associated reduction in Gibbs free energy when introducing defects, through an augmentation in entropy. Specific defects can be intentionally introduced in the sample through various methods, such as energetic particles radiation or chemical treatment. The former technique already allowed the observation *in situ* of defects formation, migration and reconstruction using electron microscopy [48]. Additionnaly, defects engineering could enable the emergence of unusual mechanical, optical and electronic properties in defective graphene [49].

The production of 2DMs on a industrial scale would most probably yield polycrystalline flakes. Graphene is not an exception, although substantial improvements were recently reported on the syn-

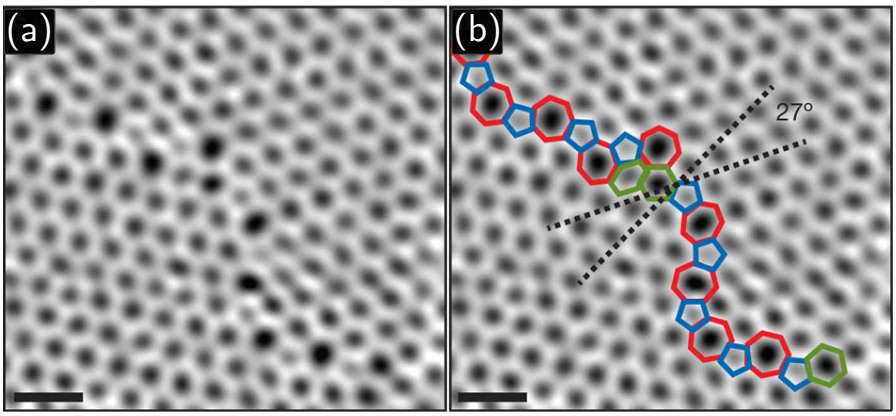

Figure 1.3: STEM image showing two graphene grains intersect with a 27° relative rotation angle. **(a)** An aperiodic line of defects stitches the two grains together. **(b)** The image from **(a)** with the pentagons (blue), heptagons (red) and distorted hexagons (green) outlined. Adapted from Ref.[50].

thesis of large-area single-crystal monolayer graphene [51]. While early graphene-based devices were fabricated from mechanically exfoliated monocrystalline samples, this technique is not suitable for wafer-scale production. Chemical vapor deposition (CVD) currently stands as the most practical, mature and reliable production method for graphene-based applications. As a proof of concept, the growth of meter-scale single-layer films was already demonstrated in 2010 using this technique [38]. The resulting flakes are however polycrystalline. Grains nucleate simultaneously at different location of the substrate and grow until a polycrystalline monolayer is formed. Line defects (or GBs) are created at the domains intersections in order to account for their misorientation, as illustrated in Fig.1.3. The growth is influenced by numerous parameters [52]. The crystalline orientation, surface roughness and defects topology of the underlying wafer will inevitably impact the properties of the over-layered graphene. The growth rate of the graphene flakes also depends on the temperature and pressure of the vapor. In consequence, it is possible to engineer the grains (orientation, shape and size) through intelligent tuning of the substrate and growth conditions.

From a fundamental perspective, a primary and important aspect is to determine the ultimate structural configuration of the resulting films, by characterizing the type of defects appearing during growth and post-processing. In a next step, their influence on the electronic

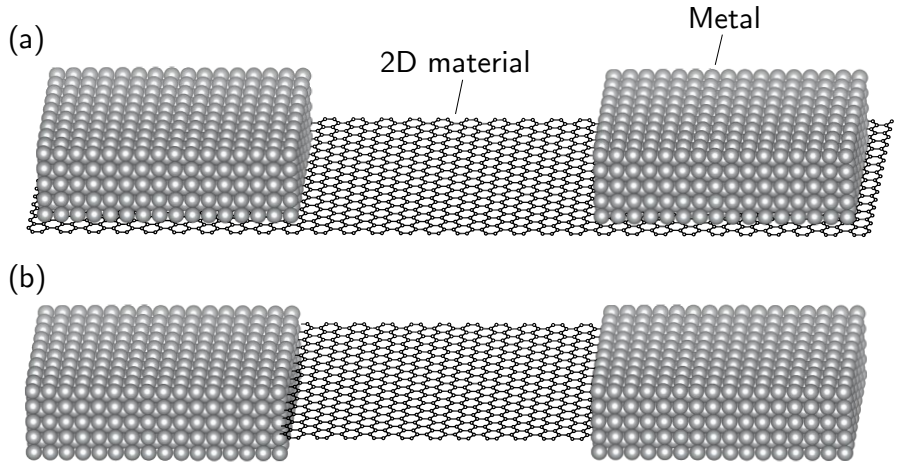

Figure 1.4: Interface geometries of metal-2D contacts. **(a)** Top-contacted configuration. **(b)** Edge-contact configuration.

properties needs to be investigated. On the one hand, such imperfections eventually lead to a reduction in performance of graphene-based devices [20]. On the other hand, unconventional electronic devices have been proposed through defects engineering in polycrystalline graphene (PG) [53–55]. The objective is thus to provide a comprehensive picture of electronic phenomena, such that degrading effects are removed while singular functionalities are preserved.

1.4 THE CONTACT RESISTANCE

The contact resistance (R_c) represents one of the most fundamental issues for the integration of 2DMs in electronic devices, by strongly restricting the injection of electrons in the channel. This substantial contact resistance stems from the pristine surface of 2DMs, as charge injection is hindered by the difficulty to form chemical bonds at the metal interface. Low R_c is however critical for the realization of next-generation electronic devices exhibiting high performance. For example, negligible contact resistance would enable high on-state currents and high-frequency operation in integrated circuits [56].

There are two fundamental types of interface geometries between metal contacts and 2DMs: top contacts and edge contacts, as illustrated in Fig.1.4. In the former case, the 2DMs interacts weakly with the electrodes by dispersion forces. The interface therefore consists of a vdW gap that acts as a tunneling barrier which greatly reduces charge

injection. The formation of a pure edge contact is much more difficult in single- and few-layer systems, owing to the atomic thinness of 2DMs. Nonetheless, edge contacts offer significant advantages over top contacts, such as a higher degree of covalency, smaller tunnel barrier widths and better scaling [57].

Concerning graphene-based devices, large sample-to-sample variations are found in the literature [58]. Such widespread disparity is due to the dependence of R_c on several factors such as the metal used for contacts, the substrate, self-doping, the fabrication process, the contact geometry or the methods and conditions of measurement. The first challenge is therefore to produce devices with reproducible and low contact resistance. In order to exploit its exceptional properties, R_c in graphene-based devices should be comparable to the standard obtained for silicon-based technology (about 50 $\Omega\mu$m) [58].

As conventional techniques of contact engineering usually fail in 2DMs, a fundamental understanding of charge injection and collection is critical for identifying unconventional solutions. Initially, the nature of the interaction between the metal and graphene needs to be characterized because interfacial properties governs everything in the 2D limit. The zero energy band gap and the vanishing DoS of graphene modifies drastically the situation compared to conventional metal-semiconductor contacts. In standard devices, two possibilities may occur: an ohmic contact or a Schottky junction. The situation is much more complex in metal-graphene junctions. As graphene shows great sensitivity to environmental factors, its electronic properties are strongly influenced upon contact, even for weakly interacting metal electrodes. In essence, charge injection results from complex transport phenomena arising between a 3D electrode and a 2D layer. The transmission mechanisms occur primarily by quantum tunneling due to the absence of bonding sites at the graphene surface. The tunneling probability and the number of conducting modes in the channel are then determined by interfacial properties, most notably by the charge transfer between the metal and graphene.

Hence, the diagnosis is evident. The characterization of R_c is a challenging task that requires a comprehensive description of both metal-graphene interfaces and quantum transport phenomena, as will be discussed in the present thesis.

1.5 TRANSITION METAL DICHALCOGENIDES

The general formula for TMDs is MX_2, where M represents the metal while X is a chalcogen. A single layer is composed of three layers in the form X-M-X. This subclass of 2DMs has been extensively investigated in the recent years. Indeed, it displays properties of the uttermost interest both for fundamental studies of novel physical phenomena and for applications in nanoelectronics and nanophotonics [59]. In contrast to graphene, the electronic properties of TMDs are governed by *d*-orbitals of the transition metal. The degree of filling of these orbitals determines considerably the electronic structure of the TMD, inducing intriguing condensed matter phenomena such as charge density waves [60], superconductivity [61] and Mott transitions [62]

The most studied TMDs are formed by group VI transition metals Mo and W combined with chalcogens S and Se. In their trigonal prismatic form arranged in an hexagonal lattice (2H), MX_2 are intrinsic semiconductor at the monolayer limit, with band gap spanning the visible part of the spectrum. Their electronic properties can be tailored by the number of layers [63], through chemical composition [64] or by mechanical deformation [65]. An important feature of 2H-TMDs lies in their lack of inversion symmetry, resulting in a splitting of the electronic bands due to the substantial spin-orbit interaction. The combination of this broken inversion symmetry with the presence of a direct band gap makes TMDs ideal candidate for applications in valleytronics [66]. In addition, monolayers 2H-TMDs display exceptional optical properties such as strong photoluminescence [63], sizable light-matter interaction [67] and large quasiparticles binding energies [68, 69] that can be utilized for unconventional optoelectronic devices.

From the perspective of field-effect devices, TMDs are ideal candidates for ultra-short channels due to their heavy effective mass [70] and low in-plane dielectric constant [71]. Effective mass materials with lower mobilities would indeed become preferable for sub-5 nm MOSFETs to suppress source-drain tunneling [72]. Quantum transport simulations analyzed the scaling limits of these materials, demonstrating a high degree of electrostatic control and an excellent scalability for low-power nano-scale applications [73, 74]. Most of the attention was caught by MoS_2, WS_2 and WSe_2 in the past decade, owing to their relatively high charge carriers mobilities, successful growth at the wafer-scale and ambient chemical stability [22]. For example, an ultrathin TMD-based FET was demonstrated as early as 2007 using mechanically exfoliated

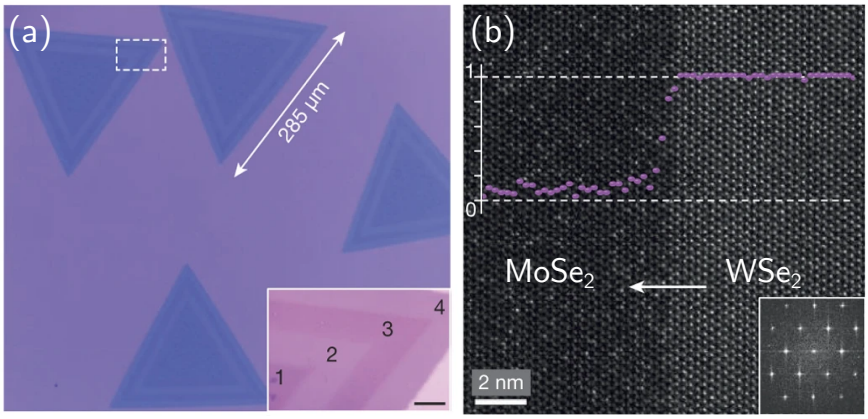

Figure 1.5: Imaging a $MoSe_2$-WSe_2 lateral junction. **(a)** Low-magnification optical image of three-junction heterostructures. The inset shows a larger magnification of the area within the dashed box. The dark-contrast regions correspond to MoSe2, the bright-contrast regions to WSe2. **(b)** STEM image of a sharp interface, with the corresponding Fourier-transform patterns and composition profiles (atomic fraction of tungsten per vertical atomic column). The average interface width is 1 nm. Adapted from Ref.[82].

layers of MoS_2 [75]. While this latter material is typically n-doped, the ambipolar characteristics of WSe_2 make it possible to create p-n junctions or complementary logic circuits [76]. In this context, those 2D semiconductors represent excellent building blocks for the design of next-generation electronic devices. One promising avenue is the possibility to connect those materials in order to construct systems with tailor-made characteristics, as explored in the following.

1.6 2DMs-based heterostructures

Novel prospects in materials design were recently suggested by combining atomically thin crystals together in the form of vdW heterostructures (HSs) [77]. Such nano-scale engineering would benefit from the abundant catalogue of 2DMs and their dangling-bonds free surfaces. In a sense, this paradigm represents a natural extension of the synthesis of semiconductor heterojunctions that occured more than three decades ago [78]. This pioneering research lead to the development of device concepts such as the hot-electron transistors [79], the resonant tunneling transistors [80] and the heterojunction bipolar transistor [81].

HSs can be constructed from isolated 2D layers by stacking or stitching them together. The former method yields vertical systems bonded solely by vdW forces while the latter technique produces lateral junctions connected by covalent bonds. In those systems, features that are weak or absent in the pristine counterparts can be enhanced or created by combining the appropriate layered crystals. In this context, recent developments in 2DMs-based HSs led to numerous breakthroughs in fundamental research and to substantial improvements in advanced devices [22]. As vertical HSs attracted the most attention, lateral HSs hold considerable experimental and theoretical promises [83].

Owing to their rich diversity in electronic properties, TMDs are ideal elementary components for the realization of HSs with tunable properties. From a structural perspective, their similar lattice enables epitaxial stitching inside the plane. Over the past few years, continuous and controlled nucleation of TMDs-based lateral junctions has been demonstrated by one-step, two-step and sequential techniques [84]. Fig.1.5 displays an optical image and a STEM image of a $MoSe_2$-WSe_2 lateral junction obtained by one-step growth. Since the unique characteristics of lateral HSs stem from the junction area, it is of primary importance to produce seamless and atomically sharp interfaces free of defects. In this regard, recent experiments have shown excellent control over sharpness [82] and strain [85, 86] at the interface. An enhanced structural controllability would translate into novel prospects in straintronic devices due to the predominant role of strain in TMDs. Overall, extensive progresses on material growth and device design in TMDs-based lateral HSs would enable quantum engineering at the ultimate limit in the forthcoming years [21].

1.7 OUTLINE OF THE THESIS

Over the years, the tremendous growth in computational resources has fueled equally large advances in material science. It is nowadays possible to characterize the electronic structure of systems containing tens of thousands of atoms with excellent accuracy. Technological progress and fundamental science are operating in a positive feedback mechanism: a better understanding of the device components leads to improved performances or to novel functionalities, and vice versa. In line with this historical trend, this manuscript addresses some of the fundamental aspects related to the realization of next-generation electronics based on 2DMs using first-principles methods.

The prime objective of this thesis is to accurately estimate how the production and integration of these materials on an industrial scale would affect their transport properties. For this reason, the Green's functions formalism used to model quantum transport in low-dimensional systems is covered in Ch.2. As the results presented throughout the thesis were obtained with the *OpenMX* software package, the principal features of the implementation of the Green's functions method in the code are introduced afterwards.

The following chapters are dedicated to the description of graphene-based materials. Although its zero band gap prevents its practical use in FETs, graphene remains an essential element for the seamless integration of 2DMs into electronic circuits. In this regard, the electronic properties of pristine graphene are covered in Ch.3. This section gives us the opportunity to present the tight-binding (TB) model and density-functional theory (DFT), the numerical techniques used to predict the electronic properties of 2D crystals. As a natural follow-up, the principal issues related to the wafer-scale integration of graphene are addressed in the next two chapters.

At first, the contact resistance in graphene-based devices is studied for the top-contacted geometry. First-principles simulations are employed in Ch.4 to examine extensively the interfacial properties of metal-graphene junctions. This analysis is performed on the most commonly used metals for contacting. Our attention in the next part of the chapter turns towards charge injection, by computing the transport characteristics of the corresponding systems. An empirical transport model is constructed from our *ab initio* results in order to gain physical insights into the transmissions mechanisms occurring at the interface. Afterwards, quantum transport is investigated inside the graphene channel. The objective is to benchmark the transport characteristics of polycrystalline samples as produced by the industry. To this end, the degrading effects of line defects are covered in Ch.5.

In the last chapter of the manuscript (Ch.6), the operation of a MoS_2-WSe_2 junction FET is investigated. The interfacial properties of the 1D junction are characterized using first-principles techniques. Nano-scale quantum engineering is then proposed through the application of strain in order to induce current modulation, a mechanism not yet observed in TMDs-based lateral junctions.

2 QUANTUM TRANSPORT

If an electric potential difference is applied along a device, charge carriers at the Fermi level are accelerated by a subsequent electric field ($\mathcal{E}$). The movement of these mobile charges through the crystal is then impacted by several scattering centers. Defects are an inevitable source of scattering. Electronic transport is also impeded by the influence of other electrons (Coulomb scattering) or by vibrations of the lattice (electron-phonon scattering). Scattering processes are divided in two categories : elastic and inelastic. The distinction is made whether energy is transferred upon collision or not. Electron-phonon interaction is typically an inelastic process while collision with defects are well described by elastic scattering.

The purpose of this chapter is to present the theoretical framework that can be used to characterize quantum transport in a crystal.

2.1 DIFFUSIVE TRANSPORT

In semi-classical transport, charge carriers are assumed to drift in a material at a constant velocity. This drift velocity (v_d) corresponds to the average velocity attained by charged particles due to the presence of $\mathcal{E}$, which accounts for the collective effects of successive collisions and thermal fluctuations. This net flow of charge carriers creates a current (I) that is expressed (in Ampere) as

$$I = nev_d \tag{2.1}$$

where n is the total number of charge carriers and e is the elementary charge. As I derives from the random propagation of charge carriers through the structure, this transport regime is denoted as diffusive. It is possible to relate the drift velocity with the average time between collisions (τ_c), also called the mean free time

$$v_d = \frac{e\tau_c}{m^*}\mathcal{E} \tag{2.2}$$

where m^* is the charge carrier effective mass. This last expression is pivotal in semi-classical transport as it allows to define essential

transport features, such as the electron mobility (μ) or the electron mean free path (l_e). It also enables us to relate the electric field and the current, or equivalently, the current density

$$J = \frac{e^2 n \tau_c}{A m^*} \mathcal{E} = \sigma \mathcal{E} \tag{2.3}$$

where σ denotes the electrical conductivity and A is the surface cross section of the conducting element. This equation is known as Ohm's law. The conductivity is therefore a material property that indicates how much current is generated when an electric field is applied. It is dependent on many parameters such as the temperature, the type of defects in the crystal or the concentration of charge carriers. In some situations, it is more convenient to refer to the resistivity (ρ) of a conductor, defined as $\rho = 1/\sigma$.

This simple description of transport is surprisingly accurate for samples of macroscopic dimensions, typically larger than a few micrometers in size. As the size of the device is reduced, the quantum mechanical nature of charge carriers needs to be considered. The miniaturization of electronic devices at the nano-scale therefore requires to characterize electronic transport in a framework that accounts for such quantum mechanical contributions.

2.2 THE TRANSPORT REGIMES

If the dimension of the system is comparable or smaller than the electron mean free path, the conduction of charge carriers is not diffusive anymore. Electrons can be transmitted through the device without being scattered. This implies that the electric resistance is no more dependent of the length of the channel. This transport regime is denoted as ballistic.

An equally important characteristic length in quantum transport is the coherence length (l_ϕ). This quantity defines the distance over which the waves propagates before its phase its randomized. This means that for devices smaller than l_ϕ, the interference of electron waves affects the device characteristics. Interference phenomena such as weak localization effects can be observed at cryogenic temperatures, when the contribution from the lattice vibration is minimal. Indeed, electron-phonon scattering is one of the predominant mechanisms causing phase relaxation at high temperatures while electron-electron

interaction prevails in the low temperature regime. Note that l_ϕ is typically longer than l_e in electronic devices.

Another typical characteristic length is considered last: the Fermi wavelength (denoted as λ_F). This parameter is nothing more than De Broglie wavelength associated to an electron located at the Fermi level. It is expressed as $\lambda_F = \hbar/k_F$, where k_F is the electron momentum on the Fermi surface. If the cross section of the system is at the order of λ_F, the available energy states are quantized. From the perspective of quantum transport, this means that the transmission of electrons through the system is done only via specific energy levels.

In the following, nano-scale systems with dimensions smaller than l_e and l_ϕ are considered. Electronic transport therefore occurs in the form of the ballistic transmission of phase-coherent electrons.

2.3 THE LANDAUER FORMALISM

The Landauer-Büttiker formula has been extensively utilized in the past decades to calculate the transport properties of nanostructures. This approach is adequate to describe the steady-state quantum transport regime, i.e. transport that is both ballistic and coherent. This formalism was originally proposed by Landauer in 1957 for the characterization of 1D structures [87, 88]. The fundamental idea is to express the transport current by means of transmission probabilities. In other words, it establishes a fundamental relation between the electron wave function (yielding the scattering amplitudes) of a quantum system and its conducting properties. This scheme was later on generalized by Buttiker for multi-channel [89] and multi-terminal [90] devices.

In order to model single-electron quantum transport, the following geometry is considered: a central scattering region is connected to two electron reservoirs by two semi-infinite leads. The corresponding configuration is represented in Fig.2.1. Inside the central region, the single-electron wave function is scattered by a spatially varying potential V_S. The reservoirs (also denoted contacts or terminals) are defined under the following assumptions. First, there is no phase relation between incoming and outgoing elements inside of a reservoir. Additionally, the contacts are described by well-defined chemical potential (μ) and temperature (T). Finally, the resistance related to the reservoir is zero or is at least negligible in regards to the resistance of the scattering region.

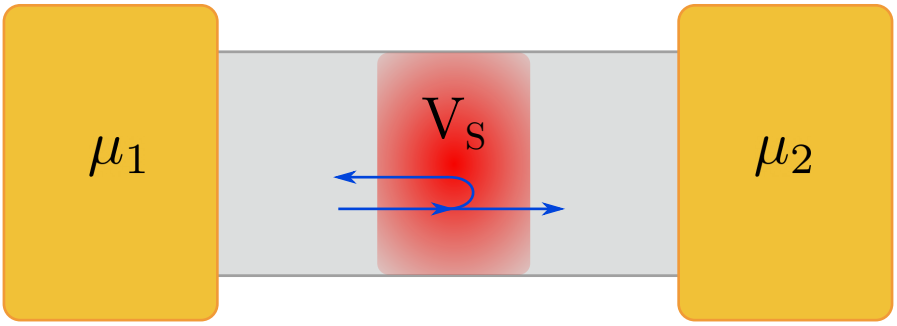

Figure 2.1: Schematic representation for the Landauer picture for electronic transport. Electrons flow through a central scattering region enclosed between two semi-infinite electrodes that are connected to thermal reservoirs. The central region is defined by a potential (V_S) that determines the probability of electronic transmission or reflection (as illustrated by the arrows). The current driving force is the difference between the chemical potentials μ_l and μ_r of the reservoirs

In general, the contacts have different chemical potentials, μ_l and μ_r, such that their difference $\mu_l - \mu_r$ represents a driving force. Electrons are emitted from a reservoir with an equilibrium distribution via perfectly conducting electrodes. Owing to the previous assumptions on the contacts, it implies that the statistics of the charge carriers can be described by independent Fermi-Dirac distributions. So the probability that an electron has energy E is given by

$$f(E, \mu_i) = \frac{1}{\exp\{(E - \mu_i)/k_B T\} + 1} \tag{2.4}$$

where the index i indicates the reservoir that supplied the particle and k_B is the Boltzmann constant.

At thermal equilibrium, the statistics of charge carriers in the whole system is characterized by the function $f(E, E_F)$, where E_F is the Fermi energy of the device. Once an electrostatic potential is applied, the chemical potential are adjusted in consequence

$$\mu_i = E_F + eV_i \tag{2.5}$$

where V_i is the electrostatic potential applied to each lead and the total bias voltage is $\Delta V = V_l - Vr$. The effect of applying a bias voltage to the device (or shifting the chemical potentials) is to generate a current between the reservoirs. It is assumed in the following that electrons in the left (right) reservoir are Bloch states with positive (negative)

momentum $\vec{k}$. The effect of the scattering potential is included by introducing a transmission coefficient T_k associated to a momentum $\vec{k}$. This term represents the probability that an incoming electron is transmitted when crossing the defective region. Identically, the particle is reflected back into the reservoir with a probability R_k, where $R_k = 1 - T_k$ by probability conservation. Importantly, the reflection and transmission probabilities are energy-dependent.

In this framework, the current flowing from the left lead into the conducting region is obtained as

$$\begin{aligned} I &= I_l + I_r \\ &= \frac{2e}{L}\sum_k f(E_k, \mu_l) v_k T_k + \frac{2e}{L}\sum_{k'} f(E_{k'}, \mu_r) v_{k'} T_{k'} \end{aligned} \tag{2.6}$$

where v_k is the group velocity, defined as $v_k = (1/\hbar)(\partial E/\partial k)$. The factor 2 has been introduced to account for the spin degeneracy while the normalization factor $1/L$ is related to the 1D volume. The summation on $\vec{k}$ ($\vec{k'}$) is done over all available momenta in the left (right) lead, as ensured by the Fermi-Dirac function which accounts for the statistics of charge carriers. This means that I_l (I_r) are the contributions to the total current of the Bloch states originating in the left (right) lead. Concerning the transmission probabilities, T_k and $T_{k'}$ are identical by time reversal symmetry argument, meaning that scattering is independent of the direction of flow.

The momentum summations in Eq.2.6 can be changed to an energy integral, such that the current is now expressed as

$$\begin{aligned} I &= \frac{2e}{h}\int_{-\infty}^{\infty} T(E) f(E, \mu_l) dE - \frac{2e}{h}\int_{-\infty}^{\infty} T(E) f(E, \mu_r) dE \\ &= \frac{2e}{h}\int_{-\infty}^{\infty} T(E)\left[\, f(E, \mu_l) - f(E, \mu_r)\right] dE \end{aligned} \tag{2.7}$$

An interesting approach is to analyze the previous relation in the limit of zero temperature. In this regime, the Fermi-Dirac distribution can be approximated by step function. This implies that

$$I = \frac{2e^2}{h} T(E_F) \Delta V \tag{2.8}$$

from the previous definition of the applied voltage. It has also been assumed that $\Delta V \to 0^+$, meaning that the whole system is not far from equilibrium.

The definition of the conductance $G = dI/dV$ gives

$$G(E) = \frac{2e^2}{h} T(E_F) = G_0 T(E_F) \tag{2.9}$$

which is the Landauer formula. A quantum of conductance (G_0) has conveniently been introduced in the previous relation. It is insightful to consider the situation of a scattering free device for which $T = 1$. In this case, Eq.2.9 predicts that the system shows a non-zero resistance, independently of the nature of the device and of the band dispersion. The reason is that there exist an intrinsic and unavoidable resistance related to the contacts. Energy is dissipated by thermalization when a charge propagating from one lead eventually reaches the other. This result is valid while the previous assumptions still hold: scattering is elastic, so that energy is conserved and the phase-coherence is preserved. Since its initial proposal, many experimental evidence confirmed the accuracy of the Landauer formula.

The Landauer formula was originally proposed for a single spin-degenerated channel but can easily be extended to a multi-channel device using transfer matrices. In the multi-channel configuration, multiple Bloch states carry a current $2ev_k$ at a given energy. If one considers the transmission and reflection matrices (denoted t and r, respectively), the conservation of current implies

$$t^\dagger t + r^\dagger r = 1 \tag{2.10}$$

for a momentum-lossless devices. The matrix element t_{ij} is defined as the probability amplitude of an incident electron in the i channel to be transmitted into the j channel. Identically, r_{ij} is the probability of the electron to be reflected into the channel j. This leads to the Landauer-Büttiker formula for a multi-channel system [89]

$$G = \frac{2e^2}{h} \mathrm{Tr}[t^\dagger\ t] \tag{2.11}$$

in the limit of low voltage bias and zero temperature. Consistently, the total transmission for a given electron of energy E is expressed as

$$T = \mathrm{Tr}[t^\dagger\ t] = \sum_{ij} |t_{ij}|^2 \tag{2.12}$$

This general relation considers that electrons are scattered elastically between all the available channels.

As demonstrated above, the Landauer-Buttiker represents an adequate framework for the description of quantum transport. A central element of the formalism resides in the computation of the transmissions coefficient, which can be achieved by means of Green's functions.

In mathematics, a Green's functions is the solution to an inhomogeneous differential equation of the form

$$[z - L(\vec{x})]\, G(\vec{x}, \vec{x}'; z) = \delta(\vec{x} - \vec{x}') \tag{2.13}$$

where z is a complex number. In this case, only the time-independent Green's functions is considered. This equation is defined on a domain subject to specific boundary conditions that contains our coordinates $\vec{x}$ and $\vec{x}'$. The operator $L(\vec{x})$ is assumed to be a linear, Hermitian, time independent differential operator and to possess a complete set of eigenfunctions ($\psi_n(\vec{x})$) and eigenvalues.

In the framework of non-relativistic quantum mechanics, $L(\vec{x})$ is given by the Hamiltonian operator ($H(\vec{x})$) of the system. The previous relation becomes in the context of the time-independent Schrodinger equation

$$[E - H(\vec{x})]\, G(\vec{x}, \vec{x}'; E) = \delta(\vec{x} - \vec{x}') \tag{2.14}$$

The function $G(\vec{x}, \vec{x}')$ can be interpreted as the response of the system in x due to a excitation in x'. From the perspective of quantum transport, this perturbation corresponds to a wave incident from one of the leads.

The first step towards a description of transport by means of Green's functions is to obtain a mathematical representation of the two-terminal device in Fig.2.1. In this regards, the Hamiltonian matrices of the scattering region and the leads are conveniently expressed in framework of the linear combination of atomic orbitals (LCAO). Once the form of $H(\vec{x})$ has been defined, the techniques utilized to solve Eq.2.14 will be discussed. The eventual objective is to obtain $G(\vec{x}, \vec{x}'; E)$ such that the ground state and transport properties can directly be computed.

As illustrated in Fig.2.2, the two-terminal setup has been divided into subsequent layers with similar cross-section dimensionality. The layers consist of the smallest set of atoms that forms an unit cell of the semi-infinite crystal composing the leads. The system presents a translational symmetry along the directions perpendicular to the transport axis. From the Bloch theorem, this means that the transport

problem can be divided into a set of independent problems associated each with one transverse k-point. This configuration is defined as the left lead-channel-right lead (LCR) geometry. The corresponding Hamiltonian reads

$$H = \begin{pmatrix} \cdots & \cdots & \cdots & \cdots & & & \\ H_{ll}^{\dagger} & H_l & H_{ll} & 0 & \cdots & & \\ 0 & H_{ll}^{\dagger} & H_l & H_{lc} & 0 & \cdots & \\ \cdots & 0 & H_{lc}^{\dagger} & H_c & H_{rc}^{\dagger} & 0 & \cdots \\ & \cdots & 0 & H_{rc} & H_r & H_{rr}^{\dagger} & 0 \\ & & \cdots & 0 & H_{rr} & H_r & H_{rr}^{\dagger} \\ & & & \cdots & \cdots & \cdots & \cdots \end{pmatrix} \tag{2.15}$$

where the H_l, H_c and H_r are the Hamiltonian sub-matrices related to the left lead, central region and the right lead, respectively. The size of those matrices is determined by the number of basis orbitals used in each region (denoted N_i). The matrix elements H_{lc} and H_{rc} describe the interaction occurring at the interface with the central part. Their corresponding dimension is $N_l \times N_c$ and $N_r \times N_c$, respectively. Each layer of the left (right) lead only interacts with the neighboring layers, as accounted for by the matrix H_{ll} (H_{rr}). It was assumed here that the system preserves time-reversal symmetry, so that all matrices are Hermitian, meaning that $H_{lc}^{\dagger} = H_{cl}$. If the set of orbital basis set is non-orthogonal, one needs to include the overlap matrix S that is expressed similarly to Eq.2.15.

The above-presented Hamiltonian is intrinsically infinite-dimensional due to the definition of the two-terminal device in Fig.2.2. In consequence, it becomes problematic to compute the eigenvectors and eigenvalues by a classical diagonalization scheme. Fortunately, the Green's functions approach enable us to naturally account for the open boundary of the transport problem. In this section, the main results of the Green's functions method are presented while the algebraic details are overlooked. The interested reader is referred to Refs.[91, 92] for a rigorous mathematical demonstration of the forthcoming results.

The first step is to write Eq.2.15 in a more compact manner

$$H = \begin{pmatrix} H_l^{\infty} & H_{lc}^{\infty} & 0 \\ H_{cl}^{\infty} & H_c & H_{cr}^{\infty} \\ 0 & H_{rc}^{\infty} & H_r^{\infty} \end{pmatrix} \tag{2.16}$$

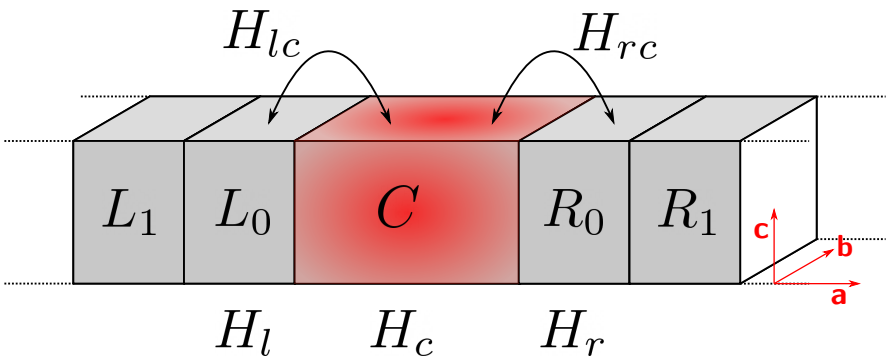

Figure 2.2: Schematic representation of the two-terminal transport setup treated by the Green's functions method. The device (or central region, denoted C) is connected to two semi-infinite leads that are composed of a periodic array of layers along the a-axis (denoted $L_0, L_1, R_0, R_1, \ldots$, while periodic boundary conditions are applied on the bc-plane. Block decomposition of the Hamiltonian into sub-matrices associated with the central region (H_c) and the repeated layers of the semi-infinite leads (H_r and H_l). The matrix elements H_{lc} (H_{rc}) represents the coupling between the left (right) lead and the central part.

where the subscript H^∞ has been introduced to denote infinite-dimensional matrices. Let us now write again the infinite eigenvalue problem of Eq.2.14 in the matrix form

$$[E\ I - H]\, G = I \tag{2.17}$$

where the I is the identity matrix and the energy dependence is implied. This relation explicitly reads for the two-probe system

$$\begin{pmatrix} K_l^\infty & K_{lc}^\infty & 0 \\ K_{cl}^\infty & K_c & K_{cr}^\infty \\ 0 & K_{rc}^\infty & K_r^\infty \end{pmatrix} \begin{pmatrix} G_l^\infty & G_{lc}^\infty & 0 \\ G_{cl}^\infty & G_c & G_{cr}^\infty \\ 0 & G_{rc}^\infty & G_r^\infty \end{pmatrix} = \begin{pmatrix} I^\infty & 0 & 0 \\ 0 & I & 0 \\ 0 & 0 & I^\infty \end{pmatrix} \tag{2.18}$$

where the notation $K = [E\ I - H]$ has been used. Note that an infinitesimal term η has been implicitly introduced as $E \to E + i\eta$. This term is a numerical artifact that needs to be incorporated in order to compute the poles of the Green's functions by contour integration in the complex plane. Note that a similar approach is to apply $E \to E - i\eta$. The sign of $i\eta$ actually determines causality in the system: the Green's functions yields the response forward (backward) in time for a causal (anti-causal) response if one has $E + i\eta$ ($E - i\eta$). In the following, a causal response is always assumed.

The objective is to determine the expression of G_c such that the eigenvalue problem can be solved in the scattering region, while accommodating for the influence of the contacts. By using Eq.2.18, the following relations are obtained

$$K_l^{\infty} G_{lc}^{\infty} + K_{lc}^{\infty} G_c = 0 \tag{2.19}$$

$$K_{cl}^{\infty} G_{lc}^{\infty} + K_c G_c + K_{cr}^{\infty} G_{rc}^{\infty} = 0 \tag{2.20}$$

$$K_{rc}^{\infty} G_c + K_r^{\infty} G_{rc}^{\infty} = 0 \tag{2.21}$$

by selecting the three block equation that involve G_c. After substituting Eqs. 2.19 and 2.21 into Eq.2.20, an explicit expression for G_c is obtained

$$G_c = [E\ I - H_c - \Sigma_l - \Sigma_r] \tag{2.22}$$

where Σ_l is associated to the concept of self-energies. This result indicates that the Green's functions of the scattering region can therefore be viewed as the one of the isolated system, with the only difference that H_c is corrected by an amount $(\Sigma_l + \Sigma_r)$. The self-energy are defined as non-Hermitian matrices

$$\Sigma_l = K_{cl}^{\infty} G_l K_{lc}^{\infty} \tag{2.23}$$

$$\Sigma_r = K_{rc}^{\infty} G_r K_{cr}^{\infty} \tag{2.24}$$

and account for the coupling at the interface after contacting. The Hermitian part causes a shift of the eigenvalues while the anti-Hermitian component leads a scattering of the energy spectrum. Here, G_l and G_r are the Green's functions related to the isolated leads

$$G_i^{\infty} = [K_i^{\infty}]^{-1} \tag{2.25}$$

It might seem that nothing much was gained by writing down Eqs. 2.23 and 2.24 since the formulas to obtain Σ_i still involve semi-infinite matrices. This is however not exact because the elements of $K_{i,c}^{\infty}$ are all zero except in a certain corner of the matrix, where they are equal to K_{ii} of size $N_i \times N_i$. Indeed, only a restricted set of atoms interact with the scattering region close to the interface, owing to the finite extension of localized atomic orbitals. This enables us to express the non-zero elements of the self-energy matrices

$$[\Sigma_l]_{N_l,N_l} = K_{ll}^{\dagger} g_l K_{ll} \tag{2.26}$$

$$[\Sigma_r]_{N_r,N_r} = K_{rr} g_r K_{rr}^{\dagger} \tag{2.27}$$

where g_L and g_r are the so-called surface Green's functions related to the contacts, corresponding to the sub-matrices of G_l^∞ and G_r^∞ in the lower right and the upper left corners, respectively. The surface Green's functions have dimensions $N_i \times N_i$ and are typically computed by recursion methods [93, 94].

Transmission, current and spectral function

The primary objective of the present section is to provide an expression for the transmission coefficients introduced in the Landauer formula. The current is calculated by employing the charge continuity equation

$$I = \frac{\partial \rho_s}{\partial t} \tag{2.28}$$

where ρ_s is the charge density matrix related to a system "s".

In the Green's functions formalism, ρ_s is expressed as

$$\rho_s = \frac{1}{2\pi} \int A_s f(E, \mu_s) dE \tag{2.29}$$

where A_s is the associated spectral function. Generally speaking, A_s is defined in terms of the retarded and advanced Green's functions

$$A_s = i \left(G_s - G_s^\dagger \right) \tag{2.30}$$

It is insightful to write the spectral function in the Lehmann representation (also called spectral representation)

$$A_s = 2\pi \sum_n \delta(E - \epsilon_n) \psi_n \psi_n^\dagger \tag{2.31}$$

where ψ_n and ϵ_n are the set of eigenvectors and eigenvalues corresponding to the Hamiltonian, respectively. This latter relation indicates that the spectral function has a peak at each eigenstate of H_s. It is therefore equivalent to the partial DoS, justifying Eq.2.29.

If the two-terminal setup is considered, the system under consideration is the central part and the charge continuity equation reads

$$\begin{aligned} I &= \frac{\partial \rho_c}{\partial t} \\ &= \int_{-\infty}^{\infty} \left(I^+ f(E, \mu_l) - I^- f(E, \mu_r) \right) dE \end{aligned} \tag{2.32}$$

by combining Eqs. 2.29 and 2.30. The Fermi-Dirac functions are introduced to take into account the injection of electrons by the reservoirs at chemical potential μ_l and μ_r. In order to obtain Eq.2.32, the eigenstates of the central part are divided into two groups associated with waves incident from the left and right contacts. This ansatz allows us to treat a non-equilibrium problem using equilibrium statistical mechanics. Consequently, the spectral function is separated into left and right components

$$\begin{aligned} A_c &= i\left(G_c - G_c^\dagger\right) = iG_c\left((G_c^\dagger)^{-1} - (G_c)^{-1}\right)G_c^\dagger \\ &= G_c\Gamma_l G_c^\dagger + G_c\Gamma_r G_c^\dagger \\ &= A_l + A_r \end{aligned} \tag{2.33}$$

which is valid if transport is coherent. Furthermore, the infinitesimal part of the Green's functions has been neglected. This last assumption implies that there exists no electronic states strictly localized in the device region that do not couple with the electrodes. We have also introduced the matrices

$$\Gamma_i = i\left[\Sigma_i - \Sigma_i^\dagger\right] \tag{2.34}$$

which accounts for the non-hermicity of the self-energies. These are Hermitian, positive semidefinite matrices called "broadening matrices" or "coupling matrices" since they describe the rate of in- and outflow of electrons from and to the leads.

On these assumptions, the right-going and left-going currents read (after some manipulations [91, 92])

$$I^+ = \frac{2e}{h}\,\mathrm{Tr}\left\{\Gamma_l G_c \Gamma_r G_c^\dagger\right\} = I^- \tag{2.35}$$

where the equality stems from the properties of the trace operator.

Finally, the formula of the total current for a two-terminal device is expressed in a straightforward manner as

$$I = \frac{2e}{h}\int_{-\infty}^{\infty} T(E)\left(f(E,\mu_l) - f(E,\mu_r)\right) \tag{2.36}$$

where

$$T(E) = \mathrm{Tr}\left\{\Gamma_l G_c \Gamma_r G_c^\dagger\right\} \tag{2.37}$$

is the transmission function. This expression (also called Caroli formula [95]) is strictly equivalent to the Landauer formula and represents a generalization of the Landauer-Buttiker theory.

2.5 THE GREEN'S FUNCTIONS FORMALISM IN OPENMX

OpenMX is a software package developed for nano-scale material simulations based on DFT [96, 97], norm-conserving pseudopotentials [98, 99] and localized pseudo-atomic orbitals (PAO) [100, 101]. The scope of the code is to enable the calculation of large scale *ab initio* electronic structures through a careful and efficient implementation of the methods and algorithms. In this manner, the electronic, magnetic, and geometrical structures of a wide variety of materials such as bulk materials, surfaces, interfaces, liquids, and low-dimensional materials can be investigated by DFT. Systems consisting of thousands of atoms can be treated using the conventional diagonalization method if several hundreds cores are used in parallel.

The non-equilibrium Green's functions (NEGF) method is implemented in *OpenMX* with the aim to be applicable to large scale complicated systems. A great deal of effort is spent on two fundamental aspects of the NEGF method. First, a remarkably efficient method is applied to the evaluation of the density matrix [102], the computationally most demanding part of the NEGF method. Second, boundary conditions between the scattering region and the leads are carefully handled in order to avoid spurious scattering. In the following, the essential features of the implementation are covered.

Equilibrium Green's functions

Since most of practical aspects in the implementation of the NEGF method appear in the ground state calculation of the system at equilibrium, the electronic structure calculation of the equilibrium ground state by the Green's functions method is detailed first.

The configuration of the two-terminal device of Fig.2.2 is considered, where the a-axis represents the transport axis. Note that the cells L_i and R_i can be different from each other as long as each type of cell contains the same number of atoms within the same structural configuration.

In the equilibrium state, the one-particle Kohn-Sham (KS) wave function in the system is expressed as a Bloch sum using PAO ($\phi_{i\alpha}$) located on site $\vec{r}_i$

$$\psi_{\sigma\nu}(\vec{k},\vec{r}) = \frac{1}{\sqrt{N}} \sum_n e^{i\vec{k}\cdot\vec{R}_n} \sum_{i\alpha} c_{\sigma\nu,i\alpha}(\vec{k}) \phi_{i\alpha}(\vec{r} - \vec{r}_i - \vec{R}_n) \tag{2.38}$$

where the indices σ, ν, i, α denote the spin, eigenstate, site and basis orbital, respectively. The lattice vector $\vec{R}_n$ and the Bloch wave vector $\vec{k}$ are defined in terms of the lattice vectors and the reciprocal lattice vectors, respectively. The summation over n runs over the N unit cells in the crystal. The summation over i and α is considered for all the basis orbitals in the 1D infinite cell owing to the absence of periodicity along the a-axis. The coefficient $c_{\sigma\nu,i\alpha}$ of the linear expansion in Eq.2.38 are given by the KS equation

$$\hat{H}_\sigma(\vec{k})c_{\sigma\nu}(\vec{k}) = \epsilon_{\sigma\nu}(\vec{k})\hat{S}(\vec{k})c_{\sigma\nu}(\vec{k}) \tag{2.39}$$

where $c_{\sigma\nu}$ is a column vector consisting of the coefficients $c_{\sigma\nu,i\alpha}$. The Hamiltonian $\hat{H}_\sigma$ and overlap matrices $\hat{S}$ read

$$H_{\sigma,i\alpha j\beta}(\vec{k}) = \sum_n e^{i\vec{k}\cdot\vec{R}_n} h_{\sigma,i\alpha j\beta,R_n} \tag{2.40}$$

$$S_{i\alpha j\beta}(\vec{k}) = \sum_n e^{i\vec{k}\cdot\vec{R}_n} s_{i\alpha j\beta,R_n} \tag{2.41}$$

where $h_{\sigma,i\alpha j\beta,R_n}$ and $s_{i\alpha j\beta,R_n}$ are the Hamiltonian and overlap matrix elements between two basis functions $\phi_{i\alpha}(\vec{r}-\vec{r}_i)$ and $\phi_{j\beta}(\vec{r}-\vec{r}_j-\vec{R}_n)$, respectively. The overlap matrix arises from the non-orthogonality of the PAO basis functions [100, 101].

Owing to their strictly localized nature, the basis functions must satisfy two conditions. First, localized basis orbitals in the central region C overlap with those in the regions L_0 and R_0 but do not interact with those of the regions beyond. Similarly, the overlap elements are non-zero only for localized basis orbitals of the L_i (R_i) region and the nearest neighboring cells L_{i-1} (R_{i-1}) and L_{i+1} (R_{i+1}). On these assumptions, the Hamiltonian has the tridiagonal form of Eq.2.15 while the overlap matrix has a similar structure. Consequently, the Green's functions in the central part is given by Eq.2.22 if the identity matrix is replaced by the overlap matrix for non-orthogonal PAO.

Equilibrium density matrix

One of the practical difficulties in the implementation of the NEGF method is how to evaluate the equilibrium density matrix efficiently and accurately [103, 104]. In *OpenMX*, the equilibrium density matrix is computed very efficiently using the contour integration method with a special treatment of the Fermi-Dirac function [102].

Let us first give an expression for the density matrix $\rho^{(eq)}_{\sigma,R_n}$ related to an orbital in the central cell and the other in the cell translated by $\vec{R}_n$

$$\rho^{(eq)}_{\sigma,R_n} = \frac{1}{\Omega}\int_{BZ}\left(\rho_{\sigma,+}(\vec{k}) - \rho_{\sigma,-}(\vec{k})\right)e^{-i\vec{k}\cdot\vec{R}_n}d\vec{k} \tag{2.42}$$

with Ω the volume of the unit cell and

$$\rho_{\sigma,\pm}(\vec{k}) = \frac{i}{2\pi}\int_{-\infty}^{\infty} G_{\sigma,c}(\vec{k}, E \pm i\eta)f(E,\mu) \tag{2.43}$$

where $G_{\sigma,c}(\vec{k}, E \pm i\eta)$ is the retarded (advanced) Green's functions if the sign is positive (negative), as previously discussed. The integration is performed over the BZ using the Monkhorst-Pack mesh [105]. The density matrix is therefore obtained from the imaginary part of the Green's functions due to the k-dependence of the Hamiltonian and overlap matrices.

For the efficient integration in Eq.2.43, the Fermi-Dirac function is expressed by a continued fraction representation

$$\frac{1}{1+\exp(x)} = \frac{1}{2} + \sum_{p=1}^{\infty}\frac{R_p}{x - iz_p} + \sum_{p=1}^{\infty}\frac{R_p}{x + iz_p} \tag{2.44}$$

where $\beta = 1/k_BT$, $x = \beta(z-\mu)$ and z is a complex variable. The real numbers z_p and R_p are the poles and the associated residues of the continued fraction representation, respectively, obtained via an eigenvalue problem derived from the continued fraction representation. Since all the z_p are real numbers, the poles iz_p are located on the imaginary axis.

As demonstrated by Ozaki *et al.* [106], the continued fraction representation is more adequate for integrating $\rho^{(eq)}_{\sigma,R_n}$ as it accounts for the the smoothness of the Green's functions in the faraway region of the real axis. This numerical subtlety allows for a remarkable convergence of the density matrix using a small number of poles. In addition, there is no ambiguity in the choice of the path in the contour integration, contrary to other schemes [103, 104, 107].

Charge density near the boundary

Although the basis functions are strictly localized in space, there is a non-negligible contribution to the charge density from the basis functions located in the leads near the boundary between the device

and the leads. In this context, the device includes the central part and the L_0 and R_0 regions. This additional charge contribution needs to be appropriately handled in order to avoid spurious scattering at the boundary.

The charge density n_σ in the device results from three contributions

$$n_\sigma(\vec{r}) = n_\sigma^{(cc)}(\vec{r}) + n_\sigma^{(sc)}(\vec{r}) + n_\sigma^{(ss)}(\vec{r}) \tag{2.45}$$

where the suffix s is either L or R and $n_\sigma^{(cc)}(\vec{r})$, $n_\sigma^{(sc)}(\vec{r})$, and $n_\sigma^{(ss)}(\vec{r})$ are the charge density contributions from the central, the lead and central, and the lead regions, respectively. Each charge contribution is explicitly given by

$$\begin{aligned} n_\sigma^{(cc)}(\vec{r}) &= \sum_n \sum_{i\alpha,j\beta} \rho^{(eq)}_{\sigma,i\alpha,j\beta,R_n} \\ &\quad \times \phi_{i\alpha}(\vec{r}-\vec{r}_i)\phi_{j\beta}(\vec{r}-\vec{r}_j-\vec{R}_n) \qquad (2.46) \\ n_\sigma^{(sc)}(\vec{r}) &= \sum_{n,n'} \sum_{i\alpha,j\beta} \rho^{(sc)}_{\sigma,i\alpha,R_n,j\beta,R_{n'}} \\ &\quad \times \phi_{i\alpha}(\vec{r}-\vec{r}_i-(\vec{R}_n \pm \vec{a}'))\phi_{j\beta}(\vec{r}-\vec{r}_j-\vec{R}_{n'}) \qquad (2.47) \\ n_\sigma^{(ss)}(\vec{r}) &= \sum_{n,n'} \sum_{i\alpha,j\beta} \rho^{(ss)}_{\sigma,i\alpha,R_n,j\beta,R_{n'}} \\ &\quad \times \phi_{i\alpha}(\vec{r}-\vec{r}_i-(\vec{R}_n \pm \vec{a}'))\phi_{j\beta}(\vec{r}-\vec{r}_j-(\vec{R}_{n'} \pm \vec{a}')) \qquad (2.48) \end{aligned}$$

where $\vec{a}'$ is the lattice vector of the unit cell for the L_0 or R_0 region along the a-axis. The displacement of $-\vec{a}'$ ($+\vec{a}'$) corresponds to an orbital localized in the L_1 (R_1) region (see Fig.2.2). The factor 2 for $n_\sigma^{(sc)}$ in Eq.2.45 originates from the implicit contribution of $n_\sigma^{(cs)}$.

The two contributions from the leads $n_\sigma^{(sc)}$ and $n_\sigma^{(ss)}$ are only relevant if the overlap of the associated two basis orbitals is not zero in the device region. Since this region is constructed by adding the L_0 and R_0 leads to the central part, it is expected that $\rho_\sigma^{(sc)}$ and $\rho_\sigma^{(ss)}$ are close to the density matrices of the isolated leads. Therefore, the density matrix elements of the leads calculated by the conventional method are used in Eqs. 2.47 and 2.48. This implementation strategy requires the device region to be large enough such that the previous approximation remains true.

Hartree potential with the boundary condition

Similarly to the charge density, the Hartree potential (V_H) in the device is calculated under the boundary condition that V_H at the boundary with the L_1 (R_1) region is the same as the one of the isolated lead. The Hartree potential is separated into two contributions [106]: the neutral atom potential (V_{na}) and a remaining part (δV_H). The former constitutes the largest part of V_H while the latter accounts for charge redistribution effects. Since V_{na} depends only on the atomic structure, it has no relation with the boundary conditions. The problem of the potential therefore comes down to solving the Poisson's equation

$$\nabla^2 \delta V_H(\vec{r}) = -4\pi \delta n(\vec{r}) \tag{2.49}$$

with

$$\delta n(\vec{r}) = n(\vec{r}) - n^{(a)}(\vec{r}) \tag{2.50}$$

where n is the total electron density obtained using Green's functions (see Eq.2.45) and $n^{(a)}$ is the atomic (or neutral) electron density calculated by superposition of each atomic electron density $n_i^{(a)}$.

In *OpenMX*, a combination of a 2D fast Fourier transform and a finite difference method is used to efficiently evaluate δV_H for the central region under the corresponding boundary conditions.

Hamiltonian and overlap matrix elements

The Hamiltonian matrix elements associated with the basis orbitals situated near the boundary are also treated in a specific manner. If the tails of two basis orbitals go beyond the boundary between the device and the L_1 (R_1) region, the associated Hamiltonian matrix elements are replaced by the corresponding element calculated by the conventional method for the isolated leads. This situation can only occur if the two basis orbitals are located in the L_0 (R_0) region owing to the conditions imposed to the leads. The replacement is made by assuming that the potential profile near the boundary is similar to that near the boundary between the regions L_1 (R_1) and L_2 (R_2). Similarly to V_H and n_σ, this assumption is justified if the size of the device region is large enough.

Non-equilibrium density matrix

For equilibrium systems, Green's functions are useful tools for calculating the thermodynamic properties of many-body systems or the linear responses of systems under small perturbations. In the non-equilibrium case, electrons are injected by the reservoirs due to the difference in chemical potentials and occupy the states corresponding to incoming waves in the contacts. The non-equilibrium Green's functions techniques was initiated by Schwinger [108] and Kadanoff and Baym [109] and later popularized by Keldysh [110].

Based on this formalism, the density matrix of the central part in the non-equilibrium state is evaluated by

$$\rho_{\sigma,R_n}^{(neq)} = \rho_{\sigma,R_n}^{(eq)} + \Delta\rho_{\sigma,R_n} \tag{2.51}$$

where the correction term is defined as

$$\Delta\rho_{\sigma,R_n} = \frac{1}{\Omega}\int_{BZ} \Delta\rho_{\sigma,R_n}(\vec{k}) e^{-i\vec{k}\cdot\vec{R}_n} \tag{2.52}$$

with

$$\begin{aligned}\Delta\rho_{\sigma,R_n}(\vec{k}) = \frac{1}{2\pi}\int_{-\infty}^{\infty} & G_{\sigma,c}(\vec{k}, E+i\eta)\Gamma_{\sigma,s_1}(\vec{k}, E) \\ & \times G_{\sigma,c}(\vec{k}, E-i\eta)\left[f(E,\mu_{s_1}) - f(E,\mu_{s_2})\right]\end{aligned} \tag{2.53}$$

where $s_1 = R$ and $s_2 = L$ if $\mu_l < \mu_r$, and vice versa. Similarly, the lower chemical potential is used in the calculation of the equilibrium density matrix in Eq.2.51. This approach is correct under two assumptions. First, the statistics of the incoming wave functions still obeys the Fermi-Dirac distribution in the scattering region. This assumption is correct in the single-particle picture since the same result is obtained from the Lippmann-Schwinger equation for non-interacting systems [91]. Second, electronic states of the central part whose energy lies below the lower chemical potential are in equilibrium. On these assumptions, the correction term only accounts for electronic states with an energy contained between the chemical potentials.

As a last comment, note that the integrand in Eq.2.52 is not analytic apart from the real axis. Thus, the contour integration method used previously for the equilibrium density matrix is not applicable. Instead, a simple rectangular quadrature scheme is applied owing to the effectively reduced energy range bounded by the Fermi-Dirac functions.

3 ELECTRONIC PROPERTIES OF GRAPHENE

The manuscript addresses two fundamental issues related to graphene-based technologies, specifically the contact resistance and the degrading effects of line defects in polycrystalline samples. It thus seems reasonable to discuss the electronic properties of graphene before anything else. This chapter also provides the opportunity to detail the theoretical framework within which the numerical simulations are performed.

The whole set of physical properties of a material is determined by the precise arrangement of its atoms and their interactions, as embodied by the Schrodinger equation. A complete hierarchy of methods has been developed to give more or less approximated solutions to the otherwise too complex many-problem. First-principle methods such as DFT or quantum Monte Carlo are at the base of this hierarchy while atomistic techniques such as TB models constitute the next level of approximations.

DFT is among the most popular and versatile methods available in condensed-matter physics [111], owing to its high accuracy while only requiring minimal information. This approach developed by Kohn and Sham [97] based on the Hohenberg-Kohn theorems [96] substitutes the many-electron interacting problem by a non-interacting problem with identical ground state charge density. An overview of DFT is provided in App.A. Implemented within the LCAO framework, DFT represents a practical solution for the accurate calculation of a vast number of properties in nanometer-scale systems. Its application to 2DMs forms an extensive literature discussing graphene, TMDs, group IV and group V layered materials, III–V layered compounds and practically any 2D crystal conceived so far [112].

The TB method is one of the most used techniques in the device community due to its computational efficiency and accuracy [111]. This numerical approach expands the electronic wave function upon the superposition of atomic orbitals of Bloch-form localized at each site of the atomic lattice. The Hamiltonian and overlap matrix elements are used as input parameters obtained empirically or from first-principles calculations. The Slater-Koster (SK) parametrization represents the most general formulation of TB by considering the orbital symmetries and

their spatial arrangement [113]. Several models have been developed for 2DMs, enabling the study of band structures of TMDs [114, 115], black phosphorus [116], spin-orbit effects in silicene, germanene and stanene [117], strain in graphene [118] and many other phenomena. While low energy electronic structures are well captured by TB models, electronic states at higher energy usually demand basis set optimization by increasing the number of orbitals or interacting neighbors.

As illustrated with graphene, the appropriate numerical approach should be determined by the scaling of the problem and the required accuracy.

3.1 THE STRUCTURE OF GRAPHENE

Graphene is an allotrope of carbon in the form of a single-layer of atoms arranged in a 2D hexagonal lattice [24, 119]. The carbon atoms are sp^2 hybridized in the plane, creating a trigonal structure where chemical bonds are oriented 120° with respect to each other. The sp^2 hybridization results from the bonding and anti-bonding of the $2s$ and $(2p_x, 2p_y)$ orbitals, as illustrated in Fig.3.1. The covalent bonds are denoted as σ and σ^* for the bonding and the anti-bonding, respectively. These orbitals are even with respect to the planar symmetry of graphene. The σ-bonds are responsible for most of the binding energy and the excellent mechanical properties of the sheet. The remaining outer-shell $2p_z$ orbitals are oriented perpendicularly to the plane. Their lateral interaction creates the π and π^* orbitals, which correspond to bonding and anti-bonding, respectively. These orbitals exhibit an odd symmetry with respect to honeycomb lattice. The electronic properties of graphene derive from the delocalized cloud of electrons formed by the π-bonds. When graphene is stacked to form graphite, the sheets are held together by weak vdW forces between the π orbitals.

Fig.3.2(a) depicts the 2D honeycomb lattice of graphene. The corresponding basis vectors (a_1 and a_2) are expressed in (x, y) coordinates

$$a_1 = \frac{a_0}{2}(\sqrt{3}, 1) \qquad a_2 = \frac{a_0}{2}(\sqrt{3}, -1) \tag{3.1}$$

where a_0 is the lattice parameters of graphene. The inter-atomic distance between carbon atoms (d) is roughly 1.42 Å, meaning that the hexagonal network is characterized by $a_0 = 2.45$ Å. The structure can be regarded as a triangular Bravais lattice with two atoms per unit cell (A and B). The A- and B-type atoms denotes each a sublattice and are surrounded

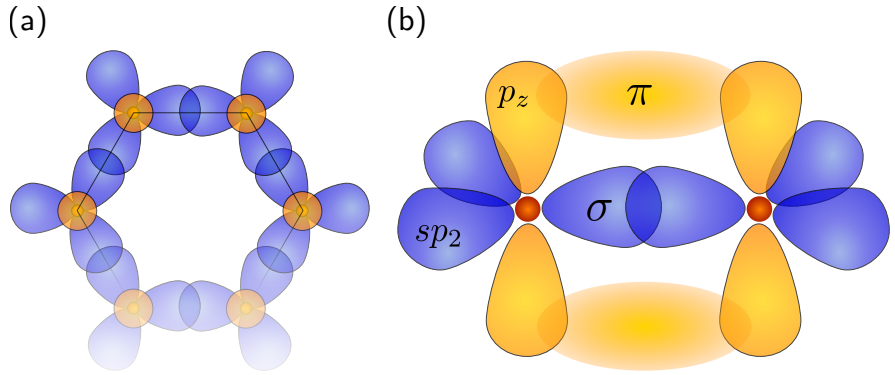

Figure 3.1: Illustration of the orbitals in graphene. **(a)** The three σ orbitals per carbon atoms are arranged in an hexagonal lattice, forming a 120° angle between each other. **(b)** The π bonds resulting from the hybridization of the p_z orbitals are oriented perpendicular to the sheet. The electronic properties of graphene derive from the circulation of electrons in the delocalized π-cloud.

by three atoms of the opposite type. The coordinates of the carbon atoms are defined in terms of the basis vectors as $(0,0)$ and $(1/3,1/3)$. One also defines the vectors that connect each atom to its nearest neighbors, the so-called nearest neighbors vectors

$$\delta_1 = \frac{d}{2}(-1,\sqrt{3}) \qquad \delta_2 = d(1,0) \qquad \delta_3 = \frac{d}{2}(-1,-\sqrt{3}) \tag{3.2}$$

From the real-space lattice vectors, the reciprocal lattice vectors are defined through the relation $a_i \cdot b_j = 2\pi\delta_{ij}$. In terms of (k_x, k_y) coordinates, those vectors are expressed as

$$b_1 = \frac{b}{2}(1,\sqrt{3}) \qquad b_2 = \frac{b}{2}(1,-\sqrt{3}) \tag{3.3}$$

with $b = 4\pi/a_0\sqrt{3}$. The Wigner–Seitz cell of this reciprocal lattice yields an hexagonal-shaped BZ. Two particular high-symmetry points located at the corners of the BZ, K and K', are of considerable importance for the description of the electronic properties of graphene. Another high symmetry point is the one labeled as M. Such points are defined in terms of (k_x, k_y) as

$$K = \frac{2\pi}{3a_0}(\sqrt{3},1) \qquad K' = \frac{2\pi}{3a_0}(\sqrt{3},-1) \qquad M = \frac{2\pi}{\sqrt{3}a_0}(1,0) \tag{3.4}$$

Fig.3.2(b) illustrates the hexagonal structure of the reciprocal space of graphene. Note that the hexagons of the reciprocal lattice are rotated by $\pi/2$

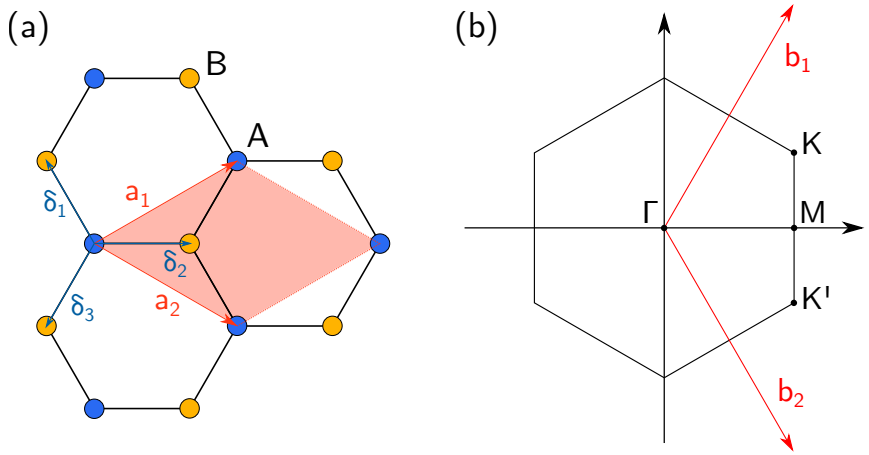

Figure 3.2: Structure of graphene. **(a)** Hexagonal lattice of graphene composed by two inter-penetrating two triangular sublattices, in blue and yellow. The periodicity of the lattice is given by the lattice vectors a_1 and a_2 while δ_i are the nearest neighbor vectors. **(on right)** The corresponding BZ, where the high-symmetry points K, K', Γ and M are represented. The periodicity of the BZ is given by the reciprocal vectors b_1 and b_2.

3.2 A TIGHT-BINDING MODEL OF GRAPHENE

The first TB description of graphene was already given by Wallace in 1947 [120]. In his seminal paper, he proposed to describe the electronic structure of graphene using a rather simple model that provides an analytical solutions to its eigenvalues and related eigenstates. Since the bonding and anti-bonding σ-bands are located far away in energy from the Fermi level, their influence on the electronic properties of graphene can be neglected. It follows that the electronic properties at low energy are related to the π- and π^*-bands, which correspond to the valence and conduction bands, respectively. The electronic wavefunctions of the different carbon atoms exhibit such symmetry such that the s, p_x, p_y orbitals do not overlap with the p_z orbitals. This means that the p_z electrons are the only orbitals contributing to the dynamics of charge carriers close to the Fermi level. Within this π-band approximation, each A and B atom is uniquely defined by one orbital per atom site.

The electronic properties of graphene can be derived by solving the Schrödinger equation associated to a honeycomb lattice with two

triangular sublattices. Bloch functions for each atom site are used as eigenvectors [121]

$$\Psi(\vec{k},\vec{r}) = c_A(\vec{k})\Phi_A(\vec{k},\vec{r}) + c_B(\vec{k})\Phi_B(\vec{k},\vec{r}) \tag{3.5}$$

where c_i are the coefficients of the linear expansion. The wavefunction is therefore expressed as a linear combination of Bloch sums on each sublattice. Each Bloch sum is defined as

$$\Phi_A(\vec{k},\vec{r}) = \frac{1}{\sqrt{N}}\sum_j e^{i\vec{k}\cdot\vec{R}_j}\phi_A(\vec{r}-\vec{r}_A-\vec{R}_j) \tag{3.6}$$

$$\Phi_B(\vec{k},\vec{r}) = \frac{1}{\sqrt{N}}\sum_j e^{i\vec{k}\cdot\vec{R}_j}\phi_B(\vec{r}-\vec{r}_B-\vec{R}_j) \tag{3.7}$$

where the exponential factor $\exp(i\vec{k}\cdot\vec{R}_j)$ is a consequence of the Bloch *ansatz*. The normalization factor N represents the number of unit cells in the graphene sheet, $\vec{r}_i$ is the atom site coordinates in the unit cell and $\vec{R}_j$ is a Bravais vectors. In this expressions, ϕ_i denotes the p_z orbital centered on the ith atom site. The sum runs over all the atomic orbitals that are equivalent to ϕ_i by means of a Bravais vector translation.

The tasks consists now to solve the Schrödinger equation

$$\hat{H}\Psi(\vec{k},\vec{r}) = E_k\Psi(\vec{k},\vec{r}) \tag{3.8}$$

where $\hat{H}$ represents the Hamiltonian of the system. The solutions of this eigenvalue equation yields the allowed energies and the coefficients of the corresponding electronic wavefunction. Solving this equation for all momenta within the first BZ fully determines the TB band structure of the crystal. By substituting the LCAO expression of $\Psi(\vec{k},\vec{r})$ and projecting onto the set of Block-like atomic orbitals, one get the following relation

$$\langle\Phi_\beta|H|\left(\sum_\alpha c_\alpha\Phi_\alpha\right)\rangle = E_k\langle\Phi_\beta|\left(\sum_\alpha c_\alpha\Phi_\alpha\right)\rangle \tag{3.9}$$

where α and β stand for the label of a sublattice, i.e. $\alpha,\beta = \{A,B\}$. This equation can be rearranged as

$$\sum_\alpha c_\alpha\langle\Phi_\beta|\hat{H}|\Phi_\alpha\rangle = E_k\sum_\alpha c_\alpha\langle\Phi_\beta|\Phi_\alpha\rangle \tag{3.10}$$

It is convenient to introduce the following notation

$$H_{\beta\alpha} = \langle\Phi_\beta|\hat{H}|\Phi_\alpha\rangle \quad \text{and} \quad S_{\beta\alpha} = \langle\Phi_\beta|\Phi_\alpha\rangle \tag{3.11}$$

where the terms $H_{\beta\alpha}$ and $S_{\beta\alpha}$ represent the Hamiltonian and the overlap matrix elements, respectively.

In the present framework, the Bloch sums are assumed to form an orthogonal basis set. In other words, $S_{\alpha\beta} = \delta_{\alpha\beta}\delta_{k,k'}$. This approximations is reasonable due to the small spatial extension of p_z orbitals in the $\{x, y\}$ plane. It is then straightforward to express the Schrödinger equation in graphene using a matrix formalism

$$\begin{pmatrix} H_{AA}(\vec{k}) & H_{AB}(\vec{k}) \\ H_{BA}(\vec{k}) & H_{BB}(\vec{k}) \end{pmatrix} \begin{pmatrix} c_A(\vec{k}) \\ c_B(\vec{k}) \end{pmatrix} = E_k \begin{pmatrix} c_A(\vec{k}) \\ c_B(\vec{k}) \end{pmatrix} \tag{3.12}$$

with the property that $H_{AB} = H^*_{BA}$, by symmetry.

Let's now write explicitly the diagonal and off-diagonal elements

$$H_{AA}(\vec{k}) = \frac{1}{N} \sum_j e^{i\vec{k}\cdot(\vec{R}_i - \vec{R}_j)} \langle \phi_{A,R_j} | \hat{H} | \phi_{A,R_i} \rangle \tag{3.13}$$

$$H_{AB}(\vec{k}) = \frac{1}{N} \sum_j e^{i\vec{k}\cdot(\vec{R}_i - \vec{R}_j)} \langle \phi_{A,R_j} | \hat{H} | \phi_{B,R_i} \rangle \tag{3.14}$$

where the notation $\phi_{\alpha,R_j} = \phi_\alpha(\vec{r} - \vec{r}_\alpha - \vec{R}_j)$ was introduced. The fundamental question to address in the TB simulations is to ask how far the previous summation runs. The simplest approximation in graphene considers only interactions between an atom and its three nearest neighbors. In this case, one gets

$$\begin{aligned} H_{AB}(\vec{k}) &= \langle \phi_{A,\vec{0}} | \hat{H} | \phi_{B,\vec{0}} \rangle + e^{-i\vec{k}\cdot\vec{a}_1} \langle \phi_{A,\vec{0}} | \hat{H} | \phi_{B,-\vec{a}_1} \rangle \\ &\qquad + e^{-i\vec{k}\cdot\vec{a}_2} \langle \phi_{A,\vec{0}} | \hat{H} | \phi_{B,-\vec{a}_2} \rangle \\ &= -\gamma_0 \left(1 + e^{-i\vec{k}\cdot\vec{a}_1} + e^{-i\vec{k}\cdot\vec{a}_2} \right) \\ &= -\gamma_0 \alpha_k \end{aligned} \tag{3.15}$$

where γ_0 stands for the transfer integral between the first neighbors π orbitals. Typical values for the hopping constant is about $2.9 - 3.1$ eV. The H_{AA} and H_{BB} matrix elements are identical because the two sublattices are composed of carbon atoms. For the sake of simplicity, the on-site energy of carbon atoms is set as the energy reference. The Hamiltonian has therefore the form

$$\hat{H}(\vec{k}) = \begin{pmatrix} 0 & -\gamma_0 \alpha_k \\ -\gamma_0 \alpha_k^* & 0 \end{pmatrix} \tag{3.16}$$

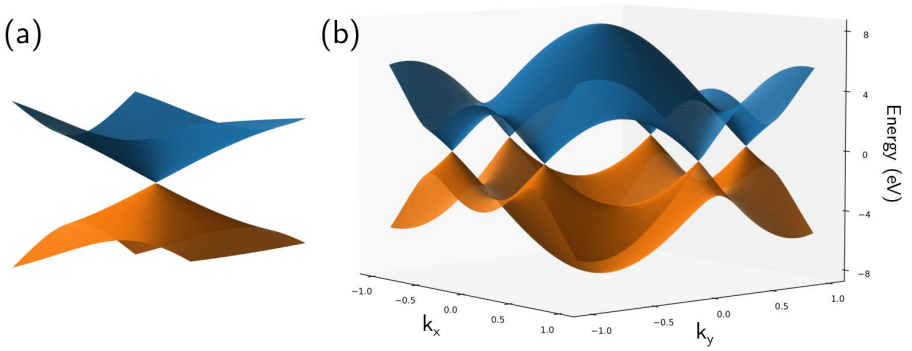

Figure 3.3: Electronic bands of graphene. **(a)** The linear energy dispersion close to the Dirac points gives rise to the "Dirac cones". **(b)** The energy dispersion obtained by a nearest neighbor model is illustrated in reciprocal space as a function of $\{k_x, k_y\}$. The orange and blue curves represent the valence and conduction bands, respectively. Here, $\gamma_1 = 2.8$ eV.

The energy dispersion are obtained by computing the determinant of the matrix $[\hat{H}(\vec{k}) - E_k\hat{S}]$. For an orthogonal basis set, one has $\hat{S} = \hat{I}$. The eigenvalues are therefore expressed as

$$E_k = \pm\gamma_0|\alpha_k| \tag{3.17}$$

$$= \pm\gamma_0\sqrt{3 + 2\cos(\vec{k}\cdot\vec{a}_1) + 2\cos(\vec{k}\cdot\vec{a}_2) + 2\cos(\vec{k}\cdot(\vec{a}_2 - \vec{a}_1))} \tag{3.18}$$

which can be expanded explicitly as

$$E_k = \pm\gamma_0\sqrt{3 + 2\cos\left(k_y a_0\right) + 4\cos\left(k_y a_0/2\right)\cos\left(\sqrt{3}k_x a_0/2\right)}$$

$$= \pm\gamma_0\sqrt{3 + f(\vec{k})} \tag{3.19}$$

where the plus sign applies to the upper (π^*) and the minus sign to the lower (π) band. It is clear that the corresponding energies are symmetric between the valence and conduction bands. Fig.3.3 shows the resulting band structure in the $\{k_x, k_y\}$ plane. In the same figure, a zoom around the Dirac points is also provided (i.e. at the K and K' in the BZ). At those points, the valence and conduction bands cross. Thus, the Fermi surface in neutral graphene is reduced to a finite set of points and is of zero dimension. That is why graphene is neither a semiconductor nor a metal, but is referred to as a zero-overlap semimetal due to its vanishing DoS.

The previous approach can be improved through different manners. First, the interaction between the atoms can be extended to more

distant sites. Although the hopping diminishes exponentially with the distance, the probability that atoms of similar sublattices interact is not zero. Cyclotron resonance experiments found that $\gamma_0^{(2)} \approx .1$ eV for the hopping probability between similar sublattices [122]. Another improvement is to enlarge the basis set by considering different atomic orbitals. A third option is to include the overlap between adjacent atom sites. In the following, the two former approaches are analyzed.

A model that includes interaction to the ith neighboring site is denoted inn. The $1nn$ produces a symmetric band structure, a feature that is removed for approximations beyond the nearest neighbors. If interactions are included up to the next-nearest neighbors, the energy bands have the form

$$E_k = \pm\gamma_0\sqrt{3 + f(\vec{k})} - \gamma_0^{(2)} f(\vec{k}) \tag{3.20}$$

The presence of $\gamma_0^{(2)}$ thus breaks the electron-hole symmetry and shifts in energy the position of the Dirac cone. The third-nearest neighbors orthogonal approximation turns out to be much more efficient than the two previous approaches [123]. The $3nn$ TB model is based on the following Hamiltonian

$$\begin{aligned}\hat{H} = &\sum_i \epsilon_{p_z} |\Phi_i\rangle \langle\Phi_i| \\ &+ \sum_{i,\langle j,k,l\rangle} \left(\gamma_0 |\Phi_j\rangle \langle\Phi_i| + \gamma_0^{(2)} |\Phi_k\rangle \langle\Phi_i| + \gamma_0^{(3)} |\Phi_l\rangle \langle\Phi_i| + h.c.\right)\end{aligned} \tag{3.21}$$

where ϵ_{p_z} is the on-site energy term and the sum on index i runs over all carbon p_z orbitals. The transfer integrals are denoted γ_0. These hopping parameters $\gamma_0^{(n)}$ correspond to a nth nearest neighbors interaction. Note that the notation $\gamma_0 = \gamma_0^{(1)}$ is implied. Similarly, the sum over j, k, l indices runs over all p_z orbitals corresponding respectively to 1st, 2nd and 3rd nearest neighbors of the ith atom site. The parameters are defined such that $\gamma_0 = -3.1$ eV, $\gamma_0^{(2)} = 0.2$ eV, $\gamma_0^{(3)} = -0.16$ eV and $\epsilon_{p_z} = 0.6$ eV, in agreement with Ref.[123]. The resulting band structure computed with the *sisl* software [124] is plotted in Fig.3.4(a).

Lastly, we present the case of a multi-orbitals TB model. In this approach, the σ-bonds are included by considering not only the transfer integrals between p_z orbitals but also between s and p_x, p_y orbitals. The Hamiltonian has the form

$$\hat{H} = \sum_\mu \epsilon_\mu |\Phi_\mu\rangle \langle\Phi_\mu| + \sum_{\mu,\nu} \gamma_{\mu,\nu} |\Phi_\nu\rangle \langle\Phi_\mu| \tag{3.22}$$

Table 3.1: List of some Slater-Koster coefficients, as defined in Ref.[113]. The parameters $\gamma_{i,j}$ are expressed in terms of the direction cosines (l, n, m) and the two-center integrals ($\Gamma_{ij\alpha}$). The p_x, p_y, p_z orbitals are symbolized by x, y, z. The two-center integral $\Gamma_{ij\alpha}$ corresponds to the Hamiltonian matrix element between the i and j orbitals, forming a molecular orbital with angular momentum α around the bond axis.

$\gamma_{s,s}$	$\Gamma_{ss\sigma}$
$\gamma_{s,x}$	$l\Gamma_{sp\sigma}$
$\gamma_{x,x}$	$l^2\Gamma_{pp\sigma} + (1-l^2)\Gamma_{pp\pi}$
$\gamma_{x,y}$	$lm\Gamma_{pp\sigma} - lm\Gamma_{pp\pi}$
$\gamma_{x,z}$	$ln\Gamma_{pp\sigma} - ln\Gamma_{pp\pi}$

where μ combines the pair of indices (i, α) running over all the orbitals and the atom sites contained in the unit cell, respectively. Similarly, the sum over ν corresponds to all the orbitals located on the nearest neighbors of the ith atom site. Contrarily to the π-band approximation, SK parameters (γ_{ij}) are no more equivalent to transfer integrals (Γ). The former are obtained by combining the latter and the direction cosines between the two atoms (denoted l, n, m). Tab.3.1 provides a list of some SK parameters as a function of the transfer integrals. In our multi-orbitals $1nn$ model, $\gamma_{\mu\nu}$ are extracted using the method proposed by McMahan *et al.* [125]. Those SK parameters are in good agreement with values previously reported in the literature [126]. The inclusion of σ-bonds is of particular importance in curved carbon structures where the curvature of the fiber causes a sp^3 hybrization.

3.3 LOW ENERGY LINEARIZATION

The band structure of graphene can be approximated by a linear function at low energy. Close to the Fermi level and the K and K' vectors, Eq.3.19 becomes

$$E_k = \pm\hbar v_F|\vec{q}| + \mathcal{O}\left[(q/K)^2\right] \tag{3.23}$$

where $\vec{q}$ is the momentum measured relatively to the Dirac points. The Fermi velocity (v_F) is the velocity of the electronic wave-packet, given by $v_f = 3\gamma_0 a_0/2\hbar$ (about 10^6 m/s). Importantly, the previous linear relation demonstrates electron-hole symmetry in graphene. The second

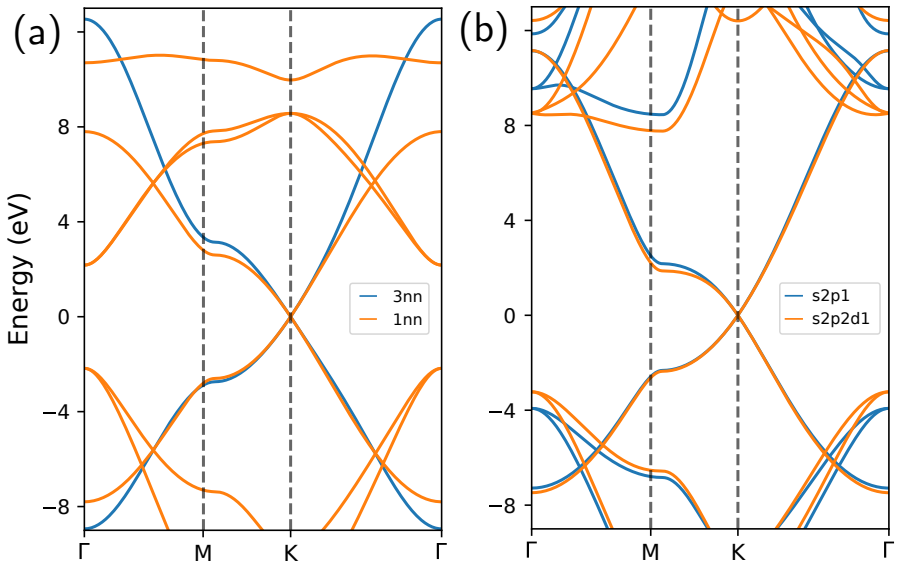

Figure 3.4: Electronic properties of graphene obtained from TB and DFT along the path $[K, \Gamma, M, K]$. **(a)** The computations are performed **(a)** with the *sisl* code using nearest neighbor (*1nn*) and third-nearest neighbors (*3nn*) models for TB and **(b)** with the *OpenMX* code using *s2p1* and *s2p2d1* as basis functions within DFT.

order terms reflects anisotropy in the conical dispersion, reducing the cylindrical symmetry to a threefold symmetry. This is the so-called trigonal warping of the electronic spectrum.

The properties of charge carriers around the Dirac points resemble those of massless Dirac fermions, i.e. particles with zero mass whose dynamics is governed by the Dirac equation. For this reason, K and K' are referred to as Dirac points. This relation appears even more evidently when the linear expansion around K and K' is applied to the Hamiltonian of Eq.3.16

$$\hat{H}_{K,K'} = \hbar v_F \begin{pmatrix} 0 & q_x - iq_y \\ q_x + iq_y & 0 \end{pmatrix} \tag{3.24}$$

Another possibility is to express the Hamiltonian using the Pauli matrices (denoted $\hat{\sigma}$)

$$\hat{H}_{K,K'} = \hbar v_F (q_x \sigma_x + q_y \sigma_y) = \hbar v_F \vec{q} \cdot \hat{\sigma} \tag{3.25}$$

Note that the Pauli matrices operate on the sublattice degrees of freedom and not on spin, as the Hamiltonian matrix elements correspond

to the A and B sublattices. Hence, one refers to Pauli matrices as *pseudospin* operators. Since $\hat{H}_{K,K'}$ depends linearly on $\hat{\sigma}$ at low energy, charge carriers exhibit an helical (or chiral) character[1]. This means that there exists two types of electrons in graphene with opposite pseudospins. Chirality is positive when an electron momentum is parallel to its pseudospin while it is negative when those vectors are antiparallel. This peculiar property has important implications in graphene. For example, electron backscattering requires an inversion of pseudospin due to the coupling of its direction with that of momentum. If the Hamiltonian is not perturbed by a term which flips pseudospin, backscattering is not possible. This particular result is a manifestation of Klein paradox for relativistic electrons.

3.4 FIRST-PRINCIPLES CALCULATIONS IN GRAPHENE

It can be useful to assess how the different TB approximations compare to first-principles calculations. In this regard, the electronic properties of graphene obtained in the framework of DFT are presented in Fig.3.4(b). The calculations are performed with the *OpenMX* code [100, 101, 106]. The pseudo-atomic orbitals used in the LCAO method are defined as sn_s, pn_p, dn_d, where s, p, d denote the type of orbitals while n_i refers to the number of orbitals used in the calculations. The exchange-correlation type is based on the generalized gradient approximation (GGA), as implemented by Perdew-Burke-Ernzerhof (PBE) [127]. Electron-ion interaction are described using Troullier-Martins-type norm-conserving pseudopotentials [128]. The energy cutoff for real-space mesh is set to be at least 300 Ry. Lastly, a fine k-points sampling corresponding to a $33 \times 33 \times 1$ mesh for the graphene unit cell is used.

In order to describe the sp^2 hybridization of carbon atoms, it seems natural to consider first a simple set of functions such as *s2p1*. This basis set proves to be extremely adequate to characterize the properties of planar graphene. In the LCAO framework, a finer degree of accuracy can be obtained by including polarization orbitals. For example, this corresponds to a *s2p2d1* basis set for carbon atoms. The resulting band structure is almost comparable to our previous calculation. Since the role of d-orbitals is negligible in graphene, the slight improvement is presumably due to the increased set of p-orbitals. When graphene

1 For massless particles, helicity and chirality are identical

interacts with atoms containing *d*-orbitals in the outer shell, it may become necessary to employ the *s2p2d1* basis set to describe accurately chemical bonds. Note that free-electron-like conduction bands are absent in the DFT band structure due to the localized nature of the basis functions [129].

Given that DFT computational framework has been addressed, a comparison with TB results is drawn. Concerning the π-bands, the $1nn$ model is observed to be adequate only in the low energy limit, typically below 2 eV. At the contrary, a quite satisfactory agreement is obtained at larger energies for the $3nn$ model, confirming the accuracy of this simple approach. Importantly, the asymmetry between the π- and π^*-bands is well reproduced. It is noteworthy that both approximations fail to give a correct conduction band along the $K - M$ branch [123]. Overall, the low-computational cost of these models enable the description of graphene electronic properties on a micrometer-scale if efficient algorithms are employed [130].

4

METAL-GRAPHENE CONTACTS

As already shown in the introduction, graphene-based materials have become especially attractive for both fundamental and applied research due to their outstanding properties. In a nutshell, the atomic thickness, high carrier mobility and unique band structure of this carbon allotrope make graphene-based materials promising candidates for next-generation electronics [131].

In this context, investigating the key factors degrading the performance of such devices is of the foremost importance. According to several works, the main limitation to graphene-based electronics is not only related to the material quality but also to extrinsic factors. In particular, one of the most parasitic element is the contact resistance appearing between graphene and a metal electrode [58]. Low and reproducible R_c is an imperative requirement for the industrial adoption of 2DMs in electronics. However, measurements of R_c do not provide a consistent picture in the literature, due to current limitations in graphene technology and to an incomplete understanding of influencing factors [132]. Therefore, characterizing the electronic properties of metal-graphene interfaces is both of crucial technological and scientific interest.

As a 2D crystal, graphene is highly sensitive to its environment. When it is adsorbed on a metal surface, the interaction with the substrate can significantly alter the electronic properties of the deposited layer [133]. The discrepancy in work function causes a charge transfer through the interface, which then results in the doping of graphene. Even for a limited charge transfer, a significant shift of the Fermi level (ΔE_F) can occur near the Dirac cone, being either upwards when electrons moves from the metal to graphene (n-doping) or downwards when holes are transferred to graphene (p-doping). The sign and the magnitude of the doping depend on the nature of the metal. Experiments have shown that Ti(0001) surface and Ni, Co and Pd(111) surfaces significantly perturb the electronic properties of graphene whereas it is essentially preserved when adsorbed on Ag, Al, Au, Cu and Pt(111) surfaces [134]. Graphene is found to be n-doped by Ag, Al, Cu, Ti, Co, Ni and Pd whereas it is p-doped when contacted with Au and Pt [135].

Experimental and theoretical studies show that strongly interacting metal electrodes display less contact resistance than weakly interacting ones [132]. Some experiments however reported low contact resistance for weakly interacting metals, even in the side contact geometry [58]. This latter observation is in contradiction with theoretical predictions. Overall, the variations of R_c reported in the literature can be attributed either to intrinsic factors (quality of graphene, metal work functions, doping of graphene) or to extrinsic ones such as the fabrication procedure. In addition, the values of R_c extracted by transfer length measurements or a four-probe method exhibit considerable device-to-device variations, depending on the process conditions. In this regard, there is a debate on the applicability of standard measurement and extraction techniques to obtain dependable and correct data [136]. Importantly, inhomogeneous doping profiles in the graphene channel lead to erroneous values of R_c when conventional extraction methods are used. A comprehensive overview is thus needed, such that R_c can eventually be extracted accurately and reproduced in a reliable and repeatable manner.

In metal-graphene nano-junctions, two components contribute to the total current: [137] (i) vertical transmission from the metal electrode to graphene (T_{mg}) and (ii) in-plane transport inside the graphene channel (T_g). Fig.4.1(a) illustrates the cascaded transport mechanisms in a graphene-based FET. If some practical issues (edges termination, contacts area, defects, ...) are disregarded, T_{mg} depends solely on two fundamental factors: (i) the metal electronic structures and (ii) the nature of the interaction at the metal-graphene interface. Whereas the former aspect is an inherent material property, the latter is governed by the difference in work function as well as by the type of molecular orbitals involved. Importantly, T_{mg} is a transmission process from a bulk phase to a 2D crystal. Most theoretical works however assume graphene to couple to metal electrodes made of thin films [132, 138–146]. In essence, these models do not describe accurately T_{mg} due to finite-size-induced modifications in the metal electronic structure. It is also troublesome to discriminate between T_{mg} and T_g in the thin-film configuration. Lastly, little diversity in the definition of the surface unit cells is reported in the literature while it was shown to substantially affect T_{mg} for certain metals [147]. To the best of our knowledge, no theoretical work on metal-graphene junctions has yet addressed accurately those concerns. This observation is even more striking if ones considers the large number of studies on 2DMs-based vertical devices [148].

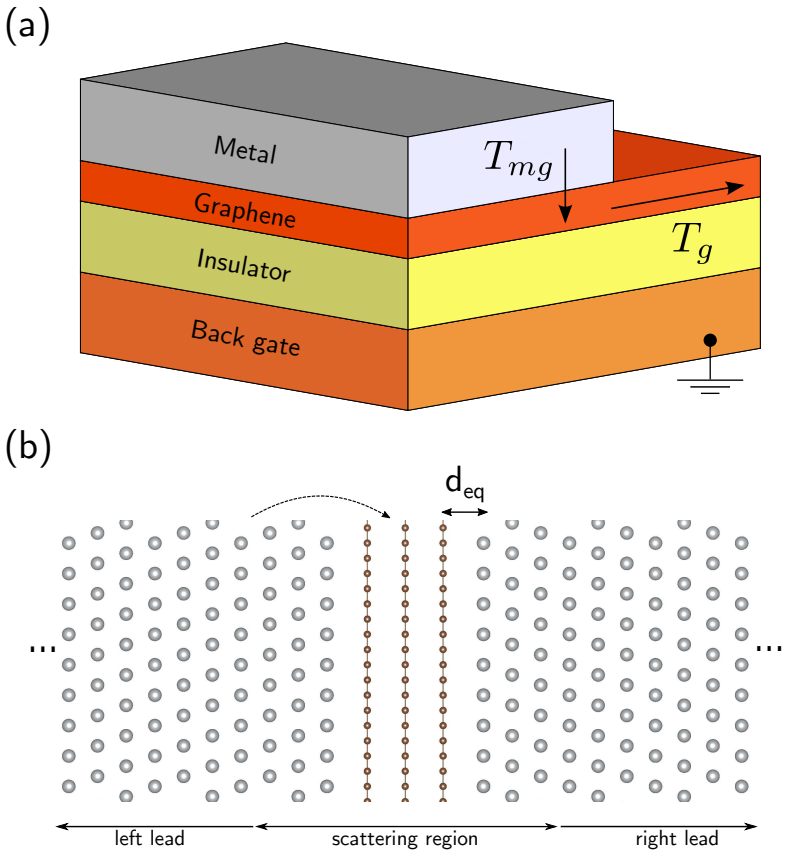

Figure 4.1: Schematic illustration of the key parameters used to model graphene-based devices. **(a)** Layer-by-layer representation of a vertical heterostructure FET based on graphene. The cascaded transport process is represented schematically by two transmission probabilities T_{mg} and T_g. **(b)** Side view of a vertical heterostructure of trilayer graphene (TLG) encapsulated between two semi-infinite metallic leads. The first three metallic layers are fully relaxed whereas atoms away from the interface remain in their bulk position. The distance between the outermost graphene layer and the metallic surface is denoted as d_{eq}. Electrons are injected and collected in the left and right semi-infinite electrodes, respectively (indicated by the dotted line).

This context appeals for an in-depth investigation of T_{mg} in metal-graphene systems. In this chapter, we present an *ab initio* study of electronic transport through junctions of trilayer graphene (TLG) confined between two semi-infinite metallic leads. This configuration is illustrated in Fig.4.1(b). Importantly, this structural model is assumed to be transposable to the analysis of R_c for single layer graphene. On the one hand, the number of graphene layers needs to be sufficiently large to avoid any spurious interaction between the leads. On the other hand, charge carriers need to experience a similar environment compared to metal-graphene contacts and the graphene system must display a conical dispersion at low energy. As demonstrated later on, TLG-metal junctions meet those requirements. A systematic approach is applied to different metals (Al, Ag, Au, Cr, Cu, Pd, Ti) to elucidate the nature of the interaction at the metal-graphene interface in Sec.4.1. For physisorbed TLG, the Fermi level shift is studied using a simple analytical model in Sec.4.2, which characterizes the metal only in terms of its work function [133]. This phenomenological model is then applied in Sec.4.3 to more realistic metal-graphene interfaces that reproduce more closely experimental observations. Afterwards, the vertical injection of charge carriers is computed using first-principles simulations, as presented in Sec.4.4. This analysis is restricted to physisorbed systems owing to the substantial modification of the electronic properties of chemisorbed graphene, which would impede its integration in nano-scale devices. In order to gain further insights into the transport mechanisms at play, a semi-empirical transport model is constructed in Sec.4.5 from our *ab initio* data. This model is based on two ingredients: the correspondence in electronic structures and the overlap in atomic orbitals. Finally, the transport characteristics of realistic metal-graphene interfaces are estimated in Sec.4.6 using this semi-empirical model. In a nutshell, this theoretical work aims to provide a comprehensive analysis of the structural, electronic and transport properties of metal-graphene junctions based on first-principles methods.

The electronic properties of metal-TLG junctions are computed based on the same approach than in Sec.3.4. A *s2p2d1* basis set is used for carbon atoms to accurately describe interfacial interactions with the metal surface. The basis functions of the metals are carefully designed to reproduced the band structures obtained with the linearized augmented-plane-wave method [149]. In the case of Cu, the radial functions of basis orbitals are variationally optimized using the orbital optimization method [100, 101]. Long-range vdW dispersion forces are

included using Grimme's DFT-D3 empirical corrections [150], such that the underbinding of GGA is accounted for.

4.1 TRILAYER GRAPHENE ON METAL SURFACES

At first, the interfacial properties of TLG (Bernal stacking) on metal substrates (Ag, Al, Au, Cr, Cu, Pd, Ti) are studied. All calculations are performed on metals in the face-centered cubic structure (fcc) even though Cr and Ti are most stable in the body-centered cubic and hexagonal closed-packed arrangements, respectively. The corresponding lowest-energy surface orientation is the (111) crystallographic direction [151]. Spin-unpolarized calculations are performed as no metal is magnetic in its ground state.

As illustrated in Fig.4.2(a), a minimal 1×1 surface unit cell is used for Cu and Cr whereas the $\sqrt{3} \times \sqrt{3}$ surface unit cell is employed for the other metals. The depicted configurations constitute an appropriate initial guess for metal-graphene interfaces before structural optimization. A small strain is applied to TLG to accommodate for the lattice mismatch, such that the band structure of TLG is marginally affected [152]. The binding equilibrium distance (or van der Waals distance, denoted d_{eq}) is obtained after structural optimization of the junction with a force criterion of 2×10^{-4} Ha$/a_0$, where a_0 is the Bohr radius. It is defined as the average distance of innermost graphene to the metal surface. The binding energy between TLG and the metal is

$$E_b = (E_{mg} - (E_{tlg} + E_m))/N \tag{4.1}$$

where E_{mg}, E_{tlg} and E_m are the energy corresponding to the metal-graphene system, TLG and the clean metal slab, respectively. The number of interfacial carbon atoms is denoted as N. The potential energy curves of TLG deposited on a metal slab are shown in Fig.4.2(b) while the optimized lattice parameter with the resulting stretch to graphene, the equilibrium distance and the binding energy are listed in Table.4.1. Note that those optimized structures constitute a reasonable approximation to metal-graphene interfaces but are not representative of experimental observations. This comment is addressed in detail in Sec.4.3.

In general, the strength of the metal-graphene interaction depends on the number of d electrons in the transition metal, the size of those orbitals (which sets the overlap with the π-cloud of graphene) and the work function difference with graphene [134]. Those junctions are classified

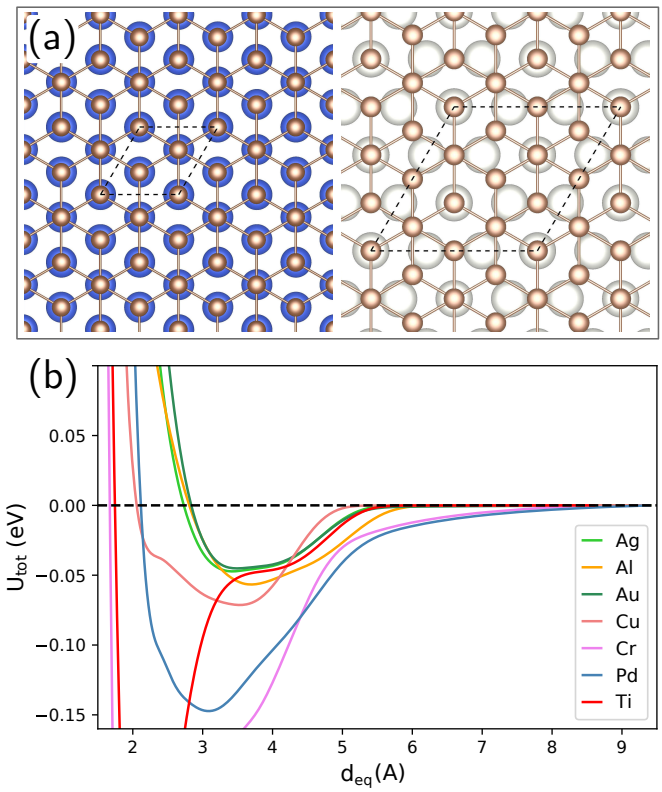

Figure 4.2: Structural characterization of TLG (light-brown atoms) adsorbed on a metal substrate (blue and white atoms). **(a)** (Left) The minimal 1×1 unit cell used for Cr(111) and Cu(111). (Right) The $\sqrt{3} \times \sqrt{3}$ unit cell employed for Ag(111), Al(111), Au(111), Pd(111) and Ti(111). The orientation of the metal surface with respect to the graphene sheet differs by 30° in the two cases. **(b)** Potential energy profiles of TLG on the metal surfaces as a function of the metal-graphene separation (d_{eq}). The energy minima of Cr(111) and Ti(111) are not shown due to the discrepancy between the adsorption regimes.

Table 4.1: Calculated lattice parameter (a_0), strain (ϵ_0) applied to graphene and interface equilibrium distance (d_{eq}) upon adsorption of TLG on the (111) metal surface. The equilibrium distance is defined as the average distance of innermost graphene to the metal surface. The binding energy (E_b) is the energy per carbon atoms in the innermost layer required to remove TLG from the surface. The respective Fermi level shift (ΔE_F) and the metal work function (W_m) are listed in case of physisorption or weak chemisorption. The theoretical metal work functions for the (111) surface are compared to the experimental ones (W_m^{exp}).

	Ag	Al	Au	Cr	Cu	Pd	Ti
a_0 (A)	2.986	2.911	2.975	2.593	2.581	2.834	2.940
$\epsilon_y = \epsilon_z$ (%)	3.86	1.25	3.46	4.14	3.65	-1.45	2.25
d_{eq} (A)	3.43	3.65	3.42	2.01	3.45	3.10	2.06
E_b (meV)	47	58	46	704	71	159	417
ΔE_F (eV)	-0.36	-0.35	-0.03	×	-0.24	0.0	×
W_m (eV)	4.43	4.10	5.32	×	4.88	5.31	×
W_m^{exp} (eV)	4.46[a]	4.26[b]	5.26[c]	×	4.94[d]	5.55[e]	×

[a]Ref.[153], [b]Ref.[154], [c]Ref.[155], [d]Ref.[156], [e]Ref.[157]

into three different categories depending on d_{eq} and E_b [158]. First, physisorption occurs when interfacial effects are weak. It is characterized by $d_{eq} > 3$ Å and $E_b < 150$ meV. In the contrary, chemisorbed TLG strongly binds to the surface with $d_{eq} < 2.5$ Å and $E_b > 200$ meV. The third category is defined as a weak chemisorption where both d_{eq} and E_b occupy an intermediate spectrum. It follows that TLG is physisorbed for Ag, Al, Au and Cu while a strong chemisorption occurs in the case of Cr and Ti. An intermediate situation is observed for Pd where TLG is found to be weakly chemisorbed. Other theoretical works have reported similar values for d_{eq} and E_b using similar functionals [159–161].

In order to assess the modifications to the electronic structure of TLG induced upon adsorption, the band structures of metal-TLG junction are presented in Fig.4.3 for Al, Ag, Au, Cu and Pd. The energy dispersion of free-standing TLG is provided for comparison. At low energy, Bernal TLG has one pair of linear bands and two pairs of parabolic bands stemming from its symmetry [162]. The Dirac-type dispersion is a consequence of the interaction between the outer layers stacked

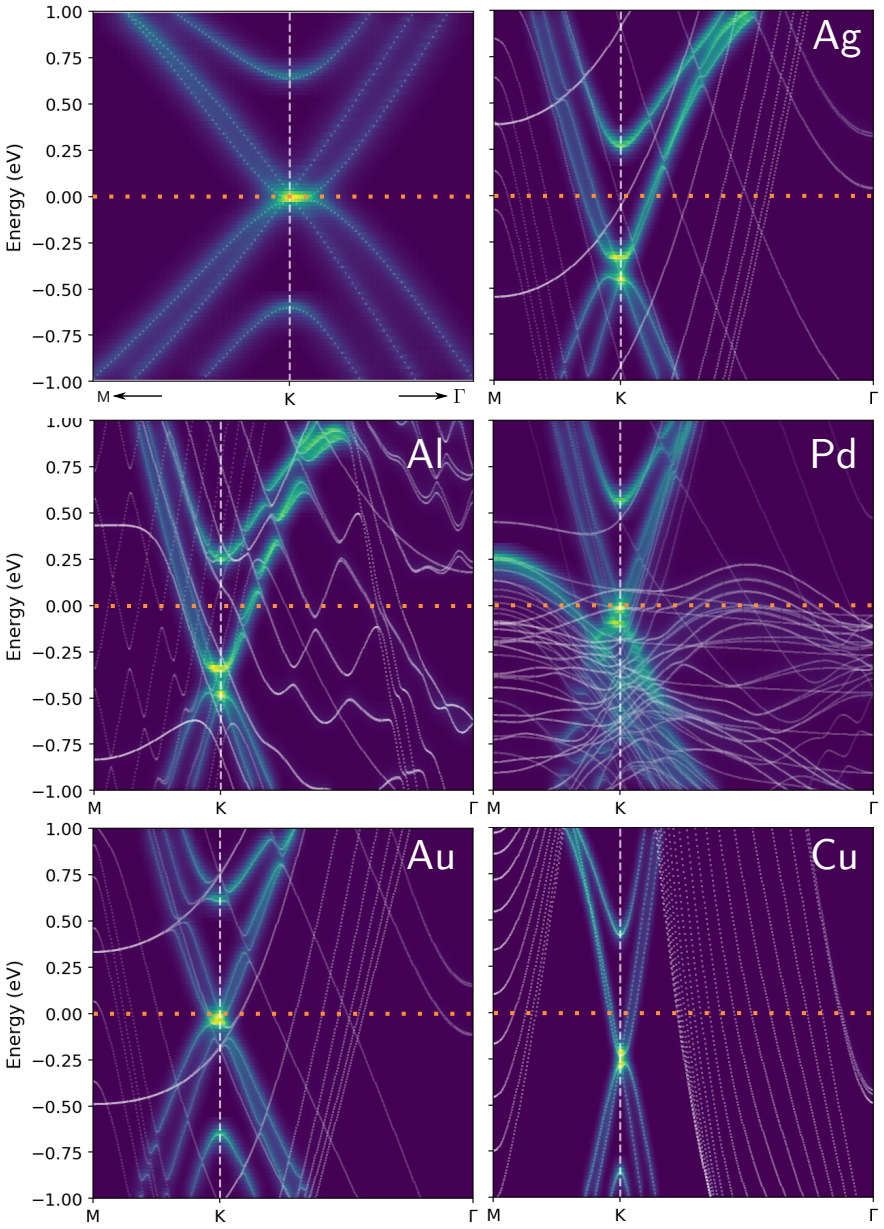

Figure 4.3: Electronic properties of TLG upon physisorption or weak chemisorption. The band structures of free-standing TLG and TLG physisorbed on Ag, Al, Au, Cu and Pd on (111) surfaces are represented. The Fermi level is set to zero (horizontal dashed line). TLG projected bands (green) are plotted against the total band structure (white).

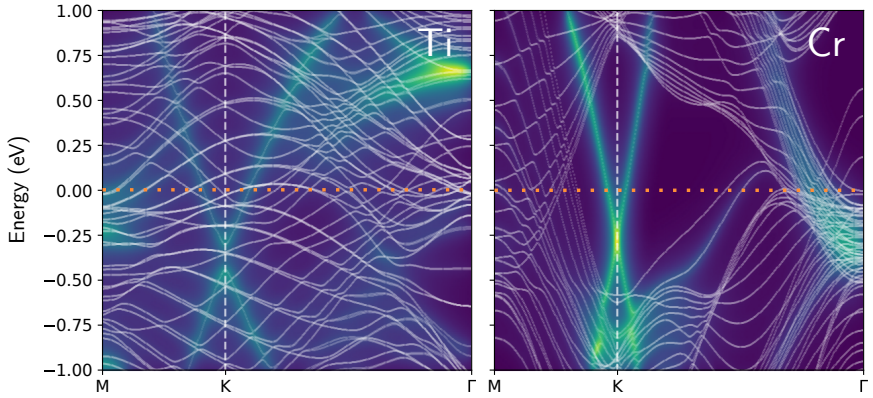

Figure 4.4: Electronic properties of TLG upon chemisorption. The band structures of TLG chemisorbed on Ti and Cr on (111) surfaces are represented. The Fermi level is set to zero (horizontal dashed line). TLG projected bands (green) are plotted against the total band structure (white).

on top of each other. The quadratic dispersion results from the interaction between the inner and the outer layers as in the case of bilayer graphene [163]. At the Fermi level, the pair of parabolic bands crosses the pair of linear bands at the *K* point. Hence, Bernal TLG behaves as a semimetal.

When the interaction is weak (Ag, Al, Au and Cu), the electronic structure of TLG is well conserved and both linear and parabolic bands are clearly identifiable. However, those bands do not necessarily cross each other at the Fermi level as adsorption generally shifts the Fermi level of TLG. A shift upwards (downwards) corresponds to a transfer of electrons (holes) from the metal substrate to graphene which becomes n-type (p-type) doped. In the case of Pd, weak chemisorption induces a mixed graphene-metal character while TLG electronic structure is still discernible.

In the case of chemisorption, the bands of TLG are strongly perturbed and acquire a mixed graphene-metal character [133], as illustrated in Fig.4.4 for Ti and Cr. Although the conical dispersion is preserved for the innermost layer, the carbon orbitals of the outermost layers are completely hybridized with the metal surface. There is therefore little to no sense to define doping owing to the strong contrast in electronic structures. In addition, the electrostatic environment of such metal-TLG interface is not representative of the corresponding metal-graphene contacts as the innermost layer induces spurious effects. In those contacts, the vertical injection of charge carriers is not predominantly

determined by the electronic structures of the isolated metal and the uncontacted graphene. For those reasons, Ti and Cr are not considered in the following.

At equilibrium distances, a significant n-type doping for Ag, Al, and Cu is observed whereas the situation is less clear for Au and Pd. The ambiguity stems from the doping difference between the innermost and outermost layers. After analyzing the DoS of the innermost layer, it is found that Au is only slightly n-doping while TLG is almost undoped on Pd. The Fermi level shift is defined as the difference between the identifiable crossing of parabolic bands (the middle of the band gap if a band gap is opened) ($\tilde{E}_{tlg}$) and the Fermi level of the metal-TLG system

$$\Delta E_F = \tilde{E}_{tlg} - E_F \tag{4.2}$$

The corresponding values are listed in Tab.4.1. To draw a comparison with other theoretical works, it is essential to point out beforehand that ΔE_F is substantially influenced by the exchange-correlation energy functional (E_{xc}). The amount of charge transferred to graphene depends on the electron density and the equilibrium distance which are both function of E_{xc} [164]. Zheng *et al.* [158] conducted an extensive investigation on the interfacial properties of bilayer and trilayer graphene on metal substrates using a GGA-PBE functional with a DFT-D semi-empirical dispersion-correction approach. A n-type doping was reported for Ag, Al, Cu and Pd while Au is p-doping for Bernal TLG. A general observation is that ΔE_F computed in the present work is lower in comparison to the Fermi level shift presented in Ref.[158] (except in the case of Pd). This means that more electrons are transferred from the metal to TLG. This larger charge exchange stems from the symmetric structure used in our study (see Fig.4.1(b)), where two electrodes are considered in contrast with the one contact geometry used in most theoretical works [133, 158, 161, 165, 166]. A significantly smaller d_{eq} is another possible source of discrepancy. All things considered, our results are consistent with the values of ΔE_F reported in the literature [167].

A rigorous explanation of the relation between charge transfer, the equilibrium distance and the Fermi level shift is provided in following.

4.2 DOPING OF GRAPHENE ON METAL SURFACES

In the following section, the doping of graphene is characterized when it interacts with the metal substrate. Naively, one would expect doping

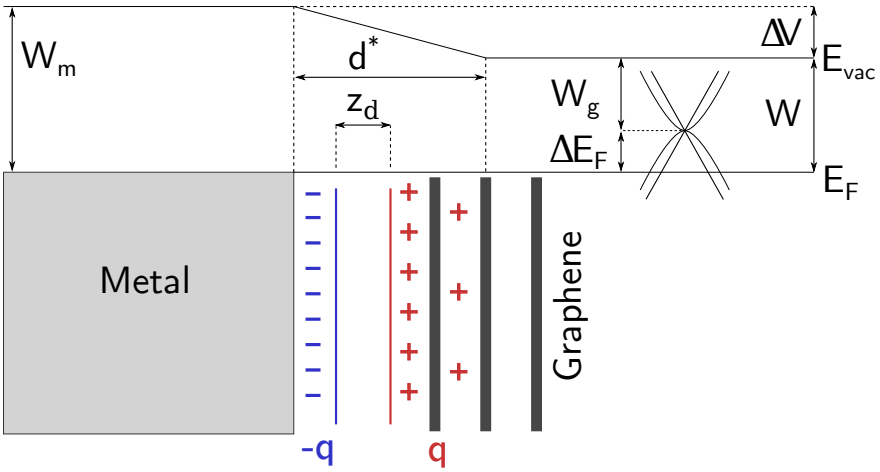

Figure 4.5: Schematic illustration of the parameters used to model doping at the metal-graphene interface. The vacuum energy (E_{vac}) is set as the energy of reference. The work function difference between graphene (W_g) and the metal surface (W_m) causes a transfer of charge (q) to equilibrate the Fermi levels (E_F). The work function of contacted graphene (W) is affected upon adsorption due to this charge transfer. The electronic redistribution results in the formation of a potential step (ΔV) that is modelled by a planar capacitor of separation z_d. The charge transferred to TLG is located on the first and second layers at most at a distance d^* to the metal surface. Charge doping induces a rigid shift of the Fermi level (ΔE_F) of the band structure with respect to the crossing of parabolic and linear bands of pristine TLG.

to solely depend on the difference between the work functions of free-standing TLG (W_g) and the clean metal surface (W_m). This simple picture is however significantly altered by the presence of an interfacial charge redistribution and a corresponding potential step ΔV. As soon as graphene interacts with the metal surface, electrons are transferred from one to the other to equilibrate the Fermi levels due the difference in work functions. The subsequent Fermi level shift (ΔE_F) takes place almost entirely in graphene since its DoS is significantly smaller than the one of a typical transition-metal. The adsorbed graphene work function (W) changes in proportion to doping and is defined by the position of the Fermi level with respect to the vacuum level (E_{vac}). A schematic representation is shown in Fig.4.5.

The Fermi level for physisorbed graphene

An analytical model of doping is derived hereafter in the case of physisorbed graphene using the aforementioned parameters. If the metal-graphene interaction is weak, graphene electronic structure is preserved and it ensues that

$$\Delta E_F(d) = W(d) - W_g \tag{4.3}$$

Khomyakov *et al.* [135] demonstrated that this relation is valid for relatively large separation ($d = 5.0$ Å) while a small deviation of about 80 meV is expected at typical equilibrium distances ($d \approx 3.3$ Å). This discrepancy emerges from the perturbation of the graphene electronic structure due to physisorption. This deviation is disregarded in the following as the typical parabolic and linear bands of TLG are assumed to shift rigidly upon adsorption. It was also shown that the interfacial electron redistribution has the shape of a dipole. In consequence, a planar capacitor model is used in order to describe the potential step (ΔV). This potential profile at the interface is not only dependent on the charge transfer that equilibrates the Fermi levels but also results from a contribution related to the direct interaction between the metal and graphene. A general expression of the potential step is

$$\Delta V(d) = \Delta_{tr}(d) + \Delta_c(d) \tag{4.4}$$

where Δ_{tr} represents the direct charge transfer driven by the difference in work functions and Δ_c characterizes the short range interaction due to the wave function overlap between the metal surface and graphene. The electron transfer term is thus modeled as a planar capacitor. From Gauss's law, the electrostatic potential between the plates is defined as

$$\Delta_{tr}(d) = \frac{e^2 N_q(d) z_d}{\epsilon_0 A} \tag{4.5}$$

where e is the elementary charge, $N_q(d)$ is the number of transferred electron (per graphene unit cell), z_d is the effective distance between the charged sheets, ϵ_0 is the vacuum dielectric constant and A is the graphene unit cell area. Note that $N_q(d)$ is defined to be negative if electrons are adsorbed by graphene. The effective distance is defined from the localization of charges at the interface. In the symmetric metal-TLG junction, charge carriers are primarily exchanged between the metal and the first and third sheets. The central layer is also doped

although not as much as the outer sheets. This means that z_d is smaller than the distance d^* between the metal surface and the second layer of TLG (see Fig.4.5). The effective distance is expressed eventually in terms of the separation as $z_d = d - d_0$ where d_0 is a constant. It is typically assumed that $d_0 = 2.4$ Å [135, 168]. As concerns the contribution from the wave function overlap, it is expected to vanish exponentially with increasing metal-graphene separation. Indeed, the wave function in the metal is an extended Bloch wave within the crystal with an exponentially decaying tail outside the surface. Khomyakov *et al.* [135] therefore proposed the following relation

$$\Delta_c(d) = e^{-\tau d}\left(a_0 + a_1 d + a_2 d^2\right) \tag{4.6}$$

where τ, a_0, a_1 and a_2 are parameters that should be fitted to data. Although more complex vdW functionals could provide a more accurate description of Δ_c, its asymptotic behavior is disregarded as it is negligible for large separation. Now that the interfacial potential step has been characterized, the adsorbed graphene work function is conveniently expressed as

$$W(d) = W_m - \Delta V(d) \tag{4.7}$$

where the change in the graphene work function is consistent with the sign and the amount of charge transferred to the system. In order to write down analytically the Fermi level shift, an additional relation is required. The DoS in graphene is fairly approximated for low-energy charge carriers by $D(E) = D_0|E|$ with $D_0 = 0.09/(\text{eV}^2 \text{ unit cell})$. The averaged number of electrons transferred to a graphene layer is then obtained by integrating the DoS from the neutrality point

$$\begin{aligned} N_q &= \int_0^{\Delta E_F} D(E)dE \\ &= \text{sign}(\Delta E_F)\frac{1}{2}D_0 \Delta E_F(d)^2 \end{aligned} \tag{4.8}$$

which is a function of the Fermi level shift only. Note that it was assumed that the electronic temperature tends to zero in order to solve the integral analytically. Solving the set of equations from Eq.4.3 to Eq.4.8 leads to the following phenomenological model for the Fermi level shift

$$\Delta E_F(d) = \pm \frac{\sqrt{1 + 2\alpha D_0 \left(d - d_0\right)\left|W_m - W_g - \Delta_c(d)\right|} - 1}{\alpha D_0 \left(d - d_0\right)} \tag{4.9}$$

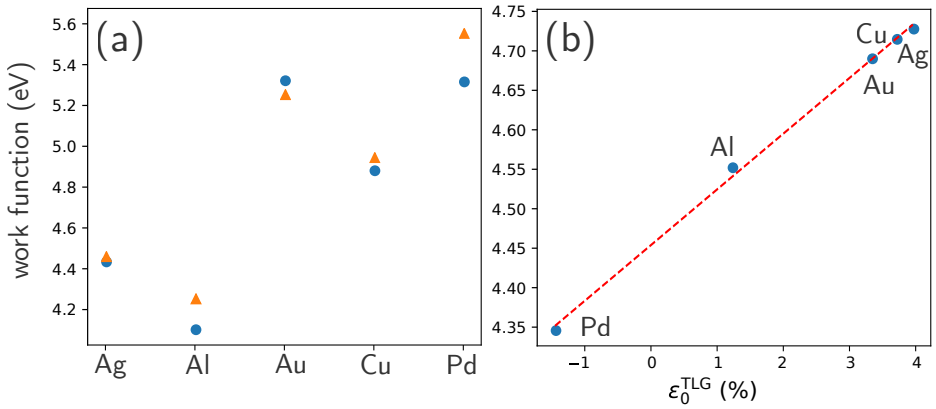

Figure 4.6: First-principles calculations of the materials work functions in metal-TLG junctions. **(a)** Comparison between the theoretical estimations (blue sphere) and the experimental measurements (orange triangle) of the metal work function for Ag [153], Al [154], Au [155], Cu [156] and Pd [157]. **(b)** The dependence of the work function of TLG on various strain profiles is also given.

where $\alpha = e^2/\epsilon_0 A = 36.2$ eV/A. The sign of ΔE_F is determined by the sign of $W_m - W_g - \Delta_c(d)$. This model was demonstrated to describe effectively metal-graphene junctions [133, 135] as well as metal-insulator-graphene heterostructures for which the dielectric constant needs to be adjusted accordingly [168, 169]. The graphene and metal work functions are obtained through *ab initio* techniques. As it concerns the metal work functions, our theoretical estimations are listed in Tab.4.1 and compared to experimental values from the literature. Fig.4.6(a) illustrates the comparison between theory and experiment. A qualitative agreement is reported, with a slight deviation of 0.24 eV for Pd. It is however important to point out that measurements reported in the literature often cover a considerable range of values, as the work function depends on various factors such as the surface cleanliness or the methods of measurement [170]. A work function of 4.45 eV is reported for pristine TLG, in agreement with the experimental values of 4.30 eV and 4.70 eV for graphene and graphite, respectively [171]. This is consistent with the theoretical estimation of 4.43 eV for TLG obtained by Leenaerts *et al.* [172]. Note that W_g is sensitive to the amount of strain applied to graphene. We report a linear dependency of W_g for small deformations, as illustrated in Fig.4.6(b).

Applicability to metal-TLG junctions

As stated above, the foregoing model was developed in the case of metal-graphene junctions while the present analysis is concentrated on metal-TLG junctions. Hence, it is essential to assess the assumptions made so far that are possible sources of discrepancy. A first deviation originates from the thickness dependence of the electronic structure of graphene. Single-layer graphene is a zero-gap semiconductor with a linear Dirac-like spectrum around the Fermi level while graphite is a semimetal. As concerns Bernal TLG, it was demonstrated that its DoS is quite similar to the one of graphene within ± 1 eV around the Fermi level [173]. Therefore, it is still reasonable to assume $D(E) = D_0|E|$ and the solution to the integral for the average number of electrons remains valid. To confirm this statement, N_q adsorbed on the middle layer is extracted from first-principles calculations and compared to its expected value for a system with a linear DoS. The resulting comparison is depicted in Fig.4.7(f). A qualitative agreement is observed, with the exception of Pd where the deviation is presumably due to a larger modification of its electronic structure. Note that it is a somewhat ambiguous issue to assign an effective charge to each atom. A Mulliken population analysis [174] was employed in this work. It should also be noted that N_q is extracted on the second layer so that the Mulliken analysis is not affected by bonding or charge redistribution at the interface. A second source of complexity in modeling the doping in metal-TLG systems resides in the localization of charge upon adsorption. In order to describe ΔV using a planar capacitor, electron redistribution needs to be shaped in the form of a dipolar charge distribution. This electronic redistribution is well visualized using the charge difference density

$$\Delta Q(x) = Q_{mg}(x) - \big(Q_m(x) + Q_{tlg}(x)\big) \tag{4.10}$$

where x is the direction perpendicular to the interface, $Q_{mg}(x)$, $Q_m(x)$ and $Q_{tlg}(x)$ are the average charge densities of the metal-TLG junction, the clean metal surface and free-standing TLG, respectively. Note that the isolated geometries are obtained from the structurally optimized junctions. The resulting $\Delta Q(x)$ are depicted in Fig.4.7(a-e) for TLG physisorbed on Ag, Al, Au, Cu and Pd, respectively. The charge difference density $\Delta Q(x)$ extracted from our *ab initio* simulations is quantitatively comparable to the ones reported for metal-graphene junction for Al, Ag, Au and Cu in Ref.[135]. A salient feature in the charge redistribution is an accretion and a depletion in electronic

density on the metal surface and the first graphene sheet, respectively. This result points to the use of a planar capacitor model to describe the potential step in the case of metal-TLG junction. It is also observed that the transferred charge is located first and foremost between the surface and the first graphene layer. A direct consequence is that z_d is expected to be smaller than the equilibrium distance since the charge is primarily localized between the surface and the first graphene layer. Importantly, the significant correlation between $\Delta Q(x)$ around the middle layer and N_q support the consistency of the current approach.

The values of ΔE_F are extracted for a range of metal-graphene separations using first-principles calculations and the phenomenological model is then fitted to those points using the parameters d_0 and $\Delta_c(d)$ (see in Fig.4.8(a)). It was demonstrated in Ref.[135] that a unique set of parameters for Δ_c and d_0 is applicable to every metal. That is to say that those parameters depend only very weakly on the metal substrate. In this analysis, standard values of $\tau = 1.2$ Å^{-1} and $d_0 = 2.4$ Å are used, in agreement with previous theoretical works [135, 168], while a_0, a_1 and a_2 were optimized in each case to produce the best fit. It remains an open question if this loss of generality on the polynomial expansion comes from the methodology employed or stems from the electronic deviation of TLG compared to graphene. A possible source of discrepancy lies in the estimation of ΔE_F from the second layer while Δ_c and Δ_{tr} are related to the interaction between the innermost layer and the substrate. This issue is nevertheless disregarded as our first and foremost objective is to accurately describe the Fermi level shift. An error of less than 25 meV is reported when estimating ΔE_F for every metal except Cu, which has an error of 65 meV. This larger deviation might be explained either by the optimized nature of the basis set or by the type of primitive cell used for Cu. As one carbon atom sits on top of a metal atom while the other does not, an imbalance between the two sublattices of graphene appears and the accuracy of the fit of ΔE_F decreases due to the opening of a band gap (E_g) [175]. Similarly, E_g is increased by an accretion of charge in the middle layer (as measured by N_q). Although charge is essentially distributed between the substrate and the contacted layers in the form of a dipole, a perceptible amount of electrons are transferred to the middle layer. This charge imbalance results in a potential drop between the external layers and the middle layer such that band gap is opened in the parabolic bands [176]. Those remarks indicate the extent to which the phenomenological model is valid. For physisorbed (or weakly chemisorbed) TLG, the model holds

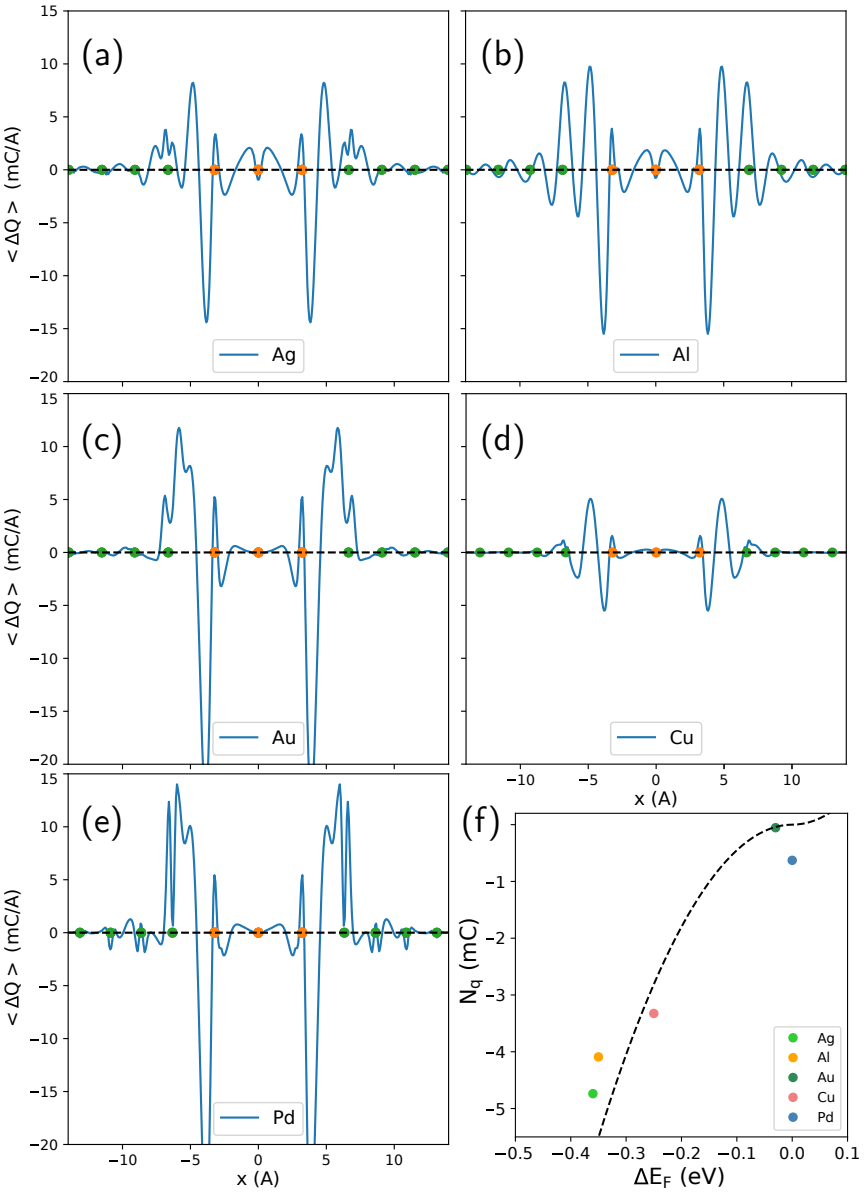

Figure 4.7: First-principles calculations of the charge transferred to TLG upon adsorption on a metal substrate. **(a-e)** Averaged charge difference density ($\Delta Q(x)$) illustrating the charge redistribution after adsorption. The atomic positions are indicated along the transport direction (x) for metal and carbon atoms (green and orange dots, respectively). **(f)** The averaged number of electrons (N_q) (per graphene unit cell) transferred to the middle layer of TLG is plotted as a function of the Fermi level shift (ΔE_F). N_q has been estimated from a Mulliken population analysis using *ab initio* methods while the analytical expression for a linear DoS is drawn for comparison (dashed black lines).

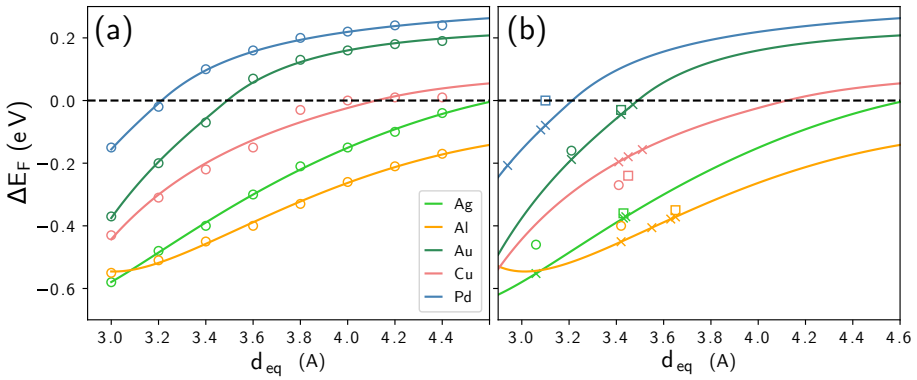

Figure 4.8: Fermi level shifts (ΔE_F) as a function of the metal-graphene separation (d_{eq}) due to the interaction with various metal substrates. The phenomenological model (Eq.4.9) is shown for comparison (solid lines). **(a)** In the case of the minimum unit cell, ΔE_F is directly extracted from *ab initio* calculations (circles). **(b)** Comparison between the predicted ΔE_F for different metal surfaces (crosses) and first-principles results for the (100) and (111) surfaces (in circles and squares, respectively). For the latter, ΔE_F is computed within the Green's functions formalism.

for energies where the DoS is linear and the charge transferred is small enough not to open a significant band gap. The corresponding criterion is that $E_g \ll \Delta E_F \leq 1$ eV, which remains valid for the considered metals (see Fig.4.3). Lastly, one must insist on the limited range of accuracy of pseudo-atomic localized basis functions compared to plane waves. Romero *et al.* showed that PAO basis sets are accurate in the physisorbed regime where binding occurs by dispersion forces [177], thus defining the upper bound for the present analysis to 5 Å.

4.3 DOPING OF GRAPHENE ON REALISTIC METAL SURFACES

We have described metal-graphene interfaces so far using the minimal surface unit cells. Such configuration often leads to a substantial deviation from the initial unit cell of graphene and is not consistent with most experimental observations performed using electron microscopy. In practice, the interaction at the interface and the lattice mismatch with the substrates lead to the emergence of a biaxial strain in graphene. It is energetically unfavorable to form a coherent interface due to the large energy cost of such deformation, with the exception of Co(0001) [178] and Ni(111) [179] where the lattice mismatch is minimal. Metal-graphene interfaces are hence characterized by Moiré

patterns which manifest as well-ordered periodic modulations throughout graphene that relax strain arising from lattice incommensurability. This structural relaxation also occurs perpendicularly to the surface as the graphene layer undergoes a slight out-of-plane deformation with similar periodicity, meaning that d_{eq} varies spatially as well. The Moiré structures of commensurate systems are described by a periodicity and a rotation angle. The periodicity is obtained from the number of hexagonal units in graphene matching the surface cells of the substrate. The formation of Moiré patterns has been observed for a series of transition metals [167] such as Al [180], Au [181, 182], Cu [183] and Pd [184]. The metal-graphene interaction is also dependent on the substrate crystallographic orientation which profoundly impacts the the corresponding interface hybridization [134]. Each crystallographic facet is characterized by a specific mismatch with the honeycomb lattice of graphene that determines the periodicity and orientation angles of the Moiré structure. In consequence, the present analysis has been extended to different interfacial arrangements and surface orientations. First, a larger cell is defined for the (111) surface where graphene is rotated by 19.1° with respect to the substrate. The (100) crystallographic orientation is then examined as it has one of the lowest surface energy in fcc metals [151, 170]. A more exotic $(1\bar{1}1)$ facet is also considered in order to investigate further the effects of hybridization at the interface. The structural parameters of those cells are presented in Tab.4.2, where strain is limited to 4 %.

The larger cell for the (111) crystallographic orientation is represented in Fig.4.9(a-b), with an strain profile equivalent to the minimal unit cell. The discrepancy between the larger and minimal cells lies in the orientation of the graphene layers with respect to the metal surface. The hybridization reordering at the interface is observed not to modify noticeably the binding energy nor the equilibrium distance. That is to say that TLG interacts homogeneously with the substrate upon adsorption, no matter its relative orientation, similarly to graphene sheets in turbostatic graphite. It is therefore assumed that the independence of E_b and d_{eq} on the Moiré structure comes from the closed-packed nature of the (111) surface, which is the most efficient way of packing atoms within a single layer. In other words, the high density of metal atoms at the surface creates a uniform orbital hybridization with the p_z orbitals of graphene.

The cells for to the (100) and $(1\bar{1}1)$ crystallographic orientations are illustrated in Fig.4.9(c-g). The corresponding potential energy curves

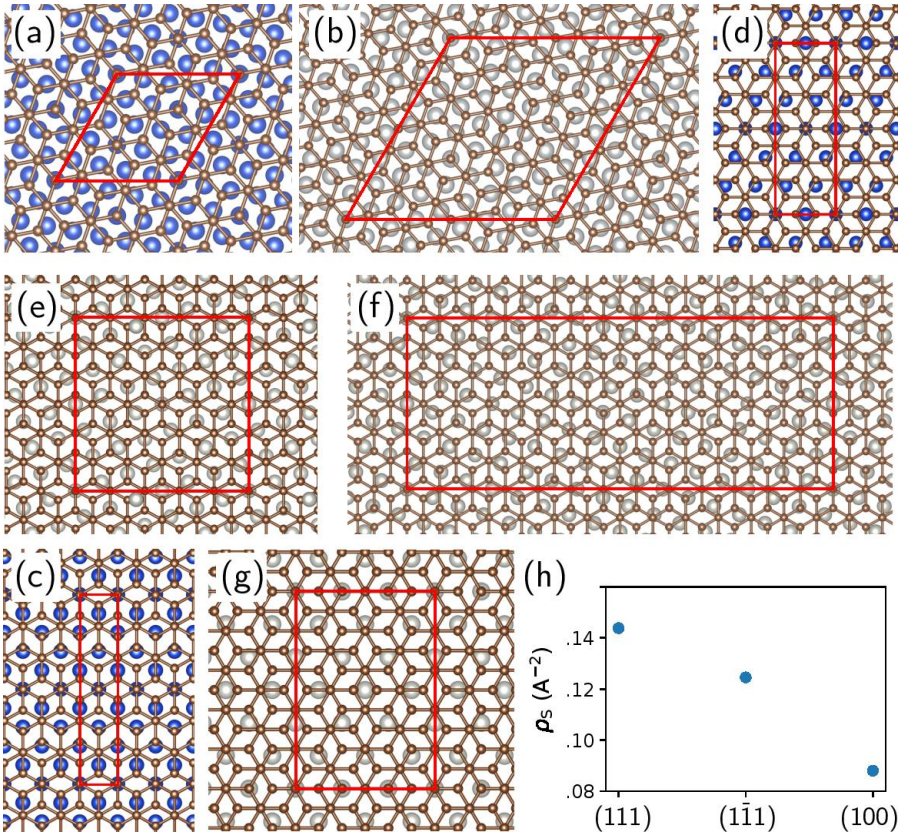

Figure 4.9: Atomistic models for the adsorption of TLG on a metal substrate at different crystallographic orientations. **(a-g)** Top view of the metal-TLG interface with the unit cell shown in red. Atoms in blue represent Cu atoms while atoms in silver characterize Ag, Al, Au or Pd atoms. **(a-b)** Supercells used for the (111) surface. The orientation of the surface with respect to the graphene sheet differ by 19.1° in the two cases. **(c-e)** Supercells for the (1$\bar{1}$1) surface. For clarity, **(d)** and **(e)** are referred as the α and β configurations, respectively. **(f-g)** Supercells used for the (100) surface. **(h)** The surface density (ρ_S) is represented for each crystallographic direction.

Table 4.2: Calculated strain (ϵ_y, ϵ_z) applied to graphene, interface equilibrium distance (d_{eq}) and binding energy (E_b) upon adsorption of TLG on (100), $(1\bar{1}1)$ and (111) metal surfaces. The respective experimental work functions (W_m^{exp}) are listed for TLG physisorbed on the (100) surface. In the case of $(1\bar{1}1)$, the two configurations for Pd are denoted Pd^{α} and Pd^{β}.

	Ag	Al	Au	Cu	Pd	
(111)						
$\epsilon_y = \epsilon_z$ (%)	3.86	1.25	3.46	3.65	-1.45	
d_{eq} (A)	3.44	3.63	3.47	3.51	3.08	
E_b (meV)	47	55	46	69	160	
(100)						
(ϵ_y, ϵ_z) (%)	$(1.7, 3.8)$	$(-0.8, 1.2)$	$(1.3, 3.4)$	$(3.7, 0.2)$	(-3.4,-1.4)	
d_{eq} (A)	3.06	3.42	3.21	3.41	2.55	
E_b (meV)	52	75	52	70	200	
W_m (eV)	4.08	4.08	5.07	4.56	4.75	
W_m^{exp} (eV)	4.22[a]	4.20[b]	5.22[c]	4.59[d]	5.65[e]	
$(1\bar{1}1)$					Pd^{α}	Pd^{β}
(ϵ_y, ϵ_z) (%)	×	$(0.5, 0.6)$	×	$(1.6, 3.7)$	$(-2, 1.7)$	$(-2.1, -2.1)$
d_{eq} (A)	×	3.55	×	2.85	2.65	2.94
E_b (meV)	×	87	×	81	180	160

[a]Ref.[153], [b]Ref.[154], [c]Ref.[155], [d]Ref.[156], [e]Ref.[185]

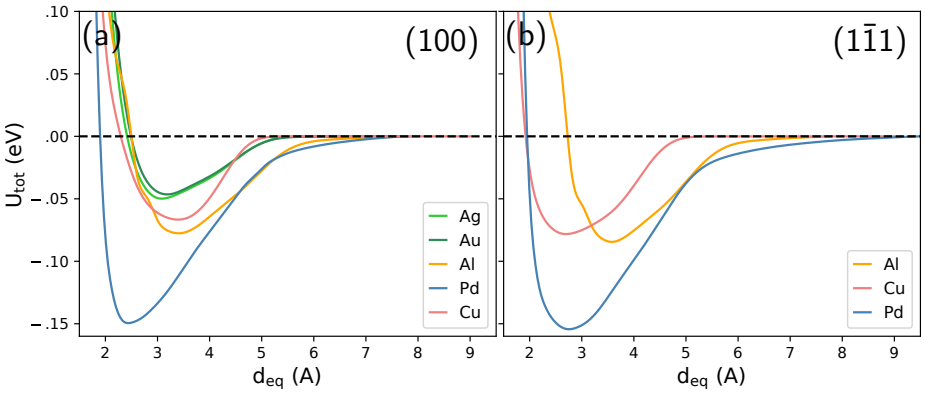

Figure 4.10: The potential energy profiles of TLG adsorbed on metal as a function of the metal-graphene separation (d_{eq}) for the **(a)** (100) and **(b)** (1$\bar{1}$1) surfaces.

are displayed in Fig.4.10. A stronger adsorption is reported for the (100) surface, with a general shift of the potential energy curves. The change in orbital hybridization modifies the equilibrium configuration compared to the (111) surface: E_b is found to increase while d_{eq} decreases. In the case of Pd, chemisorption is much more prominent compared to the $\sqrt{3} \times \sqrt{3}$ unit cell. Similarly, TLG interacts more strongly when adsorbed on the (1$\bar{1}$1) surface. Oddly enough, Pd^{α} and Pd^{β} show substantial differences in adsorption strength, even though identical orbitals and crystallographic orientation are involved.

In a nutshell, the crystallographic orientation is observed to affect the structural parameters of the metal-graphene interface. As atoms are packed less efficiently at the surface (see Fig.4.9(h)), interfacial hybridization yields a more heterogeneous energetic landscapes that depends more strongly on structural parameters. This means that metal-graphene interfaces are defined over a range of separations, whose prevalence is determined by the energetic stability of the corresponding crystallographic facet. The case of Pd is of particular interest. Since Pd is known to easily mix with carbon to produce carbide phases [166], its weak chemisorption regime is more sensitive to its respective arrangement with the graphene layer.

After the structural characterization of metal-graphene junctions, the Fermi level shift of the (100) crystallographic orientation is compared to the analytical model obtained for the minimal unit cell for the (111) surface. The (1$\bar{1}$1) systems are disregarded due to their large scale size or to their strong adsorption regime for which the phenomeno-

logical model does not hold anymore. It stands to reason that ΔE_F changes depending on the nature of the surface. On the one hand, the substrate crystallographic orientation affects the work function by reshaping the dipole barrier at the clean metal surface. In transition metals, one has the following relation: $W_m^{(111)} > W_m^{(100)}$ [170]. The experimentally measured work functions are listed in Tab.4.1 and Tab.4.2 for comparison, while theoretical estimations are provided. Except for $Pd(100)$, theoretical predictions are quite accurate. On the other hand, switching from the (111) surface to the (100) surface impacts interfacial hybridization. The modification of the orbital overlap is accounted for in Eq.4.9 through the parameter Δ_c. It has been formerly shown that $\tau \approx 1.2$ Å^{-1} and $d_0 = 2.4$ Å characterize well the orbital overlap in metal-graphene junction, independently of the substrate. This means that the dependence of the Fermi level shift on the crystallographic orientation is determined by the variation of a_0, a_1 and a_2 in the short range and by the decrease in work function in the long range.

The values of ΔE_F for the (100) systems are plotted in Fig.4.8(b) and compared to the phenomenological model. A very good agreement is obtained for intermediary distances, while an noticeable deviation is reported at shorter metal-graphene separations (i.e. for Ag(100)). In the latter instance, the discrepancy originates from a substantial modification in orbital overlap. At larger equilibrium distances, the reduction in work function is observed not to impact doping. Overall, the analytical model to estimate ΔE_F is considered to be transferable to other crystallographic orientations.

In conclusion, the structural and electronic characteristics of realistic graphene-metal interfaces were analyzed using first-principles techniques. The phenomenological model given by Eq.4.9 was shown to be quite universal, as long as the correct metal-graphene separation is provided. As detailed in the forthcoming sections, the variation of d_{eq} for different crystal surfaces has a profound impact on the transport properties. The corresponding change in doping magnitude is one example among others.

4.4 QUANTUM TRANSPORT IN METAL-TLG JUNCTIONS

The objective of the following section is to gain insights into the main mechanisms at play when charge carriers are injected from the metal electrodes into graphene. To this end, it is sensible to examine ballistic

conductances obtained within the Landauer-Buttiker linear response theory [88, 89]

$$G = R_c^{-1} = \frac{2e^2}{h} \int -T(E) \frac{\partial f}{\partial E} \left(\frac{E - E_F}{k_B T} \right) dE \tag{4.11}$$

where h is Planck's constant, k_B is Boltzmann's constant, T is the temperature, f is the Fermi-Dirac distribution and $T(E)$ is the transmission coefficient. From the previous relation, the conductance quantum is defined as $G_0 = e^2/2$. An accurate description of $T(E)$ is therefore fundamental to properly address the contact resistance. Altogether, the transmission coefficient at energy E is obtained as an average over the 2D BZ of the surface unit cell

$$T(E) = \frac{A}{(2\pi)^2} \int_{BZ} T(E, k_\perp) dk_\perp \tag{4.12}$$

where A is the cell cross-sectional area and $k_\perp$ is the momentum (perpendicular to transport) of the incident Bloch state. Inelastic processes such as phonon scattering are not considered since it clearly goes beyond the scope of the present study. The k-resolved transmission coefficient is expressed in Green's function formalism (see Eq.2.37)

$$T\left(E, k_\perp\right) = \mathrm{Tr}\left\{ \Gamma_r \mathcal{G} \Gamma_l \mathcal{G}^\dagger \right\} \tag{4.13}$$

where Γ_i is a matrix that represents the coupling between the electrodes and the junction. The retarded (advanced) Green's function $\mathcal{G}$ ($\mathcal{G}^\dagger$) is a wave function object that propagates an electronic states injected in the left (right) electrodes through the junction. This formalism has provided accurate results for the transport characterization of metal-graphene junctions [132].

Transport processes in graphene-based devices

In graphene-based devices, the total transmissions reads [186]

$$T_{tot} = T_{mg} T_g / \left[1 - \left(1 - T_{mg} \right) \left(1 - T_g \right) \right] \tag{4.14}$$

which corresponds to two cascaded processes determined by T_{mg} and T_g (see Fig.4.1(a)). Charge carriers are at first injected from the metal to the graphene underneath it, then transported inside the graphene channel. The dependency of the total transmission on T_{mg} and T_g is illustrated in Fig.4.11(a). It is apparent that one needs both transmissions to be effective in order to induce a large total transmission.

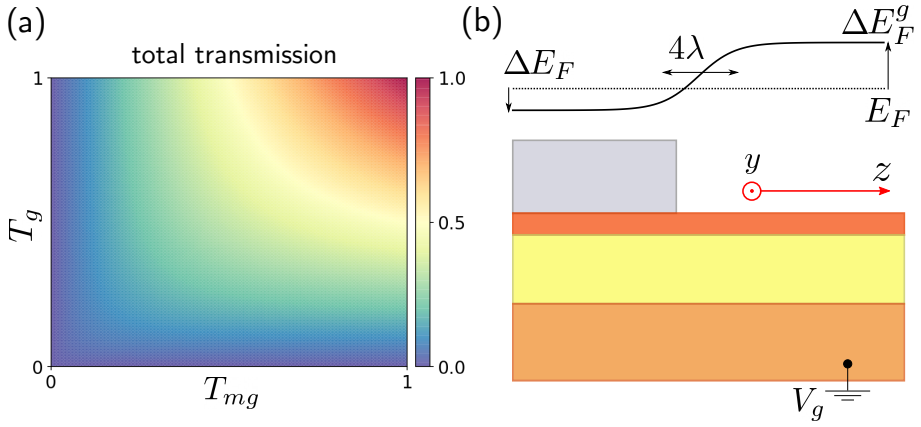

Figure 4.11: Quantum transport in metal-graphene junctions. **(a)** Evolution of the total transmission probability for a cascaded process with transmission probabilities T_{mg} and T_g. **(b)** Potential step profile in a standard graphene-based device, with an effective length λ. The Fermi level shift under the metal and deeply in the channel are denoted ΔE_F and ΔE_F^g, respectively. The potential profile is shifted by applying a back-gate (V_g).

A controlling factor for injection from the metal and transport inside the graphene channel is the doping resulting from charge transfer between metal and graphene. Importantly, the number of modes available for transport in the channel is determined by the shift of the Fermi level. At the metal-graphene junction, ΔE_F is accurately characterized using the phenomenological model (Eq.4.9). Once transmitted inside the graphene channel, charge carriers experience a space-dependent potential [187]

$$\Delta E_F(z) = \Delta E_F + \frac{\Delta E_F^g - \Delta E_F}{\exp(-z/\lambda) + 1} \tag{4.15}$$

where z indicates the distance from the metal contact (located at $z < 0$), λ represents the potential effective length and ΔE_F^g is the asymptotic Fermi level shift in the graphene channel (see Fig.4.11(b)). Different doping profiles (p-p', n-n' or p-n) are then obtained by applying a back gate, depending on the Fermi level shift at the metal-graphene junction. Typical values of λ range from a few nanometers to several tens [169]. Chaves *et al.* [188] showed that the potential effective length depends strongly on the dielectric environments both above and below graphene.

The tunneling probability inside the graphene channel (T_g) is then determined by the width, shape and height of the potential and by

the carrier incident angle [187]. At normal incidence, backscattering is suppressed due to Klein tunneling, independently of the potential height and width [189]. While p'-p and n-n' potential barriers are nearly transparent, p-n junctions can induce significant scattering depending on the incident angle and on the back-gate [137]. The interested reader is invited to read Ref.[190] for a detailed and thorough analysis of T_g.

On the contrary, a fundamental and comprehensive understanding of T_{mg} is still lacking due to the more complex nature of charge injection. Some theoretical models have provided an insightful interpretation of R_c but failed to present an accurate estimation of T_{mg}. The injection probability is either fit in accordance with experimental results [137] or obtained from approximated solutions to Schrodinger's equation [169, 191]. In addition, most *ab initio* studies used the inadequate thin-film geometry, whose thickness is no more than 1 nm. Hereafter, the current state of the art of charge injection from metal contacts into graphene is reviewed.

Charge injection in metal-TLG junctions

As mentioned above, T_{mg} is a transmission process from a bulk to a 2D material that depends on the metal electronic structure and on the physics at the junction. The latter dependence is affected by manifold parameters: the work function difference, the molecular orbitals involved, the presence of point defects, the contact area and the edge terminations. In their seminal work, Karpan *et al.* [192] demonstrated the importance of electronic states correspondence in reciprocal space between graphene and Ni for spin filtering. Kuroda *et al.* [147] subsequently explored the conductance dependence on the number of graphene layers for Al, Au, Cu, Pd and Ti contacts. They found that T_{mg} decays exponentially with increasing film thickness for some metals while it saturates for others after a few layers. This difference stems from the match/mismatch in crystal momentum giving rise to distinct behaviors depending on how Fermi surfaces are folded into the smaller BZ of the $\sqrt{3} \times \sqrt{3}$ unit cell. In the case of sufficiently thin films (i.e. single and bilayer graphene), the bonding between the metal and the graphene innermost layer is the predominant contribution to charge injection. The interaction at the junction influences T_{mg} in several manners depending on the adsorption regime and the nature of the interface. Barraza-Lopez *et al.* [141] performed calculations on graphene suspended between Al contacts and characterized the doping

variation along the channel using an analytical model. Charge transfer at the leads is identified as the dominant factors for charge injection whereas almost no sensitivity to the graphene orientation is observed, in agreement with the later work done by Maassen *et al.* [142] for Cu contacts. Also for Cu contacts, Liu *et al.* [143] analyzed the impact of molecular orbitals involved to find that their respective symmetry determines the effectiveness of T_{mg}. A systemic first-principles analysis was carried out by Ma *et al.* [193] on the dependence of R_c on the graphene edge terminations, contact area and point defects. Strongly interacting metals were reported to show small sensitivity to those factors, in agreement with the earlier work of Stokbro *et al.* [145]. It was also found that edges without chemical terminations and point defects decrease R_c for weakly interacting metals whereas hardly any effect of the contacted area was observed. In contrast, Liu *et al.* [194] found that an increased contact area leads to an enlarged charge injection in the case of Cu. This enhancement is however caused by a shift in transmission due to larger charge transfer and little to no contact-area dependence was reported on T_{mg}.

All things considered, some significant comments are required. First, nearly all *ab initio* studies have only considered the minimal unit cell due to computational constraints. Such small surface cell is however not representative of realistic metal-graphene nano-junctions, as more complicated Moire patterns are expected to emerge when graphene and the metal surface come in registry. Importantly, the surface cell determines the folding of the Fermi surfaces into the smaller BZ and therefore the match/mismatch in crystal momentum between metal and graphene. The polycrystalline nature of metal contacts has also been disregarded in the literature. It was shown previously that the substrate orientation shapes the orbital overlap at the junction and subsequently impacts the Fermi level shift through an adjustment of the equilibrium configuration. To the best of our knowledge, no theoretical work has addressed the influence of those factors on T_{mg} . Last but not least, almost all first-principles analyses explored the transport properties of metal-graphene junctions for a restricted set of metals, while (physisorbed) graphene is predicted to interact distinctively depending on the molecular orbitals involved. The lack of in depth *ab initio* investigations of R_c on an extensive array of metals makes it difficult to draw a comprehensive conclusion on the predominant transport mechanisms. In addition, the difference in methodology between the theoretical works complicates a full comparison.

The aforementioned remarks are addressed in the following manner. In addition to the minimal unit cell, the transport properties of the previously-defined supercells are investigated. The influence of the Moiré patterns on charge injection for $\theta = 19.1^\circ$ and $\theta = 30^\circ$ is explored for the (111) surface while interfacial hybridization effects are examined for the (100) and $(1\bar{1}1)$ crystallographic orientations. The geometry presented in Fig.4.1(b) is employed to avoid the limitations related to the thin-film structure, meaning that the contacts (leads) are well characterized and that lateral transmissions are disregarded. In this configuration, TLG is enclosed between two leads. Charge carriers are injected from the left electrode and collected in the right one after tunneling through TLG. The scattering region in each lead is defined to be longer than 2 nm, such that spurious interactions are avoided. The transposability of this model to the analysis of single layer graphene was already demonstrated. The conical dispersion is preserved and the electrostatic environment of the model approximates well metal-graphene contacts. It is important to point out that our objective is not so much to accurately predict the least resistive contact but rather to explain the discrepancies in experimental measurements of R_c.

At first, the transmissions for the minimal unit cells are computed within the Green's function formalism (see Fig.4.12(a)). Two recurring features are observed, independently of the metal. First, the Fermi level of TLG is shifted, as indicated by the relative position of the zero conductance. It is useful to compare ΔE_F obtained from Green's functions with the phenomenological model (Eq.4.9) constructed from thin-films calculations. Overall, a fine agreement is reported in Fig.4.8(b), although a noticeable deviation of 60 meV and 80 meV is observed for Cu and Pd, respectively. While this discrepancy is within the analysis margin, a convincing explanation is still missing. The transmission also depends on the DoS of the metal, which is depicted in Fig.4.12(c). If one compares Pd to other metals, $T(E)$ is much larger for the injection of holes while the difference is less important for electrons. In addition, the linear band dispersion of graphene is plainly perceptible for all metals except Cu. This suggests that TLG acts as filtering barrier in the former while it behaves as a transparent barrier in the latter. The two transport mechanisms are presented in Fig.4.12(d). In the case of Al, transmissions are well approximated by a linear function. On the contrary, $T(E)$ in Cu-graphene nano-junction decreases by a constant factor compared to bulk transport in Cu. The absence of a linear feature

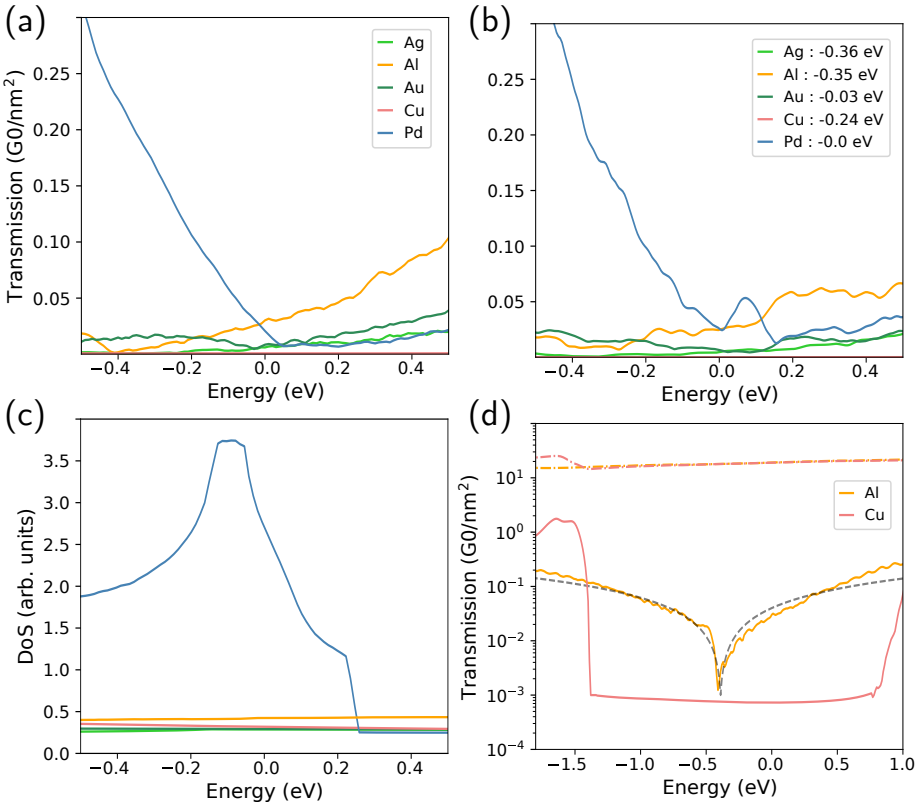

Figure 4.12: First-principles electronic transport through metal-TLG junctions for the minimal surface unit cell in the case of physisorption or weak chemisorption. Electronic transmissions per unit area as a function of energy computed using **(a)** Green's function formalism and **(b)** the empirical transport model (Eq.4.16), with the listed relative doping of TLG. **(c)** DoS of the corresponding metals. **(d)** Comparison of the electronic transmissions per unit area as a function of energy between metal-TLG systems (solid lines) and the isolated metal contacts (dot-dashed lines) for Cu and Al. In the latter case, electronic transport is adequatly described by a linear dependency on the energy (dashed lines).

and the larger diminution in transmissions compared to Al indicates that graphene acts as a vdW gap in this case.

Interestingly, the configuration depicted in Fig.4.1(b) is similar to the graphene-based hot electron transistor [195, 196] (GB-HET), where graphene is used as the base due to its ultimate thinness and high conductivity. In an elementary implementation of the GB-HET, Zhu *et al.* [148] demonstrated that graphene acts as a nearly transparent tunneling barrier. The barrier transparency originates from the material atomic thinness and the transverse momentum mismatch between graphene and the emitter. The explanation for the considerably lower $T(E)$ is hence to be found in the metal electronic structure and the epitaxial relation with graphene. In this respect, the energy surface in momentum space projected onto the $\{k_y, k_z\}$ plane is illustrated in Fig.4.13. The evaluation is performed at $E - E_F = 0.5$ eV. In the graphene film, the states in the low-energy regime are confined at the K and K' corners of the 2D BZ. At the same energy level, Cu has no states near the K-points while other metals do. Therefore, any incident state incoming from the contact couples to evanescent modes and decays exponentially in the film if there is a significant crystal momentum mismatch [147]. The role of the epitaxial relation between the metal and graphene is thus of the foremost importance. This is well illustrated in the cases of Au and Cu, where tunneling probabilities are dissimilar even though the electronic structures are quite similar. It then becomes essential to address the influence of the Moiré patterns on the transport properties of metal-graphene junctions. Such structures are unfortunately not analyzable by means of Green's functions due to their large size (too many atoms in the unit cell), thus requiring a different approach. In this context, a semi-empirical transport model is developed in the following.

4.5 TRANSPORT MODEL IN METAL-TLG JUNCTIONS

In a nutshell, the transport model accounts for three contributions: (i) the electronic structures and the epitaxial relationship, (ii) the Fermi level shift and (iii) the interfacial coupling at the metal-TLG interface. The phenomenological expression for transmissions is then given as

$$T(E) = \gamma_0 e^{-\kappa\left(d-d_{eq}\right)} \frac{1}{N_{k_\perp}} \sum_{k_\perp} f^m(E, k_\perp) f^{Gr}(E + \Delta E_F, k_\perp) \qquad (4.16)$$

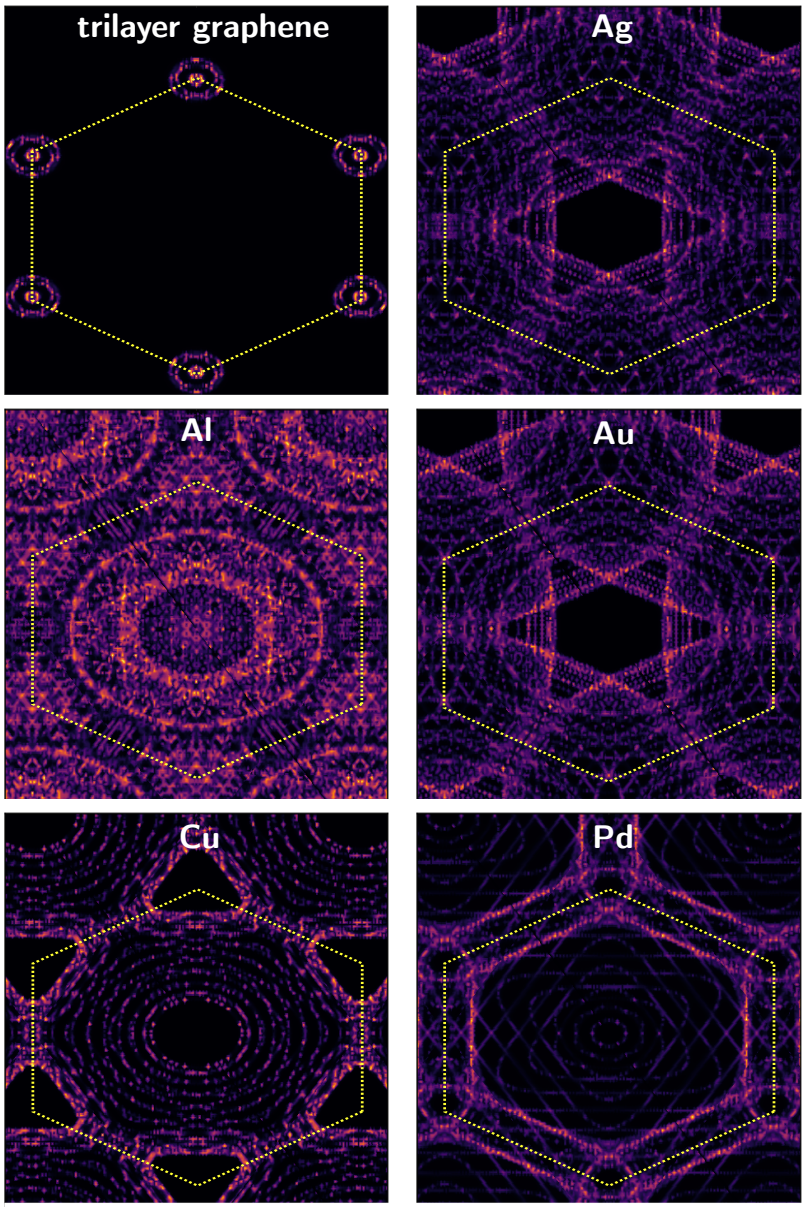

Figure 4.13: Energy surface in momentum space projected onto the $\{k_y, k_z\}$ plane for free-standing TLG and Ag, Al, Au, Cu and Pd. The transverse momentum (k_z) corresponds to the transport direction in the metal-TLG configuration. The energy surface is evaluated at 0.5 eV from the respective Fermi level. Hexagons mark the edge of the 2D BZ.

where γ_0 and κ characterize the coupling at the interface while $f(E, k_\perp)$ describes the electronic properties of the pristine materials. The doping of TLG is included by considering the shifted electronic structure at $E' = E + \Delta E_F$. Tunneling probabilities are therefore expressed as the product of the two following functions

$$\gamma(d) = \gamma_0 e^{-\kappa\left(d - d_{eq}\right)} \tag{4.17}$$

$$\xi(E) = \frac{1}{N_{k_\perp}} \sum_{k_\perp} f^m(E, k_\perp) f^{Gr}(E + \Delta E_F, k_\perp) \tag{4.18}$$

where each contribution is assumed to be independent of the other.

The parameter $\gamma(d)$ incorporates a combination of complex physical phenomena occurring at the junction, such as orbitals localization or the charge carriers tunneling rate. In essence, it represents the effectiveness of the orbital overlap between graphene and the metal on the transmission probabilities. This coupling function is energy-dependent and *a priori* unknown. In the following, $\gamma(d)$ is assumed to be energy-independent due to the weak interaction at the interface and the type of molecular orbitals involved. In the low energy regime, TLG is described by the (almost unperturbed) p_z orbitals while the metal exhibits parabolic bands which are characteristic of a free-electron gas. The dependence of $\gamma(d)$ on the metal-graphene separation is included through the parameter κ, which reflects the sensitivity of T_{mg} on the chemical bonding length. A distinction is made further on between the behavior of κ in the asymptotic limit (κ_0) and at shorter distances (κ_1). The functional form of Eq.4.17 is inspired by the previously-discussed short-range interaction (Δ_c). The exponential term is introduced as a perturbation to γ_0, which corresponds to the coupling in the configuration at equilibrium.

As electronic states of contacted graphene acquire a finite width due to the coupling with the metal electronic states [197], f^{Gr} and f^m are modeled as Lorentz functions of full width at half maximum 2β centered around the graphene and metal eigenvalues, respectively. The electronic structure coefficient is therefore expressed as

$$\xi(E) = \frac{1}{N_{k_\perp}} \sum_{k_\perp} \prod_i \frac{1}{N^i} \sum_j \frac{2\beta}{\left(E - E_j^i\right)^2 + \beta^2} \tag{4.19}$$

where i denotes a given material (metal or TLG), j runs over all available states at given transverse momentum $k_\perp$ and N^i is the number of

Table 4.3: Transport parameters extracted from transmission from metal electrodes through TLG. The effective interfacial coupling at the equilibrium sepatation (γ_0) and the tunneling probability logarithmic rate of change (κ_0) in the asymptotic regime ($d \geq 4.4$ Å) are given as a function of the metal.

metal:	Ag	Al	Au	Cu	Pd
γ_0 (mG$_0$)	10	27	33	4	30
κ_0 (A^{-1})	2.5	3.1	3.5	3.8	3.4

atoms in the cell of the ith material. The epitaxial relationship due to band folding onto the smaller 2D BZ is then naturally accounted for when computing the eigenstates of the supercell Hamiltonian. A more refined approach would be to consider the complex band structure in order to describe evanescent states, in addition to the propagating ones for which $[\mathrm{Im}(k_x) = 0]$. Although generalized Bloch states are important for understanding the electronic nature of solid surfaces and interfaces, $\xi(E)$ offers a simple and efficient modeling of the momentum match/mismatch, as demonstrated afterwards.

In summary, Eq.4.16 enables a direct interpretation of $T(E)$ using a phenomenological approach, where metals that are preferable to others for injecting charge carriers are characterized by an efficient interfacial coupling and a good correspondence in transverse momentum.

The transport model is parameterized using Green's functions calculations for the minimal unit cell. At first, $\xi(E)$ is evaluated on a dense grid of 99×99 k-points in the $\{k_y, k_z\}$ plane for each supercell. The interfacial coupling factor is then evaluated in the range $[-0.5, 0.5]$ eV. The resulting transmissions are presented in Fig.4.12(b) while the parameters are listed in Tab.4.3. A good agreement is reported at low energy between the semi-empirical model and the Green's functions technique, indicating the soundness of the suggested assumptions.

The role of interfacial coupling

Interestingly, two distinct regimes are observed regarding coupling effects in the equilibrium configuration. The value of γ_0 is low in the case of Ag and Cu while it is significantly higher for the other metals. It has been mentioned previously that the symmetry of the molecular orbitals involved greatly determines the effectiveness of T_{mg}.

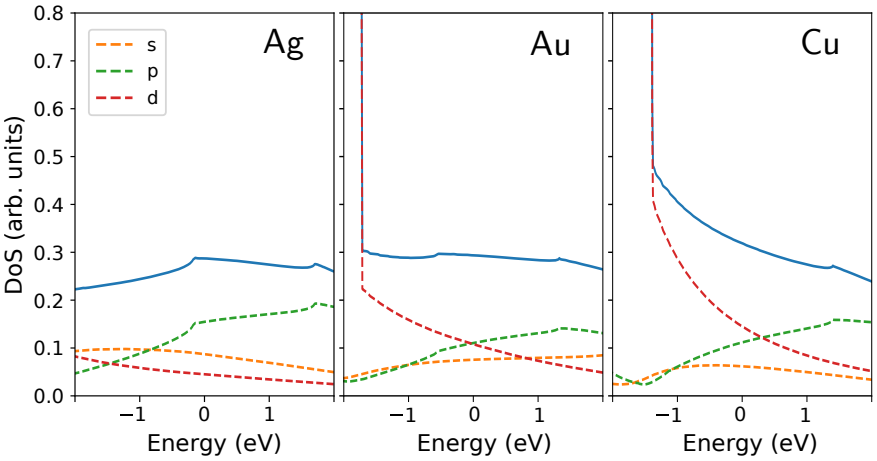

Figure 4.14: DoS of Ag, Au and Cu. The total DoS (solid lines) is compared to the projected DoS (dashed lines) on different orbitals (s, p, d).

As graphene π orbitals belong to the D_{2h} point group, they can be classified into two groups depending on their symmetry with respect to the $\{y, z\}$ plane (denoted σ_x). Similarly, the incoming wave function might be symmetric (or antisymmetric) to σ_x. In terms of electronic transport, a correspondence in symmetry between the incoming wave function and graphene p_z orbitals induces efficient electronic transmissions. On the contrary, a symmetry mismatch generates a localization of the wave function and is thus detrimental to electronic transport. Liu *et al.* [143] showed that $T(E)$ is small for Cu-graphene at low energy due to a substantial destructive overlap between graphene and the predominant s-orbitals of Cu. This assertion is in agreement with the low γ_0 reported for Cu. One must however carefully consider this statement in light of the parameters listed in Tab.4.3. Indeed, a great variation of γ_0 is observed between Au and Cu (or Ag), although those metals exhibit similar band structures (see Fig.4.3). Importantly, Liu *et al.* [143] disregarded in their analysis the influence of orbitals with greater angular momentum. However, these orbitals are essential in the characterization of the electronic structure, as represented by the partial DoS in Fig.4.14. It can be seen that the s, p and d-orbitals have an almost equivalent contribution to the DoS in the low-energy regime. Finally, it should be noted that the incoming wave function is considerably more complicated than the isolated atomic orbitals, underlining the complexity to accurately predict the effect of orbital overlap on T_{mg} based solely on the electron configuration.

In this transport analysis, the role of the interfacial gap has yet to be considered, since it greatly affects the transport properties of metal-graphene junctions. The dependency of $\gamma(d)$ on the metal-TLG separation is by nature quite complex as it affects a multiplicity of parameters which are essential in determining $\gamma(d)$, such as doping or charge localization. In their first-principles study on the modulation of R_c, Ma *et al.* [193] showed that the formation of chemical bonds between graphene and Au results in a large enhancement of the conductance. In the case of Al contacts, Stokbro *et al.* [145] computed $T(E)$ for varying separations using an extended Hückel model [198]. An exponential increase is observed for $d > 2.5$ Å whereas a saturation regime occurs in the case of covalently bonded graphene. This result supports the functional form proposed for $\gamma(d)$ but also qualitatively defines the range where the variation in separation must be accounted for. Interestingly, the lower limit for the interfacial gap corresponds to the one used in the phenomenological description of ΔE_F.

In the following section, the dependence of $T(E)$ on the interfacial gap is analyzed using first-principles calculations. By varying the adsorption height, the effectiveness of the orbital overlap between the metal and TLG is changed while keeping the electronic structure coefficient constant. At first, a simple analytical expression is proposed for κ to characterize the different transport regimes for each metal. Afterwards, κ is computed as a function of the separation using first-principles calculations. A comparison with state-of-the-art semi-empirical models of quantum tunneling is presented, enabling an unambiguous interpretation of κ.

In our model of quantum transport, κ is defined as the logarithmic rate of change of the tunneling probabilities

$$\kappa = \frac{\partial \log(T)}{\partial d} \tag{4.20}$$

where ∂d expresses a variation in the metal-graphene interfacial distance. This definition results from the phenomenological expression of the transmissions, as demonstrated in App.B. As $T(E)$ shifts from a saturation regime to an exponential increase, κ is expected to vary for intermediary separations. It reaches an asymptotic value (κ_0) at large d that is characteristic of the tunneling of charge carriers in vacuum, such as in the operation of tunneling microscopy techniques. As graphene gets closer to the surface, κ decreases at a rate (κ_1) which depends on the nature of the metal-graphene interaction. Once a certain threshold

is reached, the logarithmic rate of change is zero as $T(E)$ saturates. Consequently, the separation dependency of $\kappa(d)$ is included using the functional form

$$\kappa(d) = \max \begin{cases} \kappa_0 - \kappa_1 (d - R_0)^2 F_c(d) \\ 0 \end{cases} \tag{4.21}$$

where κ_0 and κ_1 are optimized for each type of metal-TLG junction. A smooth cutoff function has been introduced as expressed herewith

$$F_c(d) = 1 / \left\{ 1 + \exp\left[(d - R_0) / l \right] \right\} \tag{4.22}$$

in order to separate the transition region from the exponential regime. The parameters were defined in the calculations to be $R_0 = 4.4$ Å and $l = 0.1$ Å, meaning that the changeover occurs over a short interval.

The results computed from first-principles are displayed in Fig.4.15(a) for intermediary separations. A comparison with the functional form is also provided, illustrating two distinct behaviors. On the one hand, $\kappa(d)$ decreases sharply for Pd and Al so that the saturation regime is reached roughly at 3 A. This limit corresponds approximately to the one obtained by Stokbro *et al.* [145] using the Hückel model. On the other hand, $\kappa(d)$ remains almost constant for the other metals. In the case of Au, the large exponential increase agrees with the first-principles computations performed by Ma *et al.* [193]. Note that qualitatively similar values of κ_0 are reported for wide interfacial gaps, independently of the metal. That is to say that TLG acts as a universal tunneling barrier at large separations for low-energy charge carriers. On the contrary, $\kappa(d)$ appears to depend greatly on the metal electron configuration at small separations, as suggested by the similitude between Ag, Au and Cu. A large scattering in the data is due to an heterogeneous response, where certain energy regions show greater sensitivity to ∂d.

Applicability of semi-empirical approaches

After characterizing the complex dependency of $\gamma(d)$ using only two parameters, $\kappa(d)$ is interpreted through the lens of two semi-empirical models used in the prediction of the transport properties of metal-graphene junction. In the first instance, the potential term in the Schrödinger equation is assumed to vary slowly along the transport direction, giving an appropriate form for the wave function in the dipole layer. Time-dependent perturbation theory is then applied adiabatically to a time-independent Hamiltonian in the second case, providing

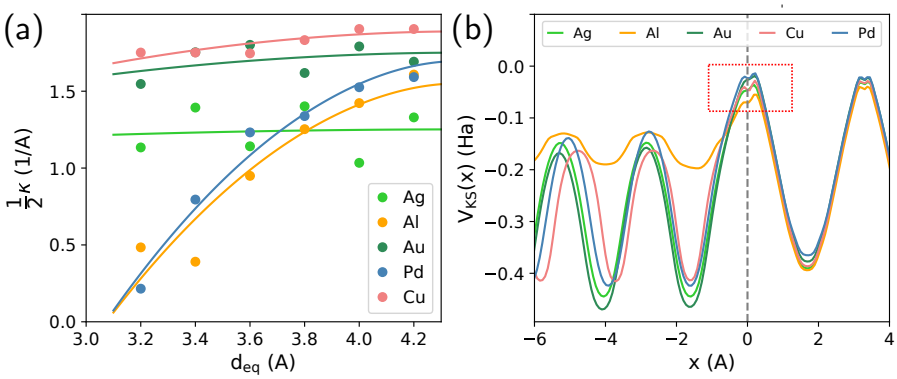

Figure 4.15: Electronic transport through a potential barrier at the metal-graphene interface. **(a)** The bonding decay length ($\kappa(d)$) as a function of the metal-graphene separation (d_{eq}) obtained from *ab initio* calculations (dots). The functional form (Eq.4.21) is drawn in comparison (solid lines). **(b)** The Kohn-Sham effective potential ($V_{KS}(x)$) excluding the non-local potential along the transport direction (x) (in solid lines), with a schematic focus on the potential at the junction generated by the dipole layer (red dotted line). The Fermi level is set to zero and the equilibrium distance is 3.3 Å. The metal substrate and graphene are located left and right of the black dashed line ($x = 0$), respectively.

an accurate description of the tunneling elements. Those methods correspond to the Wentzel-Kramers-Brillouin (WKB) approximation and the Bardeen transfer Hamiltonian (BTH) approach [199], respectively. The contact resistance is related to the interfacial gap within both formalisms as [169]

$$R_c \sim e^{\left(2\tilde{\tau}d_{eq}\right)} \tag{4.23}$$

where $\tilde{\tau}$ is the decay length. Note that the dependency on $\tilde{\tau}$ is somewhat more complex in the complete expression, although the exponential contribution remains predominant. The interested reader is invited to read Ref.[169] for a detailed analysis of the modeling of R_c within the BTH formalism.

In a general sense, $\tilde{\tau}$ describes the state of an electron decaying inside the potential barrier which, can be expressed as (see demonstration in App.B)

$$\tilde{\tau} = \sqrt{2mW_m/\hbar^2 + k_{\parallel}^2} \tag{4.24}$$

where $k_{\parallel}$ is the incident wave momentum parallel to the transport axis. In the case of metal-graphene junction, $\tilde{\tau}$ is the decay constant in the

interface dipole layer. In regards with the interface electrostatics (see Fig.4.5), W_m represents the barrier height to overcome when charge carriers tunnel from the metal into vacuum. If the graphene system functions as a filtering barrier, the predominant contribution to $k_{\parallel}$ originates from the K and K' points (i.e. $4\pi/3a_0$). This yields $\tilde{\tau} \approx 2$ A^{-1} for a typical metal work function of 5 eV. It is essential to point out that the formation of coupled electronic states are not taken into account in this estimation. This assumption is correct if the separation is large enough, typically at a distance larger than 4 A, as indicated by the computed cutoff distance (R_0). It is noteworthy that the estimation of $\tilde{\tau}$ is in qualitative agreement with the decay length obtained in STM current measurements as a function of the tip-sample distance [200], confirming the aforementioned similarity with the system under consideration.

In the configuration depicted in Fig.4.1(b), vertical injection takes place in a cascaded process. Charge carriers are transmitted first from the left electrode to TLG and then collected in the right electrode. If resonance effects inside the graphene system are neglected, the total transmission is then the product of the two tunneling probabilities [186]. This implies that $\tilde{\tau}$ is related to $\kappa(d)$ in a straightforward manner, i.e. $\kappa = 2\tilde{\tau}$. It is useful to verify this equivalence in the asymptotic limit, where the role of coupled electronic states is marginal. A satisfactory agreement is observed in Tab.4.3 with $\kappa_0 \approx 4$ A^{-1}. The slightly smaller values compared to the asymptotic limit might be explained by two factors. If reflections inside the graphene system are included (i.e. resonance effects), the drop in $T(E)$ results in a lower measurement of $\kappa(d)$. It was also assumed that $k_{\parallel} = 4\pi/3a_0$, which represents an upper bound for the momentum due to its localization at the edge of the BZ. The contribution to transport of charge carriers with lower momentum would cause $\kappa(d)$ to decrease as well. As a last comment, it is interesting to point out that $\kappa_0 \approx 2\tau$, where τ is the decay length of the wave function overlap (Δ_c), suggesting the soundness of both parameters. At smaller separations, $\kappa(d)$ also includes bonding effects that generate non-linearity in the decay rate. In such situation, tunneling is characterized by a smaller decay constant than vacuum, as demonstrated experimentally [201].

Lastly, it is interesting to examine the applicability of the semi-empirical methods presented above in light of our first-principles calculations. The WKB approximation is verified if the potential barrier change over a wavelength is much less than the charge carrier kin-

etic energy [202]. For the current set of parameters, this statement is explicitly expressed as

$$\frac{dV}{dx} \ll 0.2 \text{ Ha/A} \tag{4.25}$$

where V is the potential generated by the dipole layer. In the current configuration, dV/dx is much smaller than the required criterion, as illustrated in Fig.4.15(b) where the Kohn-Sham effective potential (V_{KS}) is depicted. It should be noted that V_{KS} is defined as a sum over the potentials generated by the neutral atoms, the difference in electron density (δV_H) and the exchange-correlation, where non-local contributions are excluded [106]. The central prediction of the WKB approximation is that the wave function decays exponentially inside the barrier. The BTH approach then predicts electronic transmissions to exhibit a similar dependency on the interfacial gap if the metal and graphene wave functions vanish inside the barrier [199]. This condition still holds when the inequality $\tilde{\tau}d \gg 1$ is sufficiently verified. From the previous discussion on the decay constants, one has the following criterion

$$\frac{1}{2}\kappa d \gg 1 \tag{4.26}$$

It is clear that this condition is met for every metal in their equilibrium configuration with the exception of Pd. Similarly, it can be assumed that Eq.4.23 is not applicable when graphene is chemisorbed. Transmissions are less sensitive to perturbations (e.g. variation in the bonding length), as the metal-graphene interaction increases in strength. That is to say that $\kappa \approx 0$ in the chemisorption regime. Hence, the BTH approach is not relevant anymore, especially since the equilibrium distance is short and interfacial electronic states must be accounted for. This semi-empirical method is thus applicable for physisorbed graphene, although the wave function overlap generates discrepancies in the final transmissions, as measured by the coefficient γ_0. Lastly, it should be noted that the analytical model (Eq.4.16) has been parameterized with first-principles computations, whose only approximation resides in the choice of the exchange-correlation functional in the single-particle picture. If $\gamma(d)$ is assumed independent of structural parameters such as the surface orientation, the previous results can be assumed to be quite universal.

In the last section of this analysis on the transport properties of metal-graphene junction, the transport model is extended to the Moiré supercells listed in Tab.4.2. When the epitaxial and structural relationships between the substrate and graphene are changed, the electronic structure coefficient and the orbital overlap are modified in consequence. It is not possible to accurately characterize the latter dependence due to the size of the systems under consideration, for which Green's function calculations are not suitable. That is why the coupling parameter is assumed to be a function of the separation and the substrate and not related to the crystallographic orientation. This assumption is motivated by the observation in Fig.4.8(b) that $\Delta_c(d)$ is roughly comparable for the (100) and (111) surfaces, suggesting that orbital overlap parameters depend marginally on the crystallographic facet. In this framework, the impact of the substrate orientation on $T(E)$ can be described by the transport model. That is to say that $\gamma(d)$ is adjusted using the functional form proposed for $\kappa(d)$ while $\xi(E)$ is computed from the supercells electronic structure at a doping given by the phenomenological model (Eq.4.9).

The tunneling probabilities obtained using the empirical transport models for the supercells are depicted in Fig.4.16. Next to the transmissions, an overview of the two contributions is provided. The effect due to the correspondance in momentum space is described by

$$\delta\xi = \int_{\Omega_E} \xi(E)dE \Big/ \int_{\Omega_E} \xi^{ref}(E)dE \tag{4.27}$$

where $\xi^{ref}(E)$ corresponds to the minimal unit cell and $\Omega_E = [\Delta E_F - \delta E, \Delta E_F + \delta E]$ with $\delta E = 0.5$ eV. This energy window is consistent with our estimation of γ_0 in Sec.4.5. In the case of Cu$(1\bar{1}1)$ and Cu(100), the reduced dimension of the optimized basis set enables the computation of the transmissions using the Green's functions formalism. This will be useful later on to assess the accuracy of the model and the soundness of its assumptions.

Two situations are to be distinguished in Fig.4.16. For the (111) supercells, the discrepancy with respect to the minimal unit cells resides almost entirely in the epitaxial relationship with graphene. At other crystallographic orientations, d_{eq} is subject to substantial variations that greatly impact doping and $\gamma(d)$. A preliminary and general observation

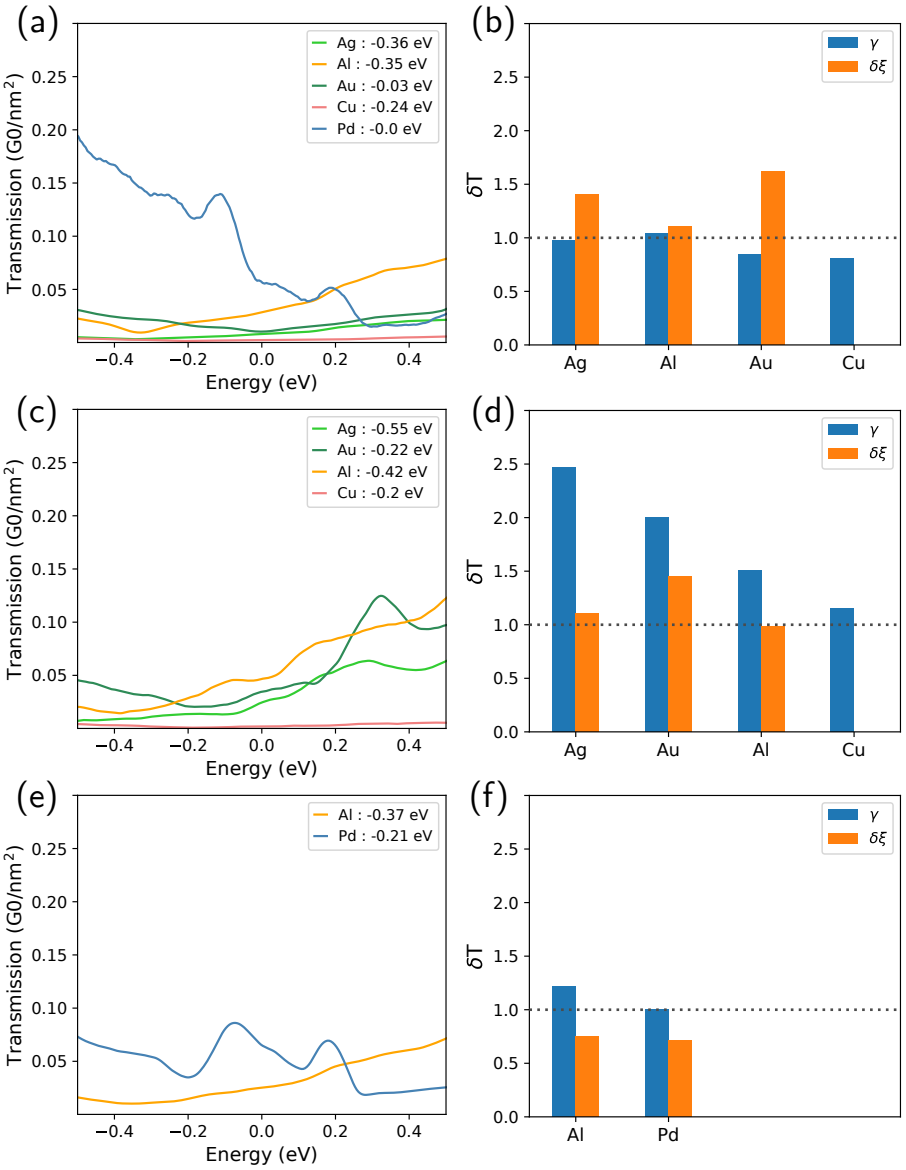

Figure 4.16: Electronic transport properties of metal-TLG nano-junction computed within the transport model for different crystallographic orientations. Electronic transmissions per unit area as a function of energy for the **(a)** (111), **(b)** (100) and **(c)** $(1\bar{1}1)$ surfaces. The related dopings of TLG are listed correspondingly. The increase in transmissions (δT) due to the crystal momentum mismatch ($\delta\xi$) and to the coupling between orbitals (γ) for the **(b)** (111), **(d)** (100) and **(f)** $(1\bar{1}1)$ surfaces.

is that $T(\Delta E_F)$ does not correspond to the minimum of conductance in the case of Pd(111) and Pd$(1\bar{1}1)$. This phenomenon is due to the non-zero overlap at the Fermi level between the parabolic bands [163]. One could use f^{Gr} from monolayer graphene to circumvent this apparent inadequacy with experimental measurements. The electronic structure of TLG is nonetheless retained for the sake of consistency, especially since graphene and TLG are close enough regarding their electronic properties in the low-energy regime. In Fig.4.16(a), $T(E)$ are found to be in good agreement with the results obtained for the minimal unit cell. The major source of modification comes from $\xi(E)$, as previously expected. The largest impact is an increase of 50% in the case of Au, in line with earlier studies on zigzag and armchair graphene ribbons [141, 142]. Cu(111) stands as an exception as transmissions are increased up to tenfold after graphene is rotated by 19.1°. The negligible $\xi(E)$ for the 1×1 unit cell also implies that the use of $\delta\xi$ is not relevant for Cu. In the supercell configuration, the crystal momentum match/mismatch is such that TLG acts as a filtering barrier rather than a transparent one. As it concerns the (100) surfaces, the dominant source of variation lies in a change of $\gamma(d)$ (see Fig.4.12(d)). Lastly, the noticeable decrease in $T(E)$ is related to a lower $\xi(E)$ in the case of the $(1\bar{1}1)$ crystallographic facet. For both surfaces, the shift of the Fermi level is found to play an important role by shifting proportionally the overall transmission curve.

In order to assess the credibility of these assertions, the transport model is compared to Green's function calculations in Fig.4.17. Chemisorption and physisorption are represented in the case of Cu$(1\bar{1}1)$ and Cu(100), respectively. The model is reported to reproduce accurately the transport features of the weaker adsorption regime while it yields an acceptable agreement with the stronger one, although its underlying assumptions are not expected to hold true at such a low interfacial distance. The acceptable agreement can be understood by noting that Cu$(1\bar{1}1)$ is only weakly chemisorbed at $d_{eq} = 2.85$ Å.

4.7 CONCLUSION

In summary, first-principles calculations were employed to study the electronic and transport properties of vertically stacked metal-TLG junctions.

First, a phenomenological model based on the work function was proposed to describe doping of graphene due to charge transfer oc-

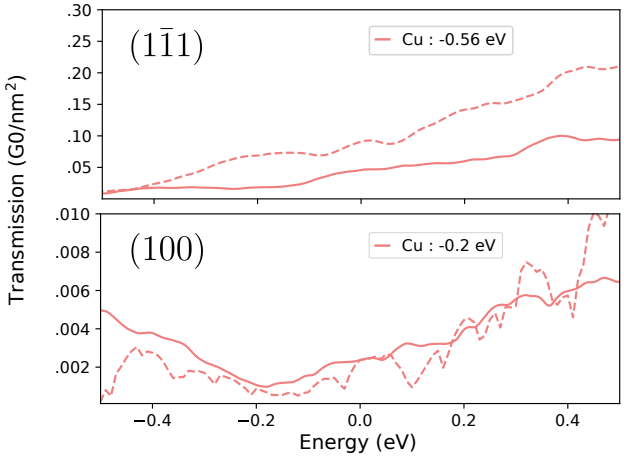

Figure 4.17: Electronic transmissions per unit area as a function of energy calculated within the transport model (solid lines) and the Green's functions approach (dashed lines) for Cu, for the $(1\bar{1}1)$ and (100) surfaces. The related doping of TLG is listed correspondingly

curring at the interface. This approach was initially applied to the minimal unit cell and then extended to larger Moiré patterns and other substrate orientations. The metal-TLG system was also demonstrated to be transferable to the analysis of R_c in single-layer graphene due the similar electrostatic characteristics.

The vertical injection of charge carriers was investigated using Green's functions techniques while the transport mechanisms were explored through the lens of a semi-empirical transport model. The orbital overlap between the metal and graphene was found to depend in a complex manner on the metal electron configuration. A comparison with state-of-the-art semi-empirical approaches was drawn using the parameters extracted from this model. The WKB approximation and the BTH method were demonstrated to be applicable to metal-graphene junctions in the case of physisorption whereas they are ill-designed for the chemisorption regime.

Lastly, physisorbed graphene was shown to act as a filtering barrier in the absence of an epitaxial relationship with the contacts. In light of this observation, the GB-HET developed by Zhu *et al.* [148] is considered once more. The device is composed of stacked doped silicon, graphene and a top Cr/Au electrode. It was mentioned that the graphene π orbitals may have been strongly perturbed due to chemical interactions with the fresh metal surface. It has been experimentally proven that coherent

metal-graphene interfaces are energetically favorable on Co(0001) and Ni(111) [179] while silicon and graphene are known to form incoherent interfaces [203]. It can therefore be stated with confidence that the device transparency does not result so much from a crystal momentum mismatch but most presumably from interfacial hybridization at the metal junction, causing electron to tunnel through the gap between H-passivated silicon and chemisorbed graphene.

To conclude on the contact resistance, two fundamental messages are derived from our detailed analysis.

The first observation is that R_c may substantially vary for a given metal, depending on the surface characteristics such as the crystallographic orientation. The presence of defects, the roughness of the substrate or its chemical reactivity are various factors that are also expected to play an important role on R_c by influencing, among others, the bond length with the over-layered graphene. Such perturbation induces a change of the coupling constant which results for physisorption in a substantial change in transmission probabilities [193]. This effect is predicted to affect T_{mg} by at most one order of magnitude, providing a rough estimation for the aforementioned substrate-related effects when disorder is moderate. In such situations, larger discrepancies in experimental measurements should be explained by other influencing factors such as self-doping or the fabrication process. Note that a more precise estimation could be obtained by accurately investigating the spatial variation of d_{eq} in Moiré structures, such that an average influencing factor $\bar{\gamma}$ could be derived. Additionally, the transport model indicates that Ag, Au and Cu are more sensitive to external perturbations than Pd, in agreement with experimental observations [58, 167]. As concerns theoretical predictions, the noticeable disparity in the computed conductances [58] stems from structural variations caused either by the choice of exchange-correlation functional or by the computational framework.

The second comment concerns the prediction of low R_c. The first condition to employ contacts with large DoS while increasing the DoS in graphene. Except for coherent metal-graphene interfaces, $\xi(E)$ is expected to depend solely on each material DoS for realistic interfaces due to band folding. Transport calculations then exhibit an linear relationship between the number of conducting modes in the graphene channel and T_{mg}, stemming from the linear DoS of graphene. This observation is in agreement with previous theoretical and experimental works [58]. A second condition lies in an efficient interfacial coupling.

The orbital overlap must be efficient for transport (γ_0 is large) while also substantially increasing T_{mg} when the metal-graphene separation decreases due to external factors. This means that $\kappa(d)$ does not saturate at small distances.

From our analysis, Au stands out as the best candidate to meet those requirements. It shows the largest γ_0 while $\kappa(d)$ does not saturate until short metal-graphene separation. The low doping upon contact means that it is easily tunable by a gate voltage. In addition, its low reactivity reduces the impact of external factors such as chemical contamination of the vdW gap. Correspondingly, Pd appears as an interesting candidate. It has a large γ_0 and a higher DoS than other metals due to the contribution of d-orbitals at low energy. However, its early saturation regime and its tendency to form carbide when interacting with graphene degrade its prospects for device integration. Indeed, the scope of this analysis is to provide avenues to design efficient contacts while impacting as little as possible the electronic properties of the over-layered graphene. Although chemical bonding reduces R_c, the electronic properties of chemisorbed graphene are strongly modified on a typical length scale of tens of nanometers. In the context of device miniaturization, the extent of this perturbation is far too large. When more invasive contacts are employed, proper engineering of the dielectric environment is required to ensure a negligible impact of the contacts on free-standing graphene [188].

5 POLYCRYSTALLINE GRAPHENE

Since its isolation by mechanical exfoliation from graphitic material [18], graphene has triggered enormous enthusiasm in the scientific community due to its unusual properties. The confinement of electrons in 2D leads to the emergence of massless chiral fermions with linear energy dispersion near the BZ corners. As detailed previously, this singular nature of low-energy charge carriers is responsible for many exotic phenomena [25].

Although most of this novel 2D physics was first revealed on exfoliated monolayer, graphene is currently synthesized by CVD techniques, presently by far the most viable and industry-compatible production methods [204]. Large-area wafer-scale monolayers can be transferred to desired substrates, patterned and modified locally, therefore enabling different electronic functionalities for all graphene-based circuits [205].

CVD graphene is found to be polycrystalline in nature, hence composed of many single-crystal domains separated by GBs of irregular shapes. Grains nucleate on a substrate at different crystal-oriented sites and grow until line defects are formed at their intersection. Grain sizes range from a few hundred nanometers to several centimeters in diameter, with a roughness that mimics that of the substrate [206]. The line defects at the grains interface are mainly composed of topological defects that accommodate for the lattice mismatch between each domain. More specifically, GBs appear as extended structural defects consisting of a random 1D distribution of non-hexagonal rings, mostly constituted of pentagon-heptagon pairs [50, 207].

Scanning probe microscopy studies demonstrated that such line defects introduce major perturbation in the electronic structure of graphene [208, 209]. These measurements revealed that GBs tend to be n-doped compared to the surrounding grains, thus acting as an electrical potential barrier for charge carriers [210, 211]. Kochat *et al.* [212] showed a strong correlation between the quality and the resistivity of GBs, with wide regions of disorder being more resistive than narrower ones. Similarly, Tsen *et al.* [213] established that poorly-connected GBs can significantly enhance the resistance of graphene by one order of magnitude, whereas Park *et al.* [214] concluded that the

electrical performance of well-stitched CVD graphene is not degraded by GBs. Lastly, transport measurement through GBs suggested that the resistance is temperature-independent [213, 215–217], supporting the hypothesis that scattering at GBs is dominated by structural defects and impurities. In a nutshell, those imperfections strongly affect the overall properties of wafer-scale graphene [218]. In particular, GBs are known to be an important source of scattering that limit drastically the carrier mobility of PG, with a degrading effect that is related to the average grain sizes and quality of the GBs [219].

Those results indicate that the high-performance need in graphene-based devices would require the controllable synthesis and large scale fabrication of single-crystalline graphene [215]. Nonetheless, large mobilities obtained in PG tell another story. Banszerus *et al.* [220] used advanced transfer techniques to measure electron mobilites as large as $350,000\ \mathrm{cm^2V^{-1}s^{-1}}$ for CVD-grown graphene, rivaling those obtained in suspended [32] and encapsulated [33] graphene. These results suggest that CVD could yield samples comparable in quality to large-area single-crystals obtained by exfoliation, which contain intragranular line defects and other structural imperfections [221]. Additionally, the controlled manufacturing of structurally well-defined line defects support the feasibility of designing novel graphene-based devices at the nano-scale using CVD [208].

In this context, the role played by GBs on the transport properties of PG is still a debated issue. So far, only a few theoretical studies based on first-principles approach have tried to scrutinize electronic transport through GBs, but only for ideal or extremely specific geometries. Indeed, line of defects with rather short periodicities have been investigated [222]. It was demonstrated that their detrimental effect can be removed through atomically precise manufacturing and that a transport gap can be opened in PG. This latter result is of primary importance for switching off potential graphene-based nano-devices. These ideally aligned defects with short periodicities are however not representative of real GBs which exhibit a more complicated atomic structure, neither straight nor periodic, but rather meandering aperiodic lines composed of fundamental units of pentagon-heptagon pairs with a significant amount of local disorder [223]. Consequently, the prediction of the transport properties in PG modeled with ideal GBs could substantially deviate from experimental measurements.

In the present chapter, first-principles simulations based on DFT are used to explore charge transport through a few "realistic" GBs.

For computational efficiency reasons, the exchange-correlation energy is described with LDA while carbon atoms are modeled using two *s*-orbitals and one *p*-orbital. This basis set is denoted as *s2p1*. A fine *k*-points grid of $48 \times 48 \times 1$ for the graphene unit cell was employed using the Monkhorst-Pack scheme [105]. To avoid spurious image interaction, a distance of 20 Å is defined between the layers. Each graphene-based system was relaxed using classical molecular dynamics to minimize its configurational energy using optimized Tersoff potentials [224]. This empirical potential was demonstrated to accurately describe the structural, thermal and mechanical properties of PG [225]. Lastly, the scattering region enclosed by two semi-infinite leads spreads from 5 to 10 nm, such that most of the in-plane strain due to atomic dislocations in the GB vicinity is included.

We start our investigation by comprehensively presenting in Sec.5.1 the structural concepts for the description of GBs as well as the transport regimes occurring in PG. In order to simulate as close as possible real GBs, more complicated atomistic models are constructed using different types of geometries, with rather large periodicity and relatively complex non-hexagonal ring configurations. The transport properties of those extended line of defects are studied in Sec.5.2. In particular, the periodicity of GBs is analyzed through a perturbative approach by introducing additional small amount of disorder in a repeated pattern. Lastly, the inter-connectivity between grains is diligently examined in Sec.5.3 by considering diverse arrangements of non-hexagonal rings through a steady increase of disorder. The results of this chapter are detailed in the conclusion. Charge redistribution effects related to the detailed GB topology are found to substantially alter the transmissions at specific energies. Altogether, the opening of a transport gap is shown to be resilient to disorder, although imperfections are found to induce leakage currents. The ambition is that this *ab initio* modeling of GBs will pave the way towards a more accurate understanding of electronic transport in PG, such that the degrading effects of GBs can be greatly removed.

5.1 QUANTUM TRANSPORT THROUGH GBS

In order to characterize structurally a GB as a periodic line of defects, some essential geometrical concepts should be specified (see Fig.5.1). A translational vector $\vec{d}$ is used to relate the relative displacement between the lattices of the two graphene domains [226], with a periodicity of

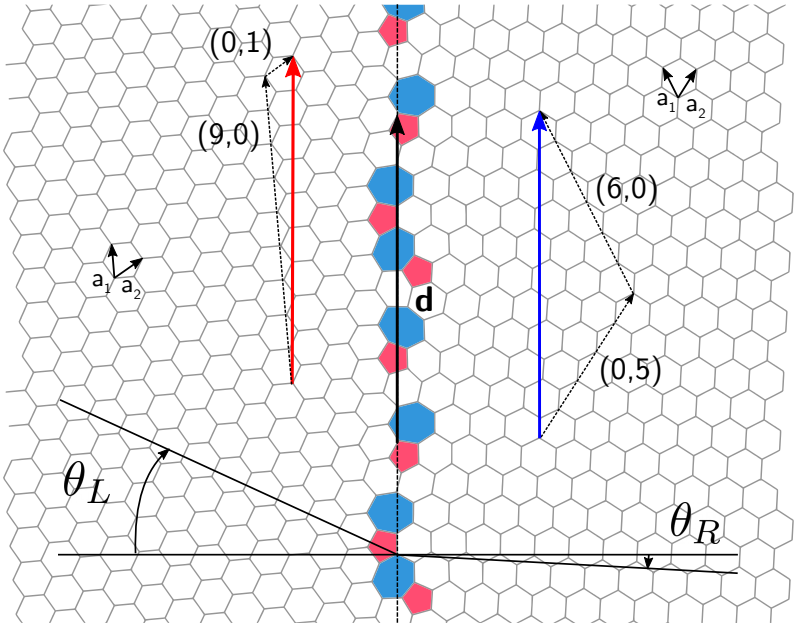

Figure 5.1: Atomic structure of a GB in PG. An example of a GB containing four pentagon-heptagon pairs per unit cell and separating two graphene domains rotated compared to each other by $\theta = \theta_R + \theta_L = 21.8°$, where θ_L and θ_R represent the orientation of each domain with respect to the zigzag crystallographic direction. The same convention for misorientation angles was introduced in Ref.[227]. The translational vector $\vec{d}$ of the GB structure is defined in terms of the lattice vectors $(\vec{a}_1, \vec{a}_2)$ by the matching vectors $(9,1)$ and $(6,5)$ in the left and right domains, respectively.

$1-5$ nm corresponding to periodically repeated atomic structures as experimentally observed in GBs [222]. In 2D systems, $\vec{d}$ is expressed as (n_L, m_L) and (n_R, m_R) in the left and right graphene domains, respectively. The indexes (n_i, m_i) describe the translational vector in terms of the lattice vectors $(\vec{a}_1, \vec{a}_2)$ in each crystalline region. In the left and right graphene domains, this vector is oriented by a respective angle θ_L and θ_R compared to a corresponding crystallographic direction (either armchair or zigzag). A total misorientation angle θ is defined with respect to the normal of the boundary line as $\theta = \theta_R + \theta_L$, based on the convention developed in Ref.[227]. In the following, two examples of GBs are reviewed in order to demonstrate the convenience of using the geometrical concepts illustrated in Fig.5.1.

The simplest case of a GB acting as a mirror symmetry line between two graphene domains is considered first. Symmetric GBs exhibit a

well-defined periodicity, expressed in terms of the lattice parameter of graphene as $d = |(n_i, m_i)| = a_0\sqrt{(n_i^2 + n_i m_i + m_i^2)}$. This simple GB model is illustrated in Fig.5.2(a) with a periodic alignment of pentagon-heptagon pairs. Pentagons lead to positive (spherical) curvature and heptagons to negative (saddle-like) curvature, such that a pentagon-heptagon pair lies inside the graphene plane. More generally, polygon curvatures must cancel each other as it results in a global warping with a logarithmically diverging energy [228]. Configurations of positive and negative structural defects are thus needed to cancel curvature. These structural defects conserve the three-fold coordination of each carbon atom and yield a low-energy cost for the GB. In the present case, the dense sampling of pentagon-heptagon pairs corresponds to a large misorientation angle $\theta = 21.8^\circ$ and a short periodicity $d = 6.52$ Å. Note that a small θ results in widely separated pentagon–heptagon pairs while a large θ induces the pairs to be close to each other. Simonis *et al.* [229] proposed this structural motif in the context of scanning tunneling microscopy studies of GBs in graphite. Its formation energy was estimated to be around 3.4 eV/nm [227], which is much smaller than typical formation energies of bare graphene edges (about 10 eV/nm or more) [230].

A more general case involves an asymmetric GB with a periodicity that depends on specific commensurable conditions between the two graphene domains. The resulting period is typically much longer and usually induces a higher energy cost per unit length [231]. In order to reduce this energy cost, out-of-plane buckling might occur along the line defects to accommodate for the generated strain. The related buckling amplitude decreases with increasing misorientation angle and is typically around 1 Å along the out-of-plane direction [227]. Only planar topological defects are however considered hereafter, thus initially neglecting out-of-plane buckling. An example is depicted in Fig.5.2(b), where the commensurable condition is ensured by applying a relative strain between the two graphene grains. The misorientation angle is $\theta = 30.0^\circ$ and the periodicity is set to $d = 12.6$ Å in order to distribute the stress equally between the left and right graphene domains, which are respectively oriented along the GB in the zigzag and armchair directions. Although the commensurable condition involves a relative lattice mismatch $\Delta d/d = 3.85\%$, the corresponding atomic structure formation energy of 5.0 eV/nm is still considerably small, indicating the relative stability of the asymmetric GB.

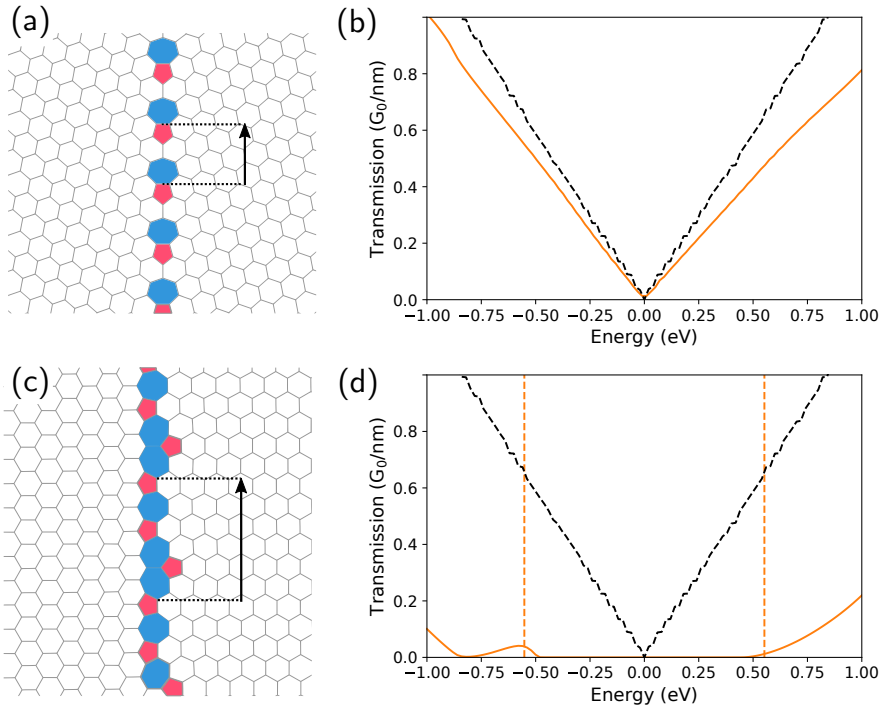

Figure 5.2: First-principles electronic transport through ideal GBs in PG. Atomic structures of **(a)** the $(2,1)|(2,1)(\theta = 21.8°)$ class-I GB and **(c)** the $(5,0)|(3,3)(\theta = 30.0°)$ class-II GB with respective **(b,d)** zero-bias total conductance per unit length. Conductances through the GB as a function of energy (solid line) are compared to pristine graphene (dashed line). The theoretical transport gap is indicated by vertical dashed lines.

Yazyev *et al.* [222] characterized electronic transport through GBs using this structural description, where charge carriers crossing an interface experience an effective rotation of the BZ. The electronic properties are derived solely for low-energy charge carriers, which are characterized by a linear energy dispersion around the Fermi energy. The dispersion relation is thus written $E(k) = \hbar v_F k$, where the Fermi velocity v_F and the momentum k are defined with respect to the Dirac points K and K'. Crystal momentum conservation is assumed along the boundary line, which is considered to be infinitely long periodic array of defects. Two cases are derived, depending on the expression of the translational vectors $\vec{d}$ in terms of the matching vectors (n_L, m_L) and (n_R, m_R). If $\vec{d}$ is expressed as $n - m = 3q$ with $q \in \mathbb{Z}$ for both domains (or equivalently as $n - m \neq 3q$), then for any charge carrier with a given momentum and energy in one domain, there exists a

corresponding channel with same momentum and energy in the other domain. However, if one translational vector belongs to $n - m = 3q$ whereas the other is defined as $n - m \neq 3q$, then transmission is only feasible for certain allowed momentum-energy pair and a transport gap is opened. Subsequently, GBs are classified in two categories, either transparent or reflective, labeled as class-I and class-II, respectively. The latter case is characterized by a transport gap defined as

$$E_g^* = \hbar v_F \frac{2\pi}{3d} \approx \frac{1.38}{d(\text{nm})}\text{eV} \tag{5.1}$$

which depends exclusively on the boundary periodicity length. This prediction suggests that GBs can be sorted on their transport properties with information based only on their misorientation angle and periodicity. An important conclusion is that commensurable systems are class-I GBs whereas class-II GBs are incommensurable systems, thus characterized by a lattice mismatch [222]. In the case of asymmetric GBs, strain was later found to open a transport gap in class-I GBs while it increases the magnitude of the gap in class-II GBs [232]. Nguyen *et al.* [233] further showed that strain effects are in fact more complex, with a dependence on its applied direction and the lattice symmetry of the two graphene domains surrounding the boundary.

Our calculations are performed with a reduced basis set compared to Ref.[222], allowing for a less expensive computational cost but with the same accuracy level. Indeed, conductances presented in Fig.5.2 for the symmetric and asymmetric GBs are in very good agreement with those reported in the literature [222, 232–235]. Both interfaces are characterized by small periodicities and large misorientation angles, indicating that the corresponding systems are planar in their stable configurations. Line defects with $\theta \approx 30.0^\circ$ are predicted to remain flat in their ground-state configurations [227], in line with our *ab initio* structural optimization conducted with a force tolerance of 10^{-4} Ha/a_0.

The symmetric class-I GB is defined by a linear combination of lattice vectors such as $\vec{d} = (2, 1)$. The resulting total transmission for low-energy carriers exhibits a high transparency (see Fig.5.2(b)), despite the large concentration of pentagon-heptagon pairs. The low scattering may be related to the atomically thin width of the interface. Note that there is a non-trivial asymmetry between holes and electrons, with a slightly larger conductance for holes. This small disparity is caused by the breaking of the bipartite symmetry of the graphene lattice for low-energy charge carriers due to the presence of topological defects [222].

Regarding the class-II GB, its translational vector is expressed in terms of lattice vectors $\vec{d}_L = (5,0)$ and $\vec{d}_R = (3,3)$. This system exhibits a substantially large transport gap of $E_g = 0.92$ eV, as illustrated in Fig.5.1(d). This transport gap is in good agreement with the estimation of $E_g^* = 1.1$ eV from Eq.5.1. Note that the value of the transport gap is determined in the logarithmic plot of conductances using a tolerance criterion of 10^{-5} G_0/nm. This method might lead to a small differences with values reported in the literature but is the standard one to assess the capability of switching on and off the current in electronic devices. In order to measure the deviation between Eq.5.1 and DFT calculations, a parameter $\delta = (E_g^* - E_g)/E_g^*$ is introduced. In this case, $\delta = 16.4\%$. Outside the transport gap, considerably smaller conductances for both electrons and holes are obtained compared to pristine graphene, with non-hexagonal rings breaking the electron-hole symmetry.

Overall, the transport properties across both commensurable and incommensurable GBs are found to be reasonably well characterized using the present numerical framework, indicating that more complex configurations can be further investigated using this approach.

5.2 QUANTUM TRANSPORT THROUGH EXTENDED GBS

A more realistic GB constructed from more complicated arrangement of polygons is considered hereafter. This array of point defects is characterized by the presence of dangling bonds, with a respective density about 2 nm^{-1} (see Fig.5.3(a)). This GB is defined by a translational vector $d = 32.0$ Å, expressed as $\vec{d}_L = (11,3)$ and $\vec{d}_R = (10,5)$ in the left and right domains, respectively. The grains are tilted with respect to each other by $\theta = 30.8^\circ$. A relative lattice mismatch of $\Delta d/d = 3.55\%$ is applied to ensure commensurability. Liu *et al.* [236] estimated the formation energy of a similar GB tilted by $\theta = 30.2^\circ$ to be 4 eV/nm, indicating the relatively stability of this atomic structure. This system is predicted to be transparent, as depicted in Fig.5.3(b), although the corresponding transmissions are relatively lower compared to pristine graphene. A damaging impact is supposedly due to the quality of the boundary, which contains dangling bonds that increase undesirable scattering.

First-principles transport computations were then performed on class-II GBs. An initial pattern defined by a periodicity of 14,9 Å was considered, corresponding to $\vec{d}_L = (6,0)$ and $\vec{d}_R = (4,3)$ in the graphene domains. This asymmetric GB is characterized by a misorientation

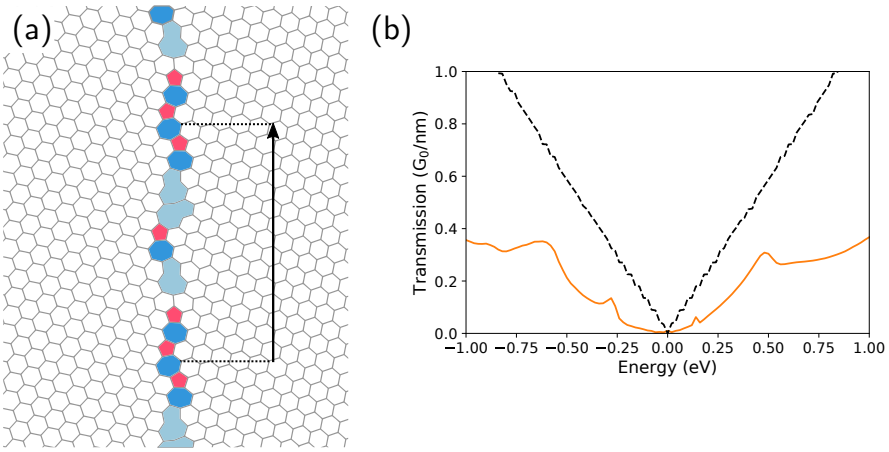

Figure 5.3: First-principles electronic transport through a realistic GB in PG. **(a)** Atomic structure of the $(11,3)|(10,5)(\theta = 30.8°)$ class-I GB where the pentagon (red) and heptagon (blue) are highlighted in green when the pair contains a dangling bond. **(b)** Zero-bias total conductance per unit length through the GB as a function of energy (solid line) compared to pristine graphene (dashed line).

angle $\theta = 25.3°$. From this simple configuration, more complicated GBs were constructed by removing an atom after repeating n times the initial pattern. Fig.5.4(a) illustrates the atomic structures for $n = 4$. The resulting configuration is thus interpreted as a periodic perturbation to the initial pattern. This perturbative analysis of disorder intends to benchmark the assumption to model GBs as periodic line of defects. Indeed, most abundant GBs observed with scanning tunneling microscope exhibit irregular structures, with no simple periodic array of dislocations [209]. A nomenclature is introduced in order to distinguish between different perturbed GBs. The initial pattern is denoted AMC-1d whereas any n-periodic system with an additional vacancy is denoted AMC-nd. Each disordered system corresponds to a vacancy concentration defined as $c = 0.673/n$ nm^{-1}.

The corresponding conductances are presented in Fig.5.4(b). The semilogarithmic plot reveals non-zero currents as large as 10^{-2} G_0/nm inside the transport gap as well as the presence of a secondary gap. A distinction is made by identifying the first as a *quasi* transport gap (QTG) and the second as a *real* transport gap (RTG). From Eq.5.1, it is evident that both gaps originate from two different periodicities. Indeed, the QTG is related to the initial pattern length $d = 14.9$ Å while the RTG is associated to the largest periodicity $d' = n\ d$. In contrast, non-zero

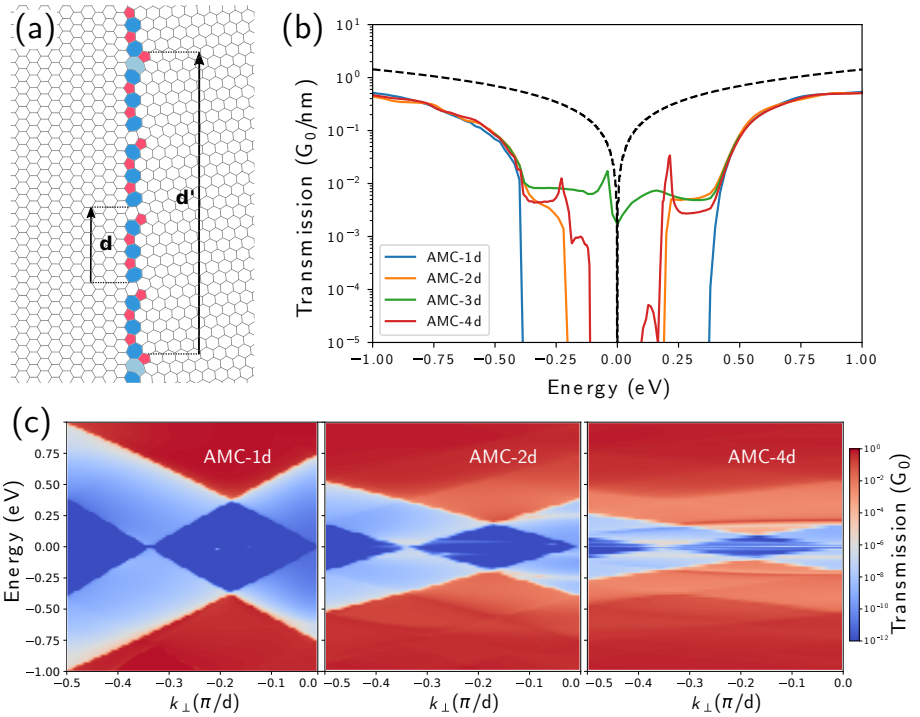

Figure 5.4: First-principles electronic transport through realistic GBs with peridiocally decreasing disorder in PG. **(a)** Atomic structure of the $(24,0)|(16,12)(\theta = 25.3°)$ class-II GB (denoted AMC-4d) where a carbon ring containing a vacancy is highlighted in azur. The initial and the repeated periodicities are respectively defined as $d = 14.9$ Å and $d' = 4\ d$. **(b)** Zero-bias total conductance per unit length through AMC-nd with $n = \{1,2,3,4\}$ as a function of energy compared to pristine graphene (black dashed line). **(c)** Transmission probabilities (in logarithmic units) as a function of transverse momentum $k_\perp$ and energy E for AMC-1d, AMC-2d and AMC-4d (from left to right).

Table 5.1: Transmission gaps of class-II GBs extracted from *ab initio* calculations (E_g) and computed from Eq.5.1 (E_g^*). The corresponding relative deviation $\delta = (E_g^* - E_g)/E_g^*$ is also provided.

	E_g [eV]	E_g^* [eV]	δ [%]
AMC-1d	0.76	0.93	18
AMC-2d	0.38	0.46	17
AMC-4d	0.20	0.23	13

transmissions are observed for AMC-3d at low energy, in agreement with the theoretical model. Inside the QTG, non-zero currents are defined as leakage currents. Their occurrence was already predicted in the case of impurities randomly distributed along a 11 nm long boundary line [222]. Those impurities had concentrations spanning from 0.1 to 1 nm^{-1}, which is equivalent to the vacancy densities of AMC-nd that ranges between 0.2 and 0.7 nm^{-1}. Outside the QTG, conductances appear to be similar and independent of the vacancy concentration, with a transparency of roughly 30% compared to pristine graphene.

The RTG is estimated for $n = \{1, 2, 4\}$ using our previous tolerance criterion of 10^{-5} G_0/nm. This means that current as small as 10^{-2} G_0/nm are defined as leakage currents if a standard on-off ratio of 10^3 is selected. The transmission gaps extracted from *ab initio* calculations are summarized in Table 5.1. A comparison with values computed from Eq.5.1 is also provided. A qualitative agreement is observed between E_g and the theoretical predictions, with a nearly constant deviation parameter not so far from the previously estimated $\delta \approx 16\%$. Importantly, the proportional trend between E_g and $1/n$ is well represented. Note that non-zero transmission are observed in the transmission gap. This feature is well perceptible in the case of AMC-2d for $k_\perp/d \in [-\pi/3, -\pi/10]$ and $E \approx 0.1$ eV (see Fig.5.4(c)). Those conductance peaks result from numerical limitations and are generated by strongly localized electronic states related to the 1D nature of GBs [193, 209, 237]. The discrepancy measured by the parameter δ likely originates from non-linearity in the band structure at higher energy. When the energy range related to the RTG decreases, δ gets smaller as non-linear effects are mitigated.

The primary mechanisms of scattering occurring at GBs are identified hereafter, in accordance with experimental observations. Microscopy imaging revealed through STM and STS techniques that GBs greatly perturb the local electronic structure by inducing charge redistribution effects that depend explicitly on structural considerations [209]. Charge carriers scattering is expected to be influenced non-trivially by numerous atomistic parameters [238]. Some predominant features can however be identified. Intrinsic topological defects are found to generate localized states at the Dirac point [208, 227, 237], resulting in resonant backscattering of low-energy charge carriers [239]. STM measurements also indicate that the resistance of GBs is changing with the width of the scattering region [212, 213, 240]. Lastly, corrugation is expected to bear important implications on the transport properties in PG [241]. Consequently, we have considered the following additional sources of disorder: (i) highly concentrated vacancies, (ii) a larger inter-connectivity region and (iii) out-of-plane buckling.

The resulting atomic configurations along with their electronic conductances are depicted in Fig.5.5.

The effects of vacancies are investigated with two GBs characterized by a vacancy density defined as $c_i^* = i\ 0.67\ \text{nm}^{-1}$ with $i = \{1, 2\}$. Introducing a vacancy in an hexagonal network creates three dangling bonds, which will eventually relax to form energetically more stable reconstructed vacancies [242]. The three-dangling-bonds configuration has nonetheless been preserved to enlarge the possible detrimental effects of vacancies on charge transport. No notable impact on transmissions is noticed for c_1^*, as the increased scattering only produces small changes in conductance. This result is consistent with our previous observation. No substantial effects was reported outside the QTG for AMC-*n*d at comparable vacancy concentrations. On the contrary, a uniform drop of roughly 50% occurs for c_2^* due to the larger concentration of vacancies.

Electronic transmissions are drastically reduced when considering a wider inter-connectivity region, from 50% up to 75% depending on the system. These predictions seem to concur with experimental measurements for poorly-connected grains [213]. This is understood by noting that transmission through GBs occurs by quantum tunneling at low temperature. A poor connectivity between grains therefore translates into a wider potential to overcome, substantially degrading

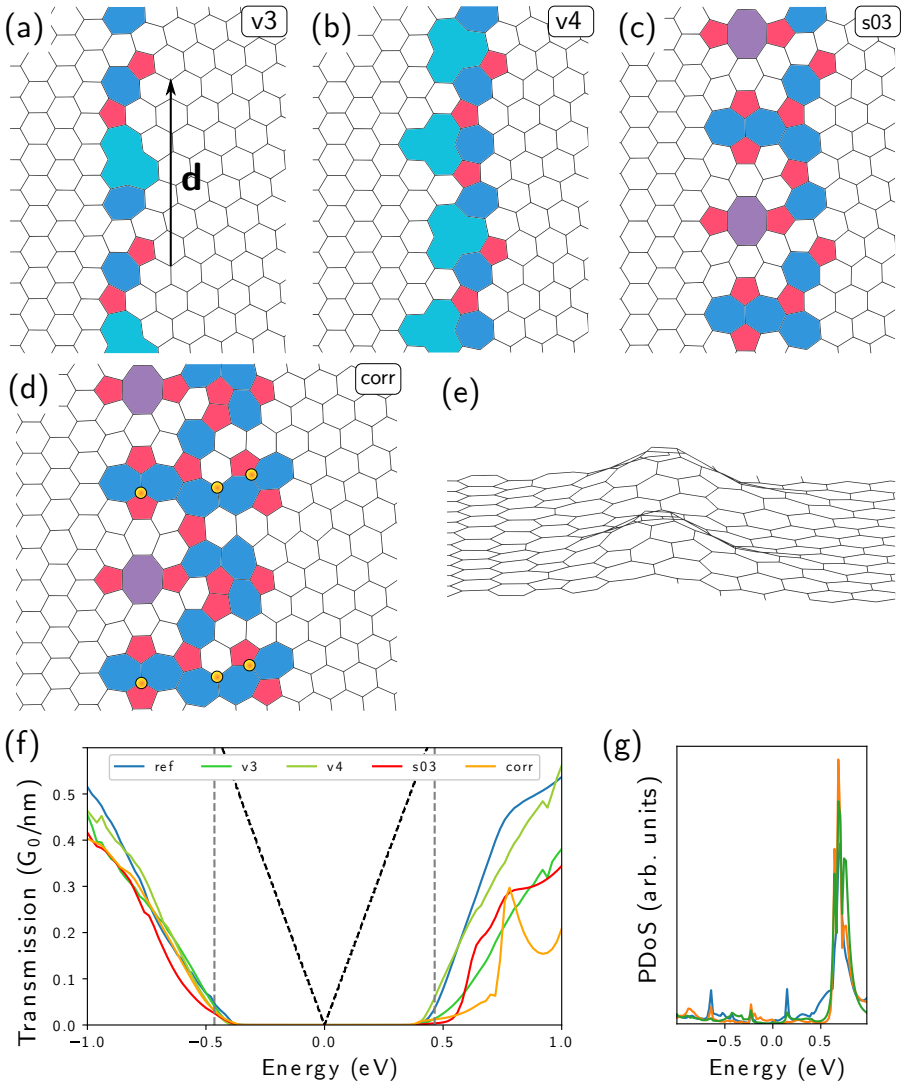

Figure 5.5: First-principles electronic transport through disordered GBs in PG. Atomic structures of the $(6,0)|(4,3)(\theta = 25.3°)$ class-II GB for the initial pattern (AMC-1d) with **(a,b)** highly concentrated vacancies (c_1^* and c_2^*), a larger inter-connectivity region with **(c)** planar geometry and **(d,e)** out-of-plane buckling (respective top and side views). Carbon rings containing a vacancy are highlighted in azur while pentagons, heptagons and octogons are displayed in red, blue and purple, respectively. **(f)** Zero-bias total conductance per unit length through those disordered GBs as a function of energy compared to the ones of pristine graphene (black dashed line) and the initial pattern (black solid line). The theoretical transport gap is indicated by vertical dashed lines. **(g)** Projected DoS as a function of energy corresponding to carbon atoms highlighted in yellow in the corrugated system.

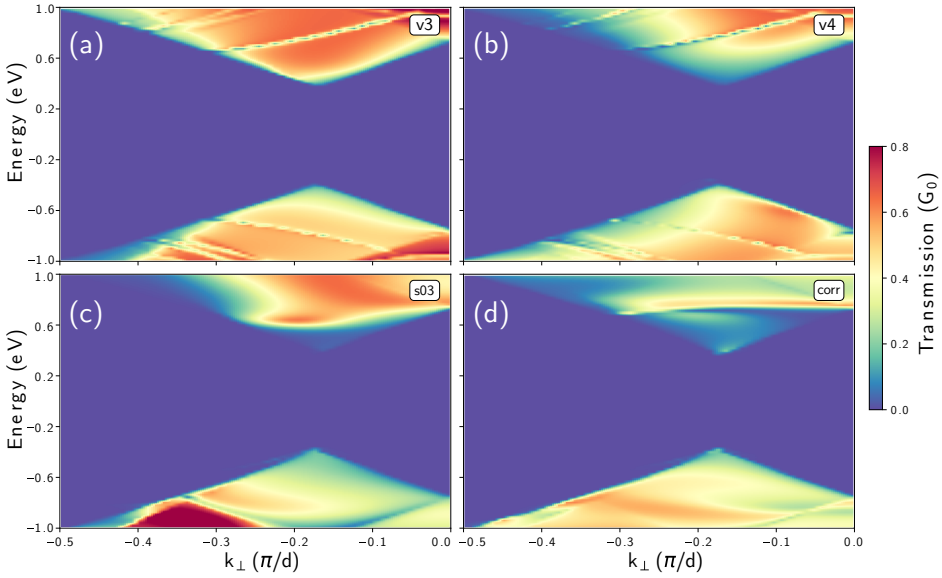

Figure 5.6: First-principles transmission probabilities for the $(6,0)|(4,3)(\theta = 25.3°)$ class-II GB as a function of transverse momentum and energy. The transmission map is given for the initial pattern (AMC-1d) with **(a,b)** highly concentrated vacancies (c_1^* and c_2^*), a larger inter-connectivity region with **(c)** planar geometry and **(d)** out-of-plane buckling.

electronic transport. A transmission peak is found at 0.8 eV in the corrugated case, suggesting that local electronic perturbations improve electronic transport at specific energies, as previously suggested by experimental observations [193]. In order to clarify the role of those charge redistribution effects, the local DoS is investigated inside the scattering region (see Fig.5.5(g)). For the buckled configuration, a sharp peak in the DOS is found at 0.8 eV. This result is in agreement with STM measurements on periodic GBs, whose occurrence generates sharp LDoS peaks in the tunneling spectra [243]. This peak is unambiguously associated to a series of atoms distributed along a line of heptagons, as highlighted in Fig.5.5(d). This observation reveals that odd-membered rings induce resonant states slightly above the Fermi energy, as already demonstrated in carbon nanotubes [244, 245]. Since an enhancement in the DOS that is non-orthogonal to transport is unequivocally related to an increase in transmissions, charge redistribution effects are found to enhance the total conductance around 0.8 eV. Overall, corrugation plays an important role in the degradation of transport, assumingly due to the weakening of the delocalized π-bonds [246].

Interestingly, the transmissions of holes is observed to be weakly sensitive to the type of disorder. An investigation of the transmission probabilities reveals that scattering modifies differently the transport properties of each defective system, with a non-trivial dependence in energy and momentum, as depicted in Fig.5.6. This means that the transmission of holes is significantly sensitive to the nature of defects but this effect is not reflected in the momentum-averaged conductance.

Lastly, the transport gap is found to remain constant despite the types of disorder, consistently with Eq.5.1. Note that transmissions are reduced by one order of magnitude around 0.5 eV for larger inter-connectivity regions, indicating that an *effective* transport gap would depend not only on d but also on the detailed GB topology in the case of poorly-connected grains [234].

5.4 CONCLUSION

In summary, the transport properties of realistic GBs were described using *ab initio* numerical simulations.

At first, two simple configuration of GBs were studied. In agreement with previous reports, metallic and semi-conducting characteristics were observed.

The effects of disorder on charge transport were studied by considering more complex atomic structures, including various types of non-hexagonal rings, vacancies, larger inter-connectivity regions with planar and corrugated geometries. The objective was to model GBs as close as possible to experimental observations.

The metallic GBs were reported to exhibit sensitively reduced transparency in the presence of non-hexagonal rings, as scattering increases due to a lesser inter-connectivity between the grains.

For more realistic semi-conducting GBs, the transport gap was found to be qualitatively consistent with theoretical predictions, showing a well-defined inverse relationship with the smallest apparent periodicity and a substantial resilience to disorder. Inside this transport gap, leakage currents as large as 10^{-2} G_0/nm were observed if a small amount of disorder breaks the initial periodicity. Outside the transport gap, poorly-stitched GBs were reported to show significantly reduced electronic transmissions. Charge redistribution effects can nonetheless induce substantial variations at specific energies, depending on the detailed topology of the boundary.

Our conclusion is that random disorder assumingly standardize the transport properties of GBs by blurring the classification between each transport behavior. On the one hand, imperfections tend to enhance scattering and thus reduce the overall transmissions. On the other hand, the reflective character fades away in disordered reflective systems due to the emergence of leakage currents. In consequence, experimentally measured conductances are presumably quite universal and robust [223], independently of theoretical predictions. Lastly, the finding of conductances almost comparable to pristine graphene for well-stitched GBs with significant defects concentrations supports the feasibility of integrating PG in electronic devices.

Some comments are addressed before concluding this chapter. It is important to note that disorder is always introduced in a periodical manner. Line defects are however intrinsically non-periodic as GBs resemble more or less to periodic arrays of point defects. This discrepancy could induce slight perturbations to results drawn on such assumption. The imperfections considered so far represent a non-exhaustive set of atomic structures that may not encompass the degrading effects of disorder on the whole. For example, chemical functionalization could have been investigated in order to describe more comprehensively scattering mechanisms occuring at GBs. Seifert *et al.* [247] suggested that the electronic properties of PG are largely dependent on the nature of functional groups, which are intrinsically present at GBs due to their high chemical reactivity. In spite of these limitations, the present study represents an improvement in the understanding of electronic transport across PG. The ambition is that such atomistic characterization may pave the way towards the integration of graphene-based devices on a industrial scale.

6 TMDS-BASED LATERAL JUNCTIONS

The FET is integral to many electronic devices, acting as the elementary component in integrated circuits where it allows energy-efficient high-speed operations. FETs are three terminals systems composed of source, drain and gate electrodes. The source and drain electrodes are connected through a semiconducting channel, isolated from the gate electrode by an insulating material. The effective operation of FETs relies on efficient electrostatic coupling between the gate and the channel, without electrons being allowed to flow between the two. As previously discussed, 2DMs have attracted enormous interest during the past decade for the fabrication of electronic devices that could enable an extension of Moore's law. Those materials show relatively high mobility and proper electrostatic control while being atomically thin, which provides a compelling platform for the design of extremely thin devices absent of short-channel effects [14].

Since the first isolation of monolayer graphene in 2004 by Novoselov *et al.* [18], the range of 2DMs has been extended to hexagonal boron nitride (h-BN), transition metal dichalconegides (TMDs), silicene, phosphorene, MXenes, ... Among those materials, TMDs stand out as the most promising candidates for transistor applications [59]. TMDs constructed from group VI transition metals Mo and W and combined with chalcogens S and Se are direct band gap semiconductors in the monolayer form, in contrast to their indirect band gap in the bulk. Such materials may be synthesized through CVD, the most practical method for the production of high-quality large-area flakes that is compatible with existing industrial processes. Interestingly, theoretical calculations predict promising charge carriers mobilities in TMDs, with estimation in the range of $100 - 1000\ \mathrm{cm^2V^{-1}s^{-1}}$ at room temperature [248, 249]. Experimentally measured mobilities are in practice significantly lower [25], due to the presence of disorder and scattering sources, combined the reduced dielectric screening in atomically thick materials that increases sensitivity to environmental factors. As a proof of concept, the first transistor based on single-layer MoS_2 was demonstrated by Radisavljevic *et al.* in 2011 [250]. The devices showed excellent operational properties, such as high on/off ratios, high on

currents, a low sub-threshold swing (SS) of 74 mV dec^{-1} and a room-temperature mobility of the tens of $cm^2V^{-1}s^{-1}$ due to the deposition of a thin layer of high dielectric constant material.

Owing to the synthesis methods, the presence of the substrate or other post-processing conditions, strain is always present in TMDs monolayers. Interestingly, these materials were shown to display high strength, with breaking occurring at an effective strain of 6% to 10% [251], substantially larger than the fracture strain of silicon [252]. This unique feature of 2DMs allows for engineering of the electronic structure solely through the application of strain, defined here as straintronics. A large number of theoretical and experimental works have investigated the role of strain on the electrical properties of TMDs [253, 254]. As it concerns electronic devices, strain is expected to modulate the band gap [65, 255], the electron mobility [256], the charge carriers effective masses and on-state currents in transistors [257–259]. In a nutshell, theoretical and experimental observations evidence that TMDs represent highly promising candidates for the realization of large-area, high performance flexible devices and circuits [59].

In recent years, the development of 2DMs has lead to the construction of heterostructures (HSs) by combining layers of crystals that have some or no atomic species in common and/or incommensurate lattices. Such HSs are characterized by dangling-bond free surfaces, ultra-thin body and atomically sharp interfaces. Although each material possesses a distinctive set of electronic properties, the formation of HSs enables the enhancement or the emergence of tailored functionalities that might be absent in the pristine counterparts [83], offering exciting opportunities for inventively engineering devices at the atomistic scale [21]. As an illustration, HSs based on 2DMs displayed unique characteristics such as valley splitting by magnetic proximity effect [260], spatially indirect excitons [261] and superconductivity in bilayer graphene rotated by a magic angle [262].

Single-layer TMDs can be stacked together in order to form vertical HSs [263] while their lateral analogues are constructed by stitching them together [264]. In contrast to the former architecture, heterojunctions have attracted less attention from the scientific community, for the most part due to complications in the growth process. Similarly to their pristine counterparts, TMDs-based HSs can be grown using CVD. Lateral HSs were first realized using edge epitaxy, where the growth of a TMD crystal occurs on the active edge of the different TMD crystal [84]. Several groups implemented this strategy in a one-step approach and

demonstrated the synthesis of MoS_2-WS_2 [265], $MoSe_2$-WSe_2 [266], MoS_2-$MoSe_2$ and WS_2-WSe_2 [267] lateral junctions. Lateral stitching of dissimilar chalcogens and transition metals (MoS_2-WSe_2) were realized in the following years using a two-step synthesis scheme [268], a technique yielding atomically sharp interfaces.

In this context, the charge transport properties of MoS_2-WSe_2 lateral junctions are characterized in this study based on the FET architecture (see Fig.6.1) in the framework of straintronics. Nano-scale band engineering is proposed through the application of a uniaxial strain along the transport axis. Owing to the modification in band offset at the interface, current through the junction can be modulated by deforming the central region of WSe_2. This current modulation is shown to improve with the length of the channel and to be resilient to deviations from its ideal operational framework. The ambition of this work is to illustrate the prospects that hold lateral HSs as an unique platform for the design of strain-induced transport mechanisms.

The transport characteristics of the field-effect device are computed in the ballistic regime within the Landauer formalism. The Perdew-Burke-Ernzerhof (PBE) [269] implementation of the GGA functional is used to describe the exchange-correlation interaction. Applying the Monkhorst-Pack scheme [105], the electronic structure of TMDs are computed with a k-points sampling equivalent to a $16 \times 16 \times 1$ mesh in the unit cell. To avoid spurious interaction, an inter-layer distance of 20 Å is employed. The basis set is such that Mo, S and Se atoms are described by *s2p1d1* orbitals while W atoms are characterized by *s2p2d2* orbitals. The association of pseudo-atomic localized basis functions and one to one commensurate lattices between MoS_2 and WSe_2 enables the characterization of substantially large system, extending over tens of nanometers.

6.1 TRANSITION METAL DICHALCOGENIDES

As a preliminary step, the electronic structures of the isolated TMDs are investigated. Those materials consist of an hexagonal lattice of transition metal atoms (M) surrounded by an upper and lower layer of chacolgen atoms (X) with a MX_2 stoichiometry.

The lattice parameters for MoS_2 and WSe_2 were computed to be $a_0 = 3.21$ Å and $a_0 = 3.34$ Å, respectively. Those results are in good agreement with first principles calculations based on plane wave basis

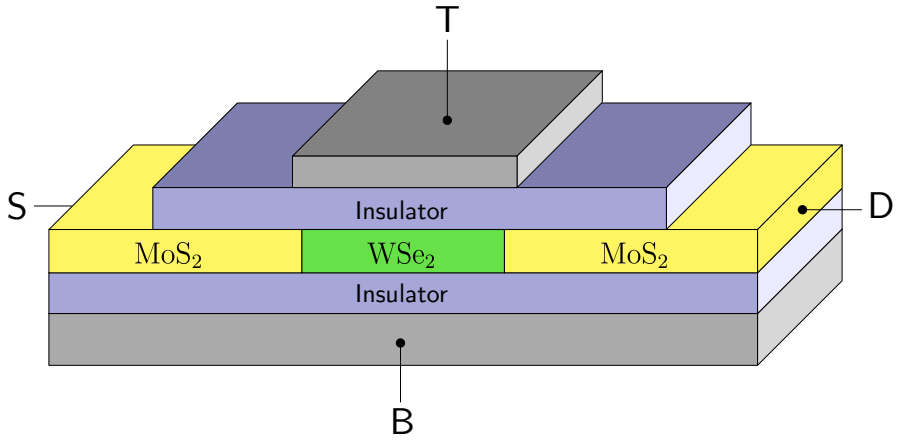

Figure 6.1: FET-device based on 2D lateral heterojunctions: the elementary transistor is composed of top (T) and back (B) gates, source (S) and drain (D) while the channel is constructed by inserting a WSe_2 strip inside a MoS_2 layer.

sets [270] and with experimental measurements done by neutron scattering [271] and X-ray diffraction [272] techniques.

At the monolayer limit, MoS_2 and WSe_2 are direct band gap semiconductors, as illustrated in Fig.6.2. The computations done with the GGA exchange-correlation functional yields a band gap (E_g) of 1.63 eV and 1.33 eV for MoS_2 and WSe_2, respectively. Those results are in good agreement with state-of-the-art computations based on DFT [273]. The experimental value of the band gaps for single layer MoS_2 and WSe_2 were reported to be 2.15 eV [274, 275] and 2.08 eV [275], respectively. The discrepancy with theoretical predictions originates from DFT notoriously underestimating the band gaps in crystals [269]. Theoretical predictions can however be improved by calculating the quasi-particle band structure using GW techniques and by including excitonic effects through the Beth-Salpeter equation approach [276]. The valence band maximum (VBM) and the conduction band minimum (CBM) are located at the two inequivalent high-symmetry points K and K', which denote the corner of the hexagonal BZ. Importantly, the lack of inversion symmetry results in a spin splitting of the electronic bands driven by spin-orbit coupling (SOC). The magnitude of this effect is much larger in the valence band, with a calculated splitting of 155 meV in MoS_2 and 487 meV in WSe_2. This trend between TMDs is explained by the relativistic nature of SOC that depends on the atomic mass as Z^4. The spin splitting is opposite between the K and K' valleys, owing

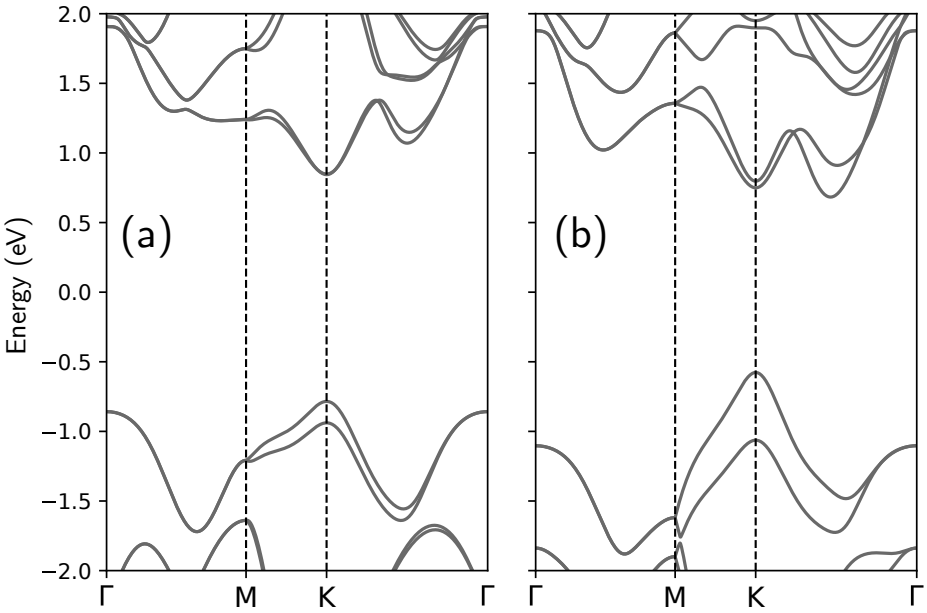

Figure 6.2: Electronic properties of monolayer TMDs. The band structures of monolayer **(a)** MoS_2 and **(b)** WSe_2 are depicted.

to time-reversal symmetry. This means that the valley polarization of a charge carriers automatically determines its spin polarization for a given electronic band. This property is referred to as spin-valley coupling [277].

6.2 LATERAL HETEROJUNCTIONS OF TMDS

Covalent bonding in lateral HSs limits the constitutive TMDs to display relatively small lattice mismatch, restricting our analysis to M={Mo,W} and X={S,Se}. Among those materials, the MoS_2-WSe_2 lateral junction stands out as the configuration with the largest lattice mismatch and the most chemically diverse system at the same time. For these reasons, the present work is focused on this specific junction, as it offers an especially interesting playground for the design of novel transport phenomena.

The lateral junction is constructed by inserting a WSe_2 stripe inside a MoS_2 region. The WSe_2 stripe is constrained along the interface line so that its forms a commensurate structure with MoS_2 while it is strained perpendicularly to the junction by an amount $1 + \epsilon_x$, as depicted in Fig.6.3(a). The total strain is therefore expressed as $\epsilon = (\epsilon_{zz} + 3\epsilon_{ac})/4$,

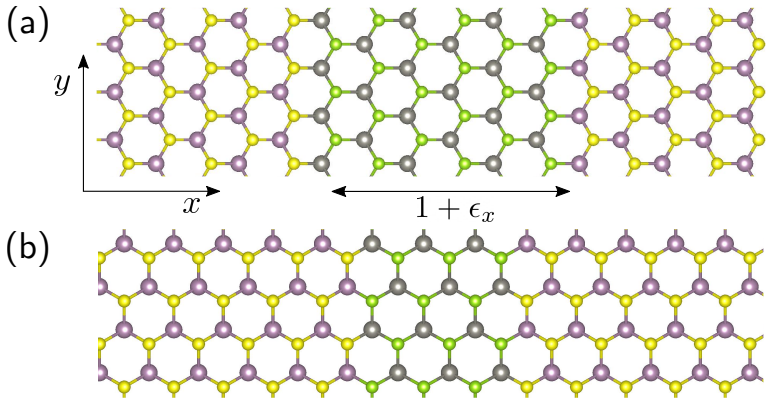

Figure 6.3: Atomic structures of MoS_2-WSe_2 lateral heterojunctions with **(a)** zigzag and **(b)** armchair interfaces, respectively. The strain along the transport axis (ϵ_x) is applied in the central strip of WSe_2.

where ϵ_{zz} and ϵ_{ac} represent deformation in the zigzag and armchair directions, respectively. This relation is valid in the limit of low strains, when the contribution of quadratic terms is negligible. Two types of interfaces are considered in the following: zigzag and armchair (see Fig.6.3). Both interfaces are observed experimentally, even though the zigzag direction tend to be the preferable growth direction for the lateral interface [85, 265, 268, 278, 279].

An essential feature of HSs lies in the relative alignment of the semiconductors energy bands at the junction, i.e. the band offset. In most cases, the band gaps and the Fermi levels of both materials are usually different, resulting in a discontinuous arrangement of the band structures so that the Fermi level remains constant throughout the system. Three types of band alignment are identified: (i) type-I corresponds to configurations where one material band gap is nested inside the other band gap, (ii) type-II is when the CBM is inside the other material band gap (also called staggered band offset), (iii) type-III refers to a broken band alignment where the CBM of one material is below the VBM of the other material.

Band offset in TMDs is dictated by the transition metal d-orbitals and the chalcogenides p-orbitals [280]. In MoS_2 for example, the VBM consists of the $d_{x^2-y^2}$ and d_{xy} orbitals of Mo and the p_x and p_y orbitals of S. Similarly, the CBM has the character of the d_{z^2} orbital of Mo and the p_x and p_y orbitals of S. Each band extremum originates from the repulsion between the corresponding orbitals, as defined by their overlap integral and their difference in onsite energies. For a larger

overlap integral or a smaller energy difference, the band extrema are pushed upwards in energy (with respect to the vacuum energy level). As the X atomic number increases, its *p*-orbitals becomes shallower and are located at higher energy, resulting in a larger overlap and a smaller energy difference with the M orbitals. Additionally, the band extrema are pushed upwards when the M atomic number gets larger, as the energy of the *d*-orbitals increases. This means that the VBM and CBM of WSe_2 are located at a higher energy than for MoS_2.

Extensive experimental works were carried out to assess the electronic properties of HSs by means of scanning tunneling spectroscopy (STS). Chiu *et al.* [275] used X-ray photoelectron spectroscopy to determine the band offset in a MoS_2-WSe_2 vertical HS. A type-II alignment was found, with a valence band offset (VBO) of 0.83 ± 0.07 eV and a conduction band offset (CBO) of 0.76 ± 0.12 eV. Band offset is however subject to intrinsic discrepancies between lateral and vertical HSs. In the latter, interlayer coupling occurs through vdW interaction while it depends for the former on the lattice mismatch and the intrinsic electric polarization (or electric dipoles) caused by bonding dissimilarities. Wei *et al.* [281] used first-principles simulations to show that charge transfer across the interface results in band bending in lateral TMDs quantum wells, a feature absent in stacked systems. Additionally, TMDs quantum wells represent an intriguing platform for the realization of novel phenomena due to the emergence of quantum confinement. Lastly, a structural discrepancy stems from the interface dimension, which is 1D in lateral junction but 2D in vertical structures. Zhang *et al.* [85] studied the MoS_2-WSe_2 lateral junctions by means of STM in order to measure the strain distribution and the band alignment. The misfit strain was found to induce a type II to type I band alignment transformation, due to the band gap reduction in strained MoS_2. Correspondingly, the VBO was approximately estimated to 0.65 ± 0.05 eV while the CBO was determined to be 0.40 eV.

The junction local density of states (LDoS) extracted from *ab initio* calculations is presented in Fig.6.4(e-g), enabling the determination of the band offset. In complement to the LDoS, the excess charges at the zigzag interface are displayed. These figures intend to illustrate the joint roles of strain and the type of interface. First, the amount of charge exchanged depends on the type of covalent bonds at the junction. Fig.6.4(a-d) show a net charge gain at the M side as the metal *d*-orbitals act as electron accommodators. Conversely, charge accumulation is absent in the armchair configuration as Mo and W atoms form equi-

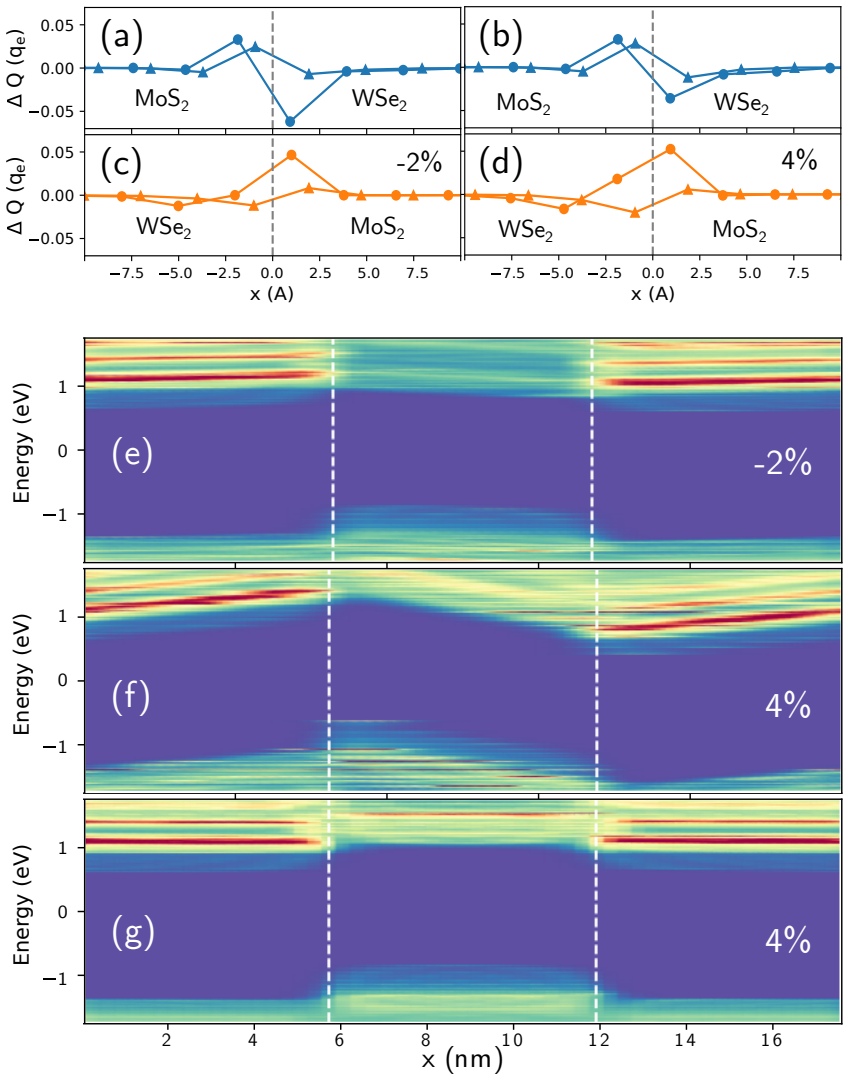

Figure 6.4: Interfacial properties of MoS_2-WSe_2 lateral heterojunctions. **(a-d)** Excess charge as a function of the distance from the interface (indicated by a dashed line), as obtained from a Mulliken population analysis, for the zigzag interface at **(a,c)** $\epsilon_x = -2\%$ and **(b,d)** $\epsilon_x = 4\%$. The dots and triangles represent M and X atoms, respectively. **(e-g)** LDoS of junctions at various strains for **(e,f)** a zigzag and **(g)** an armchair interface.

valent covalent bonds [282]. Second, a zigzag interface results in two asymmetric junctions (WS2 or MoSe2) whereas an armchair interface has a two-fold rotational symmetry (WS2 and MoSe2). This structural (a)symmetry generates a similar (a)symmetry in the charge redistribution between the two interfaces, as demonstrated for the zigzag configuration. These two discrepancies imply that zigzag and armchair interfaces show contrasting LDoS. At similar strain profile, the LDoS is found to be symmetric for the armchair direction while band bending occurs for the zigzag interface, in agreement with Refs.[281, 282]. The slope of the bands in WSe_2 is dictated by the electrical polarization generated by the charge build-up in MoS_2. The electric dipole located at each interface creates an electric potential gradient that is negative (positive) in the left (right) region of WSe_2. Consequently, the charge carrier energy is increased (decreased) as it penetrates into the stripe. Strain influences the amount of charge transferred across the junction as well as the band gap of WSe_2. The former effect alters band bending while the latter affects the band offset. Note that a detailed discussion of the effect of strain on the electronic properties of TMDs is provided later on. Importantly, the tuning of the CBO through mechanical deformation is at the core of the present research. Finally, the band offset is computed for the most stable configuration ($\epsilon_x = 0.5\%$) with a WS_2-like interface. The VBO and the CBO are found to be 0.4 eV and 0.22 eV, respectively, which corresponds to a type II band alignment.

6.3 STRAINTRONICS IN LATERAL TMDS JUNCTIONS

In the early 2000s, band engineering based on the introduction of artificial strain into SiGe films embedded in a PMOS transistor lead to a breakthrough in semiconductor electronics, with dramatic performance enhancement relative to unstrained devices [283]. For instance, strain engineering (or straintronics) led to a fourfold increase in hole mobilities in silicon transistors [284].

Substantial modifications of the band gap of 2D materials were reported experimentally for moderate strain profiles [253, 254], demonstrating the interest of straintronics in 2D semiconductors. Extensive *ab initio* calculations based on DFT were performed in order to study the effect of mechanical deformation on the electronic properties of TMDs [65]. A direct-to-indirect band gap transition occurs at small tensile strains of $1\% - 2\%$ for transition metal disulfides, with a larger threshold for selenides. In addition, the band gap is reduced by both tensile and

shear strain. A semiconductor-to-metal transition is observed upon application of a 10% biaxial tensile strain, with a more rapid diminution of the band gap as compared to the uniaxial case. Such large value of strain corresponds to the maximum amount of deformation attainable in TMDs [251]. As concerns the transport of charge carriers, the strain-induced tuning of the band gap results in a corresponding modulation of the electrical conductivity. This piezoresistive effect was demonstrated by Manzelli *et al.* [59] in MoS_2.

Strain can be introduced in 2D materials through miscellaneous strategies, such as bending a flexible substrate, elongating an elastic substrate, piezoelectric stretching or substrate thermal expansion [253]. The first two methods enable the application of uniaxial strain while the latter strategies yield biaxial strain. Interestingly, a MoS_2 monolayer was uniaxially strained up to 2.4% by bending its polycarbonate substrate [285]. A similar approach was later on successfully employed to introduce mechanical deformation in WSe_2 [286].

Lattice-mismatched lateral HSs represent an intriguing possibility for the production of novel electronic structures via strain engineering. As mentioned above, the electronic properties of the TMDs are substantially influenced by the strain distribution caused by the lattice mismatch. In addition, the deformation profile can be controlled through the growth process [279], the type of substrate [85] or the supercell dimension [86], such that strain is applied at specific location with precise magnitude. This combination of these features with atomically sharp lateral interfaces enable the design at the nano-scale of the electronic structures. For example, Zhang *et al.* [85] reported spatial modulation of the band structure in the MoS_2 region for a MoS_2-WSe_2 lateral HS grown on top of an underlying WSe_2 monolayer. Similarly, Xie *et al.* [86] adjusted the epitaxial strain by accurately designing the supercell dimension, showing the tunability of the (opto)electronic properties of the MoS_2-WSe_2 junction. In spite of those experimental demonstrations of electronic structure engineering, only a handful of theoretical studies investigated the integration of TMDs-based lateral HSs in semiconductor devices.

In the following, we present the conductance obtained for the HSs represented in Fig.6.3 in order to draw preliminary observations for potential FET applications. The characterization of the role of strain demands highly accurate computations performed on a system of significant size, typically beyond the tens of nanometers. On the one hand, first-principles methods allow for a straightforward description of

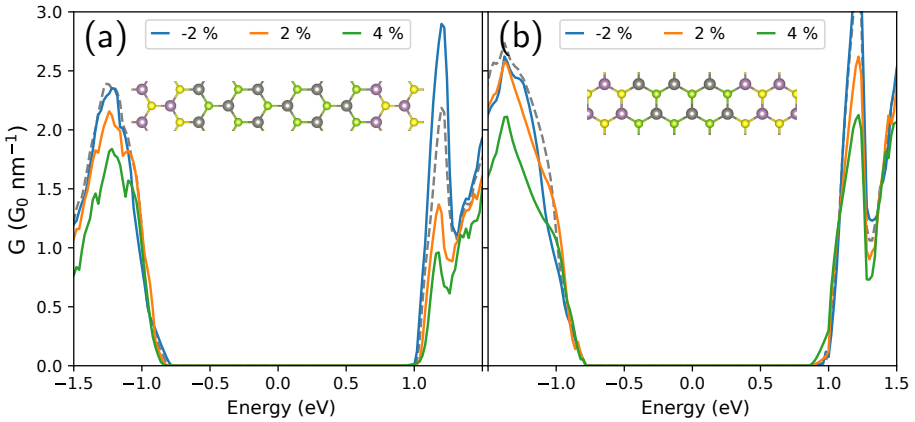

Figure 6.5: Electronic transmissions per unit area as a function of energy for different strains applied on WSe_2 along x, corresponding to the **(a)** zigzag and **(b)** armchair interface, respectively. Transmissions for unstrained WSe_2 are depicted in dashed lines. The width of the strip is 3 unit cells of WSe_2. Inset: illusration of the geometry.

strain and interfacial coupling, as opposed to semi-empirical techniques for which a proper calibration of the parameters is required. If so, the Hamiltonian is constructed using an effective mass approach [287, 288] or maximally localized Wannier functions [289, 290], such that the model includes strain effects [291]. On the other hand, tight-binding methods exhibit a linear scaling with respect to the size of the system compared to the cubic scaling of DFT. In this context, an adequate trade-off between accuracy and scaling is needed. The issue of correctly describing interfacial coupling is of uttermost importance. Choukroun *et al.* [289] calculated them as the average of the coupling parameters of the materials on either side of the interface. Marin *et al.* [290] showed that the values assigned to coupling parameters changed marginally the transfer characteristics of the PdS_2 lateral HS-FET. This observation was however done on a monolayer-bilayer PdS_2 junction and not on a genuine heterogeneous system. It remains an open question if TB models can capture the complicated physics of strained lateral HSs. In this work, *ab initio* calculations are performed on devices extending over 20 nm through proper design of the basis set, the spin-polarization and the geometry, as detailed in the ensuing paragraphs.

Electronic transmissions are initially calculated in the non-collinear framework for a junction formed by repeating n rectangular unit cells of WSe_2 along the transport axis. The results for $n = 3$ are presented

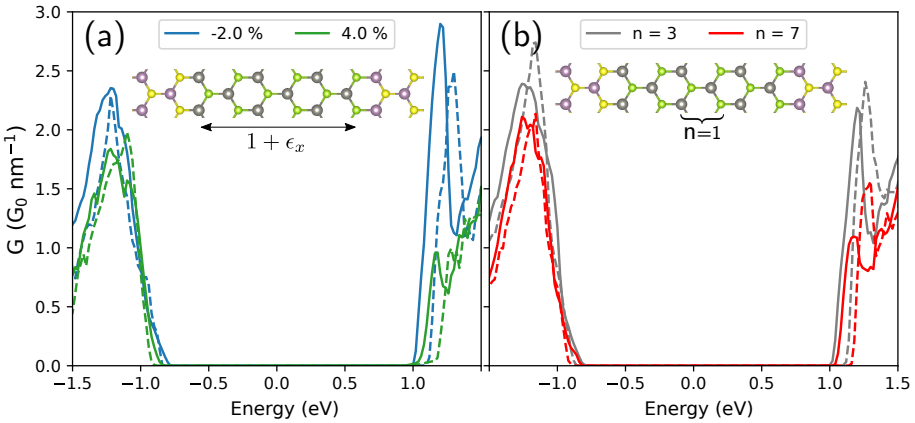

Figure 6.6: Electronic transmissions per unit area as a function of energy for unpolarized and non-collinear spin-polarized calculations, represented in dashed and solid lines, respectively. **(a)** Conductances at $\epsilon_x = -2\%$ and $\epsilon_x = 4\%$, where the width of the WSe_2 strip is $n = 3$. **(b)** Conductances for different widths of the WSe_2 strip, which remains unstrained. Inset: illustration of the parameter used for comparison.

in Fig.6.5. As a general observation, tensile strain applied to WSe_2 reduces $T(E)$ in the conduction and the valence bands. The effect of strain appears to be relatively independent of the type of interface, stemming from the reasonably isotropic electronic properties of TMDs at low energy [292]. Further calculations are performed only on the zigzag interface, as this configuration coincides with experimental observations and scales better with the channel length.

Collinear spin-unpolarized and non-collinear spin-polarized calculations are then compared. The objective is to reduce four-fold the dimension of the Hamiltonian by disregarding the effect of SOC. The comparison is performed on two subsets to address the relevance of charge transport. First, strain is applied on WSe_2 for $n = 3$. Second, the quantum well is extended from $n = 3$ to $n = 7$ in the unstrained configuration. The corresponding results are presented in Fig.6.6. A qualitative agreement is obtained between both frameworks and for each subset. The main discrepancy originates from the estimation of the band gap due to spin splitting in the valence and conduction bands. Although SOC substantially affects the electronic bands, its impact on the charge redistribution at the interface is negligible. In addition, the strain-induced band gap modulation in TMDs is independent of SOC [293]. It follows that the tuning of the band alignment

through mechanical deformation is well characterized by collinear spin-unpolarized calculations.

In the ensuing section, the operation of a double-gated FET is characterized using the above-mentioned framework.

6.4 FIELD-EFFECT TRANSISTOR OF LATERAL TMDS JUNCTIONS

Most properties of interest in FETs originate from the statistics of electrons in the conduction band and holes in the valence band, depending on the sheet doping. That is to say that the device characteristics are completely determined by the transport properties of the mobile carriers and their electrostatic field-effect control by the gates [294]. Some essential parameters related to the channel are the carrier density ($\tilde{n}$), the mobility (μ) or the quantum capacitance (C_q).

In order to simulate the FET using *OpenMX*, some approximations are imposed. It is well established that MoS_2 is typically n-doped while WSe_2 exhibit ambipolar characteristics [76]. An electron doping of 5×10^{12} cm^{-2} is defined in the MoS_2 region far from the interface. This value is in agreement with surface densities reported in the literature, as obtained by means of liquid gating and electrostatic gating [295]. Note that the strain-induced current modulation presented hereafter has also been verified at lower carrier densities. The band structure is assumed to be shifted rigidly upon application of a back gate. That is to say that the electronic properties of the materials remain unchanged by doping. Zhao *et al.* [296] used self-consistent tight-binding techniques to demonstrate the reliability of the rigid shift approximation in single-layer TMDs at doping levels below 10^{13} cm^{-2}. The drain-source voltage (V_{ds}) is set to 0.1 V for every system. In the *OpenMX* software, it is not possible to introduce an insulating material between the channel and the gates. As detailed further on, this technical limitation restricts the range of doping that is attainable in the WSe_2 channel when applying a top gate voltage (V_{gs}). Based on those assumptions, the current across the junction (I_{ds}) and the charge carrier density in the channel ($\tilde{n}$) are computed by first-principles simulations for small compressive and tensile strains. The transport mechanisms are understood through the lens of a simple quantum tunneling model, using information drawn from the band structure of strained WSe_2. Finally, the devices characteristics are analyzed in more realistic setups, by gating a section of the MoS_2 region, extending the channel length or straining the MoS_2 contacts.

The gate voltage is treated by adding an electric potential (U_g) to the total Hamiltonian. This term is defined as

$$U_g(x) = U_g \exp\left[-\left(\frac{x - x_g}{L_g}\right)^8\right] \tag{6.1}$$

resembling a step potential applied by the gate, where L_g and x_g represent the center and the length of the top gate, respectively. In the lateral heterojunction, L_g coincides with the size of the WSe_2 region (L_{WSe_2}), if not stated otherwise. The gate voltage is therefore determined by U_g, although the connection between the two depends on the operation regime of the FET. Altogether, the applied voltage affects the channel and the insulating material [294]

$$V_{gs} = eU_g + V_{in} \tag{6.2}$$

where V_{in} denotes the voltage inducing band bending in the dielectric layer. In the sub-threshold region of a FET, most of the gate voltage drops in the insulator and is therefore applied to the channel, implying that $V_{gs} \approx eU_g$. The correctness of this approximation is discussed later on, when the carrier density in the WSe_2 channel is studied in more details.

The current through the junction is obtained using the Landauer formula. This formalism represents an adequate approach to compute electronic transmissions in nano-scale devices, where transport is ballistic and coherent. The current is therefore written as

$$I_{ds} = \frac{2e}{h} \int_{-\infty}^{\infty} T(E) \left[f_s(E) - f_d(E)\right] dE \tag{6.3}$$

where the indices s, d correspond to the source and the drain. Note that $T(E)$ also includes the number of propagating mode in the channel, which is proportional to the DoS.

In this framework, the current is computed as a function of the electric potential for the lateral HS at different strain profiles, as illustrated in Fig.6.7(a). Those results roughly resemble the transfer characteristics in the sub-threshold regime, representing an ideal configuration where the voltage is applied solely to the channel. The simplicity of this model does not allow us to extract certain features such as the sub-threshold swing (SS) in a reliable manner. Nonetheless, it enables an accurate characterization of electrostatic gating and strain-related effects on the junction transport properties. In Fig.6.7(a), strain-induced modulation

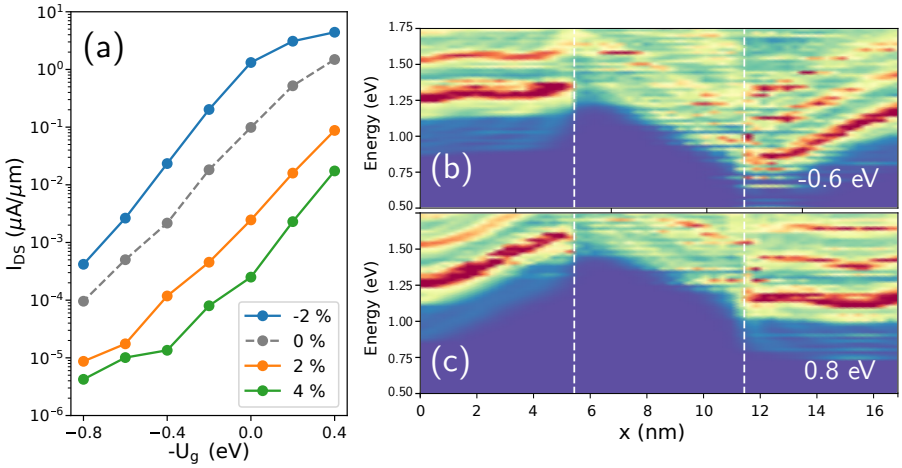

Figure 6.7: Transport properties of a MoS_2-WSe_2 based FET . **(a)** Transfer characteristics for the lateral heterojunctions of MoS_2 with a central strip of WSe_2 for a gate length (L_g) of 5.8 nm and an applied bias of $V_{ds} = 0.1$ V. The corresponding LDoS for $\epsilon_x = 4\%$ at **(b)** $U_g = -0.6$ eV and **(c)** $U_g = 0.8$ eV.

of I_{ds} is observed, with tensile strain decreasing exponentially electronic transmissions (and conversely). The proper operation of the top gate is verified in Fig.6.7(b,c), where the LDoS is represented at $U_g = -0.6$ eV and $U_g = 0.8$ eV. The current increased exponentially with decreasing gate potential due to the larger energy barrier in the WSe_2 region.

In order to compare the transfer characteristics with hands-on device measurements, U_g needs to be translated into an experimentally accessible quantity. In practice, the inversion charge (Q_{inv}) in the channel can be calculated from the capacitance-voltage characteristics, providing an immediate determination of the carrier sheet density. From a theoretical perspective, $\tilde{n}$ is obtained by computing the LDoS inside the channel. The total number of electrons (N) per area surface (S) is calculated such as

$$\tilde{n} = N/S = \int_{E_c}^{\infty} f\left(E - E_F\right) \rho\left(E\right) dE \tag{6.4}$$

where $f\left(E - E_F\right)$ and $\rho\left(E\right)$ are the Fermi-Dirac function and the electronic DoS, respectively. The integration is performed on all energy levels above the CBM. In the case of free electrons in a 2D Fermi gas, the density is written as [294]

$$\rho\left(E\right) = \left(g_s g_v m^* / 2\pi\hbar^2\right) \sum_i \Theta\left(E - E_i\right) \tag{6.5}$$

in which $\Theta(E)$ represents the Heaviside function, E_i indicates the band edges, m^* denotes the carriers effective mass, g_s and g_v are the spin and valley degeneracy factors, respectively. The effective mass is inversely proportional to the bands curvature and expresses the change in group velocity to a change in crystal momentum. This expression is correct near the VBM and the CBM, where the electronic band dispersion is accurately described by the parabolic approximation, i.e. $E(k) = \hbar^2 k^2 / 2m^*$. If one considers a single conduction band, $\tilde{n}$ is then expressed as

$$\tilde{n} = (g_s g_v m^* / 2\pi\hbar^2) k_B T \ln\left\{1 + \exp\left[\left(E_F - E_c\right) / k_B T\right]\right\} \tag{6.6}$$

for a system at temperature T. The effect of the top gate is to tune the carrier density in the channel. It follows from the previous equation that the Fermi level of the system is affected in a similar manner. The electric potential is then related exponentially to the carrier concentration. In the WSe_2 channel, one has

$$\tilde{n} = (g_s g_v m^* / 2\pi\hbar^2) k_B T \ln\left\{1 + \exp\left[\left(eU_g - E_F^0\right) / k_B T\right]\right\} \tag{6.7}$$

where E_F^0 corresponds to the Fermi level in the MoS_2 contacts. This equation is valid at low gate voltage, when $V_{gs} \approx eU_g$. At higher gate voltage, when the FET is strongly "on", $\tilde{n}$ and V_{gs} depend linearly on one another [294].

Fig.6.8(a,b) depict the sheet carrier densities computed for WSe_2 in the isolated form and in the center of the channel (denoted $\tilde{n}_{0,WSe_2}$). The strong similarity between the two systems indicates that the channel effectively behaves as a 2D electron gas far enough from the junction. The slight disagreement is supposedly created by the limited size of the channel, where charge inhomogeneity results from a significant charge penetration from the interfaces towards the center of the junction.

As an alternative to conventional transfer characteristics of FETs, the current is plotted as a function of $\tilde{n}_{0,WSe_2}$ in Fig.6.8(c). The effect of tensile strain is still present, with a modulation factor of about 10 for a deformation of 2%. As detailed previously, those results are valid in the sub-threshold regime. At large doping values (typically above 10^{13} cm^{-2}), WSe_2 becomes a degenerate semiconductor [297]. In this strong-inversion regime, the voltage induces substantial band bending in the insulating material, even for nanometers-thin insulators such as SiO_2 [294]. The current enters a saturation regime and I_{ds} exhibits an almost linear relationship with V_{gs}. From this discussion, one

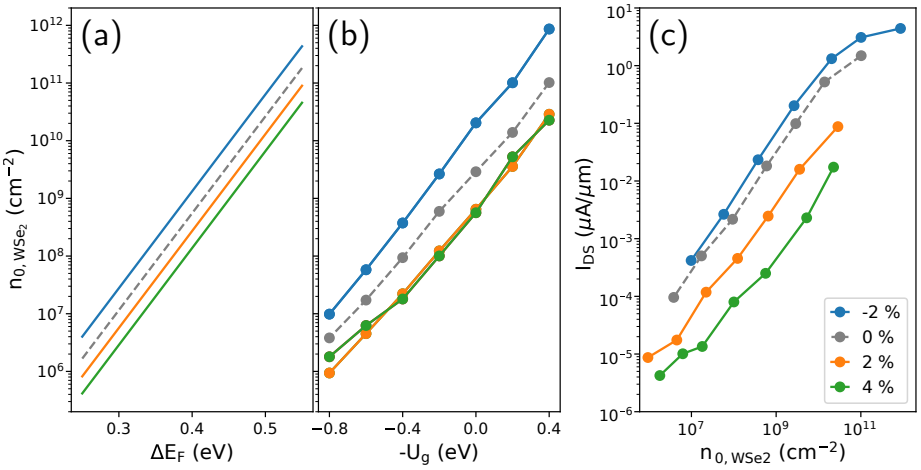

Figure 6.8: Transport properties and carrier statistics of a MoS_2-WSe_2 based FET. **(a,b)** Electron density in the channel ($\tilde{n}_{0,WSe_2}$) as a function of strain along the armchair direction, obtained for **(a)** an isolated 2D material and **(b)** in the center of a strip embedded in the junction. **(c)** Transfer characteristics for the device at $V_{ds} = 0.1$ V.

concludes that the plateau observed in Fig.6.8(c) does not correspond to the saturation regime. This is confirmed by numerical simulations performed at larger doping, where I_{ds} is observed to increase steadily until $\tilde{n} \approx 3 \times 10^{13}$ cm^{-2}. Although the description of the on-state is beyond the scope of this work, a value of 2×10^3 μA/μm is measured. This result is consistent with I_{on} obtained in n-type MoS_2 FETs [257–259], indicating the marginal impact of interfacial scattering on the current. As a last comment, the sub-threshold slope does not seem to be significantly affected by mechanical deformation. In order to provide a comprehensive explanation of the aforementioned results, the electronic properties of strained WSe_2 are thoroughly investigated and a simple theoretical model for lateral transmission is then proposed.

At first, the band structure of WSe_2 is compared at different strains with the energy bands obtained for the isolated configuration (see Fig.6.9). Note that when $\epsilon_x = 0$, the system is still strained along the interface direction due to the lattice correspondence between WSe_2 and MoS_2. Although the "unstrained" system is an indirect band gap semiconductor, WSe_2 recovers its direct band gap under moderate tensile strain ($\epsilon_x \geq 4\%$). This results is in agreement with the extensive theoretical work done by Maniadaki *et al.* [298]. It was demonstrated that uniaxial strain shifts the CBM to Q for $\epsilon_x < 0$ while the CBM

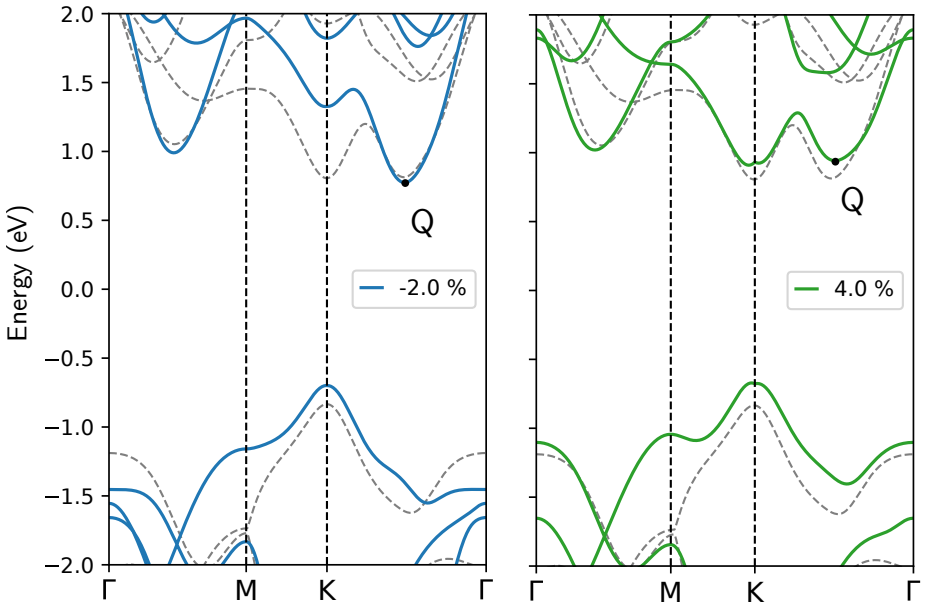

Figure 6.9: Electronic properties of WSe_2 strained along the armchair direction. The band structure of strained WSe_2 is compared to the one of isolated WSe_2, in solid colored lines and dashed gray lines, respectively. The Q point indicates the minimum of the conduction band.

and VBM remain at K otherwise. It follows that electronic transport exhibits a multi-band character when $\epsilon_x = 4\%$. Other theoretical works on TMDs have also predicted that strain changes the effective mass experienced by charge carriers at the Q and K points [160, 256, 257].

In the following, the dependence of E_g and m^* on mechanical deformation is investigated in detail. The description of the band gap is of the foremost importance as it controls band alignment, meaning that $\tilde{n}_{0,WSe_2}$ and the CBO are directly impacted by band gap modulations. In this context, the potential barrier at the MoS_2-WSe_2 interface (E_b) is provided for comparison. The results are presented in Fig.6.10.

Each parameter displays a proportional relationship to strain in the small deformation limit (i.e. $\epsilon_x < 5\%$). Interestingly, E_g and E_b appear to depend almost identically on strain. This strain-induced tuning of the band gap and the conduction band edge was already observed in WSe_2 contacted to metal electrodes [299]. In this three-terminal FET, the Schotty barrier at the conduction band edge decreases by the same amount as ΔE_g. The advantage of the current device is that WSe_2 is less perturbed by MoS_2 than by metal contacts due to the similar

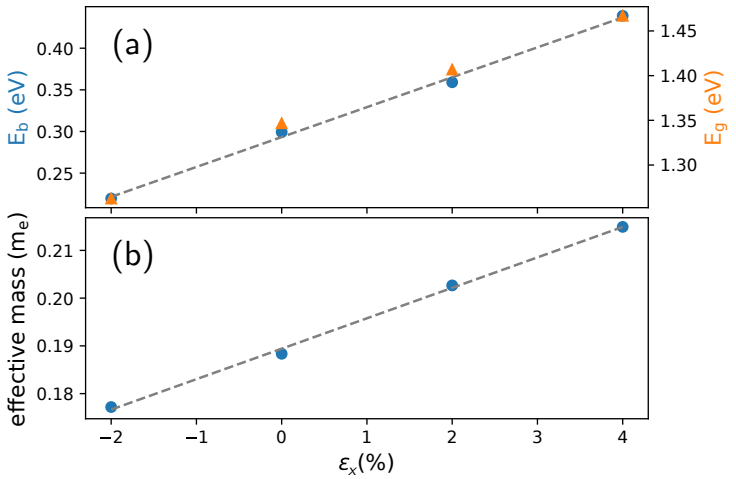

Figure 6.10: Electronic structure modifications of strained TMDs-based systems. **(a)** The energy barrier height (E_b) at the MoS_2-WSe_2 interface for $V_{ds} = 0.1$ V and $U_g = 0$ eV is compared with the band gap (E_g) in isolated strained WSe_2, depicted in blue and orange, respectively. **(b)** Effective mass computed at the Q point in isolated strained WSe_2.

chemical environments of both TMDs and to the much smaller charge density in MoS_2. The shorter perturbation means that MoS_2-WSe_2 lateral HSs represent a more scalable alternative for the miniaturization of electronic devices. Our estimation of m^* at Q is in satisfactory agreement with previous theoretical works [194, 300]. Importantly, the effective mass at Q was found to be anisotropic [257–259, 300], with an approximate two-fold ratio between the radial and tangential direction. Both components exhibit the same trend such that we investigate only the radial part. It turns out that for uniaxial strain: $0 < \partial m^*/\partial \epsilon$, similarly to biaxial strain in MoS_2 and WS_2 [257–259]. The impacts of variations in effective mass on the current are complex. Overall, a smaller effective mass is found to enhance the transfer characteristics of MX_2 FETs [301], mostly due to the increased group velocity. In the next paragraph, a simple theoretical model for lateral transport is proposed based on our analysis of E_b and m^*.

In FETs, the top gate controls exponentially the flow of electrons by affecting the carrier density in the channels. An equivalent approach is to consider the point of view of quantum tunneling. Electrons injected in MoS_2 are transmitted through the interface with a transmission probability that depends exponentially on the potential profile to overcome. As a first assumption, the potential shape is characterized only by the

width and height of the barrier. If the barrier is approximated by a rectangular potential, an incident wave is transmitted with probability

$$T(E) = 1/\left(\cosh^2(\beta w) + (\gamma/2)^2 \sinh^2(\beta w)\right) \tag{6.8}$$

where $\beta^2 = 2m^*(E_b - E)/\hbar^2$, $\gamma = \beta/k - k/\beta$ and w is the width of the barrier. In consistency with our previous discussions, this expression is derived for free particles populating a single parabolic band.

In Fig.6.11(a), the tunneling transmissions obtained with the analytical model are compared to conductance computed from first-principles, where w is determined such that it yields the more adequate fit. Interestingly, this simple approximation provides significant insight. On the one hand, a larger strain reduces exponentially $T(E)$ as E_b and m^* increase. On the other hand, the current is enlarged linearly by a greater DoS. The former effect is of course more consequential than the latter, translating into an exponential dependence of the current on strain, as depicted in Fig.6.7(a). The tunneling model also predicts the barrier width to decrease with the applied deformation. This observation is consistent with the LDoS presented in Fig.6.4(e,f). The potential shape changes from rectangular to triangular as strain increases, due to the aforementioned band bending effect, effectively reducing its width. The discrepancy between L_{WSe_2} and w is most probably due the simplicity of the model and to the assumption of an isotropic effective mass. Lastly, $T(E)$ deviates more from the model for larger deformation. The reason is that the CBM of WSe_2 exhibits a multi-bands character with increasing strain, causing the wave function in the device to show a mixed character due to the contributions of different valleys, e.g. from the K and Q valleys. This phenomena generates larger transmissions due to the underlying increase in DoS, as illustrated in Fig.6.11(a) for $\epsilon_x = 4\%$.

This latter comment requires a careful investigation of the role of each valley. In this regards, the current density and the map of transmission probabilities are depicted in Fig.6.11(b,c). The current density peaks around 1.1 eV due to the predominant contribution of the Q valley. The valley-dependence of the current is well represented in the transmission map, where both valleys fold at $\pi/3L_y$ while the Q valley also folds at $\pi/6L_y$. The role of the K valley is observed to remain marginal when comparing transmission maps at -2% and 4%, although its contribution becomes more and more significant as strain increases.

In the last section of this chapter, the dimensional scaling and the operational robustness of the device are investigated.

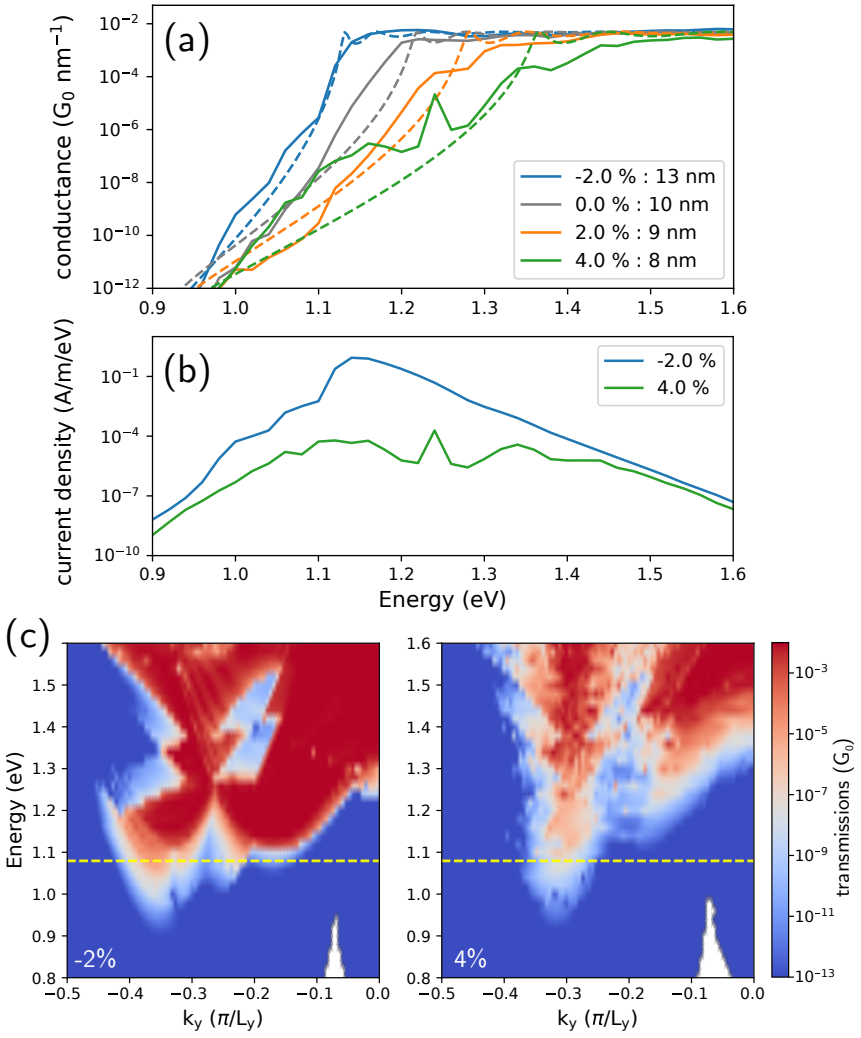

Figure 6.11: Quantum tunneling model for MoS_2-WSe_2 lateral junctions for different strain profiles at $V_{ds} = 0.1$ V and $U_g = 0$ eV. **(a)** Electronic transmission per unit area as a function of energy obtained from DFT and the quantum tunneling model for a rectangular barrier, represented in solid lines and dashed lines, respectively. The legend indicates the barrier width related to strain. **(b)** Current density as a function of energy. **(c)** Transmission probabilities (in logarithmic units) as a function of tranverse momentum (k_y) and energy. The yellow dashed line indicates the position of the Q point.

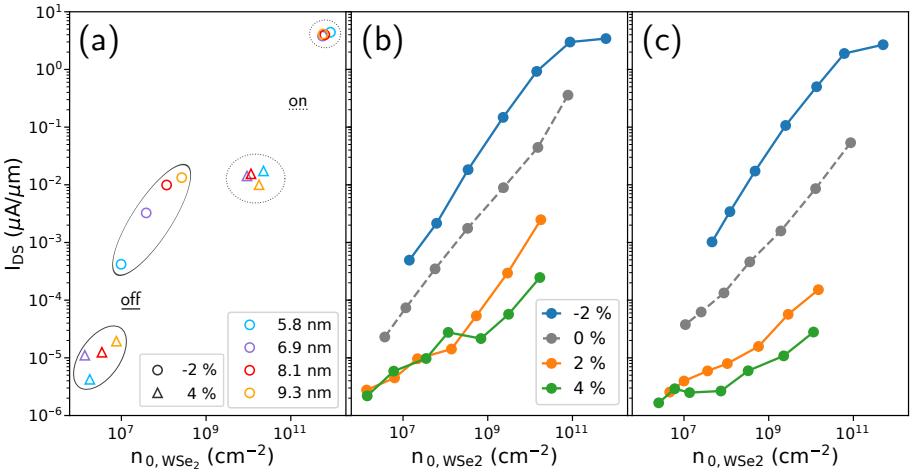

Figure 6.12: Transport properties of a MoS_2-WSe_2 based FET at various channel and gate lengths for $V_{ds} = 0.1$ V. **(a)** On and off currents, in dashed and solid circles, respectively, as L_g is increased while $L_{WSe_2} = 5.8$ nm. **(b,c)** Transfer characteristics for the device when the channel (gate) length is **(b)** 8.7 nm and **(c)** 11.6 nm.

At first, the region under electrostatic gating is extended beyond the WSe_2 channel such that the MoS_2 region at the interface is also affected by U_g. It was assumed until now that $L_{WSe_2} = L_g$, although it is evident that those two parameters would differ in practice. Such discrepancy could degrade the device performance or even impede its proper functioning. The on- and off-current values are reported in Fig.6.12(a) at tensile and compressive strains for L_g ranging from 5.8 nm to 9.3 nm while $L_{WSe_2} = 5.8$ nm. Owing to the restriction within the sub-threshold regime, the on-current values are defined as the largest values reported in Fig.6.8(c). A distinctive pattern emerges: I_{off} substantially increases with L_g whereas I_{on} is unaffected. The same observation applies to the sheet carrier density, meaning that extending the gate beyond the interface leads to an increased charge transfer from MoS_2 to WSe_2. This additional charge redistribution reduces the controllability of the gate on the current, impacting more strongly configurations with low $\tilde{n}_{0,WSe_2}$. Overall, the strain-induced modulation of the current is still preserved. The scaling behavior of the device is illustrated in Fig.6.12(b,c), with the channel extending over 8.7 nm and 11.6 nm. No significant effect is reported on the SS when L_g increases. This result is inconsistent with previous observations in the literature where the SS improves due to better electrostatic integrity as the device

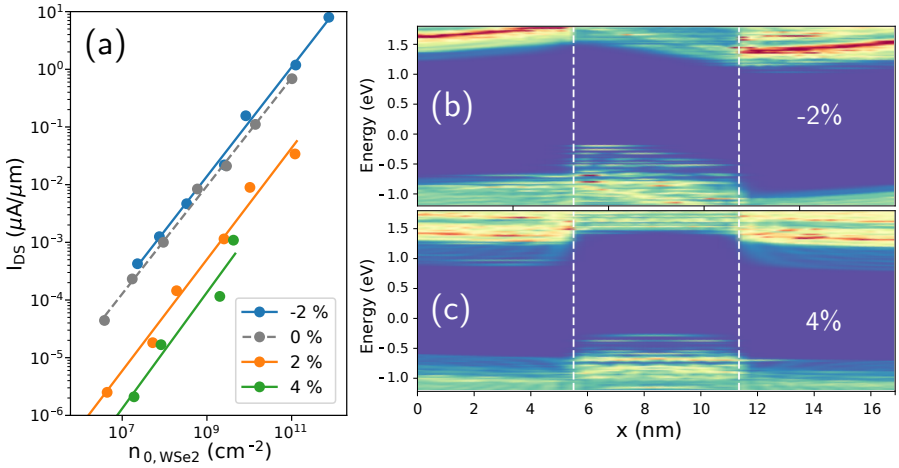

Figure 6.13: Transport properties of a uniformly strained MoS_2-WSe_2 based FET **(a)** Transfer characteristics for the device in the case of uniform uniaxial strain for $L_g = 5.8$ nm and $V_{ds} = 0.1$ V. The correpsonding LDoS at $U_g = 0$ eV at **(b)** $\epsilon_x = -2\%$ and **(c)** $\epsilon_x = 4\%$.

scales up [289, 302]. This discrepancy presumably originates from the technical limitation in the present device simulation. The current decreases for $\epsilon_x \geq 0\%$, illustrating an enhanced strain-controllabilty as tunneling probabilities drop for longer channels. Lastly, the density in the center of the channel appears reasonably independent of L_g, indicating the reliability of $\tilde{n}_{0,WSe_2}$ to characterize the carrier statistics in WSe_2.

Although strain engineering in WSe_2 is feasible at growth, the aforementioned strategies to introduce uniaxial deformation are not designed to impact the system locally but instead on the whole. Additionally, functional operation at global strain profiles represents a decisive advantage of hetereojunctions over TMDs mono-crystals, where strain-induced current modulation occurs only when deforming locally the central region. In this context, the $(I_{ds} - \tilde{n}_{0,WSe_2})$ characteristics are presented when the MoS_2 leads are strained uniaxially altogether with the WSe_2 channel. As strain affects the band gap in MoS_2, the Fermi level in the left lead is adjusted under the requirement that $\tilde{n}_{MoS_2} = 5 \times 10^{12}$ cm^{-2}. The results are depicted in Fig.6.13(a). A noticeable noise in currents is reported but the strain-controllabity remains overall acceptable, especially since the channel length is short. Indeed, the small L_{WSe_2} most probably causes the absence of current modulation for compressive strain. In the more practical case of tensile strain, this

feature is well preserved. Interestingly, the LDoS depicts a pronounced band bending for $\epsilon_x = -2\%$ while it is unapparent for $\epsilon_x = 4\%$, in contrast with the configuration of reference (see Fig.6.4(e-g)). This discrepancy assumingly originates from the change in electronic properties of MoS_2. The more triangular shape of the potential barrier also provides an explanation for the the absence of current modulation for tensile strain. As demonstrated by the quantum tunneling model, a triangular barrier is equivalent to a rectangular one with smaller width. At longer channel lengths, current modulation is expected for all strain profiles.

6.5 CONCLUSION

In summary, a MoS_2-WSe_2 lateral HS is studied by means of first-principles calculations. A type-II band alignment is reported, with band bending occurring at the junction vicinity for a zigzag interface due to charge redistribution effects. Strain is observed to significantly influence the band offset by increasing the band gap in the WSe_2 region. Afterwards, transport calculations are performed on the zigzag configuration in the collinear spin-unpolarized framework. Assuming a rigid shit of the band structure, the current characteristics are computed at $V_{ds} = 0.1$ V. A modulation of the current that depends exponentially on strain is reported. Strain-related effects consist of an adjustment of the CBO and the effective mass that is proportional to the applied deformation. As thermionic transport occurs by tunneling mechanisms, those phenomena imply an exponential dependence of I_{ds} on strain. This strong modulation contrasts with the moderate gain theoretically predicted in homogeneous MX_2 n-type FETs, where reasonable deformations ($< 5\%$) induce at most a 30% current increase [257–259]. The device operational robustness is demonstrated for global strain and non-ideal gating profiles while the current modulation is shown to improve when scaling up. In terms of quantum engineering [21], TMDs-based lateral HSs represent the scaling limit owing to their ultimate thinness and similar chemical environment, contrary to mixed-dimensional architectures [299, 303]. Compared to TMDs mono-crystals, the functional operation of the heterojunction even for global strain profiles constitutes a decisive advantage.

This theoretical work must be regarded as a preliminary step towards the demonstration of the unique platform that constitute lateral junctions of TMDs. Indeed, more elaborate studies are required to unveil

the full complexity of the underlying transport mechanisms and to overcome the present numerical limitations.

In this context, it is of importance to list some avenues and perspectives for forthcoming works. A fundamental improvement would be to introduce an insulating material between the top gate and the channel into the numerical simulations. In this manner, one could characterize the dependence on strain of the channel capacitance (C_q) due to modifications on the band structure. Similarly, the fringing of the electric field at the gate edge could also be included. Overall, the exact FET transfer characteristics could be calculated, enabling an accurate estimation of the SS factor and the on-state current. In the scope of low power electronics, one could consider the tunnel FET architecture owing to its improved sub-thermionic operation. It would also be of uttermost importance to compute the gauge factor of the device. In the context of straintronics, the large current modulation could provide an interesting platform for the highly sensitive measurement of strain or pressure. In this regard, strain gauges comparable to that of state of the art silicon sensors were already demonstrated using MoS_2 [304]. Another theoretical limitation is that electron-phonon interaction has been neglected although it has been predicted that the formation of chemical bonds at the interface would enhance the electron-phonon coupling [305]. From a structural perspective, the impact of defects has been neglected even though their presence at the interface has been observed experimentally [85]. In spite of their fundamental role in strain relaxation mechanisms, defects are not expected to substantially affect the performance of the device. Indeed, Cao *et al.* [306] demonstrated that optoelectronic properties such as the band offset are only minimally affected by interfacial imperfections. On the contrary, those defects could represent an interesting platform for the design of additional strain-induced transport mechanisms.

7 CONCLUSION

In this last chapter, the main results of the manuscript are put in perspective with recent findings of fundamental research, disruptive prospects for digital applications and expectations from the industry.

First and foremost, the emergence of 2DMs as a remarkable alternative to silicon-based technologies is nowadays obvious. Nano-material transistors offer considerable advantages, promoting transformative advancement towards high-performance thin-film applications [11]. Over the years, synthesis and post-processing techniques as well as the performance of devices have been experiencing continued extensive progress. In spite of the technological obstacles limiting all 2DMs-based electronics to a distant promise, the large scale chemical assembly of atomically thin circuits has been extensively demonstrated [23, 264]. Similarly, the integration of 2DMs into conventional devices is becoming a reality [307, 308]. In short, the development of 2DMs eventually constitutes an innovative strategy to supply the miniaturization trends in electronics foretold by Moore more than five decades ago.

7.1 POLYCRYSTALLINE GRAPHENE

As an important step towards industrial production of large scale high-quality flakes, the fast growth of inch-sized single-crystalline graphene was demonstrated on a Cu-Ni alloys in 2016 [309]. By locally feeding carbon precursors to a desired position, the synthesis period was reduced from roughly 12h down to 2.5h. Even more recently, Wang *et al.* [51] used a similar procedure to report the scalable growth of large-are single-crystal monolayer graphene that are high-quality and fold-free. Although those feats are impressive, relatively high growth temperatures ($\sim 1000^{\circ}$C) and the inevitable transfer step represent impediments for the industrial integration of graphene-based devices. The game-changing breakthroughs would be the development of graphene growth on arbitrary surfaces and/or at low temperatures (for example, using plasma-enhanced CVD or other methods) [205]. In this context, the direct integration of high-quality polycrystalline films on semiconducting devices has been realized at low temperatures [310, 311].

Our results support the feasibility of using well-stitched PG in electronic devices. The computed electronic transmissions show that graphene flakes formed by well-stitched grains can be almost comparable in quality to single-crystal containing impurities. For samples with large grains (typically beyond 10 μm), the sheet resistance will be dominated by scattering inside the grains [206]. Although GBs may not be significant scattering centers, the absorption of functional groups at line defects considerably degrades the performance of electronic devices [218]. The development of dry transfer methods compatible with industrial requirements represent another critical challenge for the integration of graphene-based devices. The objective for the industrial production of graphene-based applications is therefore to find an optimal trade-off between the grain size, the GB width, the growth time and temperature, depending on the application, while avoiding as much as possible chemical contamination. In this regard, Samsung and its collaborators reported almost a decade ago the realization of capacitive multitouch devices using mass-produced graphene films [312].

Beyond impeding charge transport, the presence of GBs can impact electronic devices in other ways. In the context of miniaturization, heat generation and dissipation is essential. However, Joule expansion microscopy measurements revealed strong Joule heating many times larger at the GBs than within the grains [313]. This bears important implications for the reliability of PG-based devices due to the substantial risk of premature failure before the average temperature has significantly increased. Additionally, GBs were shown to greatly enlarge electrical noise in transport measurements [314].

In complement to electronics, PG has also been considered for other type of applications. Several theoretical work investigated the role of GBs on the thermoelectric properties of graphene. Lehmann *et al.* [315] predicted the figure of merit to be significantly enhanced by the presence of GBs owing to a stronger phonon scattering. However, the combined predictions of atomistic simulations on the electrical [219] and thermal [316, 317] conductivity of large-area PG suggest an overall reduction of the figure of merit compared to single-crystal graphene. While the the adsorption and reaction of adsorbates or line defects can hinder electronic transport, it could be advantageous for gas sensing applications. Salehi *et al.* [318] showed that line defects offer superior performance as sensors compared to single-layer graphene containing point defects. Similarly, sensor-based technologies could exploit

the additional noise due to GBs that is undesired in most low noise applications [314].

7.2 THE CONTACT RESISTANCE

Several strategies are being proposed in order to reduce R_c: work function engineering [319], substitutional doping of graphene, optimizing the fabrication method [320] and the transfer process [321], cleaning the contacts by surface treatment [322–326], patterning the contact region [327, 328] or designing innovative device architectures [329]. Those different routes aim to lower R_c either by increasing the number of conducting modes in graphene or by enlarging interfacial interaction by improving chemical bonding or removing surface contaminants and resist residues. An optimal solution would however minimize electronic structure perturbations on the over-layered graphene. For example, a record value of 23 $\Omega\mu$m was obtained for R_c by combining edge contacts with the n-doping of graphene achieved by the negative transfer phenomenon at the interface with PVP/PMF insulators [330]. Scientists are also reaching a consensus on the applicability of standard measurement and extraction methods to obtain dependable and correct R_c values. After the demonstration that the classic transfer length method may be inappropriate under certain conditions for characterizing metal-graphene contacts [331, 332], clear protocols to extract R_c are now being defined [136].

Throughout our investigation, it was demonstrated that R_c depends on two principal contributions: the DoS of the metal and the efficiency of the orbital hybridization. The latter parameter was shown to be considerably sensitive to external perturbations for Ag, Au and Cu contacts. In addition, interfacial hybridization was reported to be significantly more efficient for vertical injection in the case of Au. This combination of factors indicates the potential of Au for good contacts. In this context, low R_c of 23 $\Omega\mu$m comparable to standards of silicon-based technology were obtained by patterning graphene before depositing Au contacts [328]. In this manner, interfacial coupling is increased by etching holes in graphene such that charge injection occurs through the edges at the expense of the surface.

The issue of the contact resistance is not limited to graphene contacts. In the case of semiconducting 2DMs, traditional strategies to decrease the Schottky barrier such as substitutional doping are too invasive to be applicable. Owing to the formation of metal-induced gap states

causing Fermi level pinning, the Schottky barrier can be considerably large. In addition, the problem related to the absence of bonding sites remains. In this context, the development of MX_2-based electronics is greatly hindered by the inability to obtain low values of R_c [56]. Most of the research on the contact resistance in TMDs has focused on MoS_2 due to its natural availability, restricting our understanding of these contacts due to their material-specific properties (such as constituent elements and atomic defects). In this regard, more systematic studies are required on other TMDs. In general, novel theoretical models and experimental approaches need to be developed to address the issue of the contact resistance in 2DMs. For example, a genuinely 2D approach to produce low R_c in TMDs is to phase-engineer a metallic 1T phase in the contact region of the semiconducting 2H phase [333].

7.3 2DMS-BASED HETEROSTRUCTURES

Over the past years, considerable progress has been made in material growth and device design of lateral HSs. The recent improvements in assembly techniques, characterization and spectroscopy methods have led to the synthesis of interfacial regions that are almost atomically sharp over tens of nanometers [85, 86]. This greatly contrasts with the diffusive nature of interfaces that existed in the preliminary growth stages of lateral HSs [265–267]. From the perspective of devices, some practical applications are already achieved in experiments while more and more theoretical proposals are being suggested, supplied by the increasing demand for novel materials platforms to develop next-generation technologies.

As central components in opto- and electronic devices, atomically thin in-plane p-n junctions can already be produced from lateral HSs of TMDs, owing to the chemical stability and structural similarity of their constituents. WSe_2–WS_2 junctions were shown to display high voltage gain when used as inverters [267] while well-defined diode characteristics with rectification ratios up to 10^5 were reported in another experiment [334]. MoS_2-WSe_2 lateral HSs demonstrated excellent power conversion efficiency in solar cells [335] and photodetectors with enhanced performance compared to isolated TMDs were realized with MoS_2-$MoSe_2$ junctions [336].

Theoretical proposals underline the considerable promises that hold TMDs-based heterojunctions, and field-effect devices are no exceptions. Transport studies have suggested that MoS_2-WS_2 ribbons show ex-

tremely high figure of merit if used as thermoelectric materials [337]. In an analogous manner, ferromagnetic MoS_2-WS_2 lateral junctions were proposed as spin-valley filters and splitters without external gating or as electron waveguide [338]. While strain has been predicted to enhance the power conversion efficiency of lateral HSs [339], the strain-induced current modulation detailed in Ch.6 represents a functionality that has not yet been predicted in those systems. Similarly, Lucchesi *et al.* [288] studied the properties of the MoS_2-WSe_2 lateral junction but within the scope of the bipolar transistor, showing large current modulation and strong current gain. In line with the phase engineering used to contact semiconducting TMDs [333], in-plane Schottky-barrier FETs based on 1T-2H lateral HSs were found to exhibit sub-threshold swing close to the thermionic limit [340]. Tunnel FETs based on 2H-TMDs heterojunctions are predicted to yield even lower sub-threshold, making them ideal candidate for ultra-low power consumption applications [289].

Those practical examples and theoretical proposals illustrate the evident interest of TMDs-based junctions due to their unique set of properties. Although all 2DMs-based electronics remains a distant prospect, lateral HSs already provide excellent complementary applications to those offered by conventional semiconductor technologies.

Overall, some essential challenges need to be overcome. In spite of the substantial developments in growth process, the junctions quality is still not comparable to their fundamental limit. Current synthesis methods do not yet yield reliable and repeatable products, as demanded by the industry. As slight changes in synthesis schemes may generate radically different structures, a deep understanding and a precise control over the kinetics and thermodynamics of the growth process are mandatory [84]. Hence, synthesis methods that are scalable and selective over crystals shape and dimension represent an important milestone. Similarly, theoretical efforts are needed to simulate interfaces as seen in experiments, by considering several features such as structural relaxation, dislocations, vacancies, impurities and strain fields. Atomistic models can be used to study systems containing thousands of atoms, random distributions of defects, large scale strains and other intrinsic attributes of lateral HSs. In this regard, TB models [114, 115, 291] and molecular dynamics methods [341, 342] offer a suitable trade-off between scaling and accuracy. Concerning electronic devices, the problem complexity requires a multi-scale approach to capture the detailed physics of the junction while providing a high-level description of the device operation [111].

Appendices

A

DENSITY FUNCTION THEORY

In the last decades, density functional theory (DFT) [96, 97] has emerged as a successful approach to compute the electronic structure of many-body systems such as molecules or crystalline solids. It is among the most popular and versatile methods currently used in computational physics and chemistry. Indeed, this method provides an accuracy comparable to traditional techniques such as Hartree-Fock while showing relatively low computational costs.

A.1 THE MANY-BODY PROBLEM

In quantum mechanics, the wave function (Ψ) contains all the information required to extract the physical properties of a system. Let us consider a crystalline solid composed of N_n nuclei and N_e electrons. In this configuration the wave function is expressed as

$$\Psi = \Psi(\vec{x}_1, ..., \vec{x}_{N_e}, \vec{R}_1, ..., \vec{R}_{N_n}) \tag{A.1}$$

where $\vec{x}_i$ and $\vec{R}_j$ are the coordinates of the nuclei and the electrons, respectively.

In the steady-state non-relativistic framework, the system dynamics is governed by the time-independent Schrödinger equation

$$\hat{H}\Psi = E\Psi \tag{A.2}$$

where $\vec{H}$ is the Hamiltonian of the system and E denotes the corresponding eigenvalues.

One can write this Hamiltonian in terms of two contribution, i.e. attraction/repulsion between particles by Coulomb interaction and the kinetic operators

$$\begin{aligned}\hat{H} = &-\frac{1}{2m_e}\sum_{i=1}^{N_e}\nabla_i^2 - \frac{1}{2M_n}\sum_{p=1}^{N_n}\nabla_p^2 \\ &-\sum_{i=1}^{N_e}\sum_{p=1}^{N_n}\frac{Z_p}{r_{ip}} + \sum_{i=1}^{N_e}\sum_{j>i}^{N_e}\frac{1}{r_{ij}} + \sum_{p=1}^{N_n}\sum_{q>p}^{N_n}\frac{Z_pZ_q}{R_{pq}}\end{aligned} \tag{A.3}$$

where Z is the total charge of an nucleus, m and M are electron and nucleus mass, $r_{i\alpha}$ is distance between electron i and a particle α and R_{pq} denotes the distance between nuclei p and q. The indices i, j and p, q denote electrons and nuclei respectively. The first two terms describe the kinetic energy of the electrons and nuclei. The other three terms represent the attractive electrostatic interaction between the nuclei and the electrons and repulsive potential due to the electron-electron and nucleus-nucleus interactions.

For clarity reasons, Eq.A.3 is written in a more compact form

$$\hat{H} = \hat{T}_e + \hat{T}_n + \hat{V}_{en} + \hat{V}_{ee} + \hat{V}_{nn} \tag{A.4}$$

Solving this Hamiltonian is however not numerically accessible due to the large number of components and the interacting terms that make it impossible to separate the many-body problem into simpler single-particle equations.

There are many sophisticated methods for solving Eq.A.4. For example, the wave function is expanded as a combination of Slater determinants in the Hartree–Fock method (and post-Hartree–Fock methods for more sophisticated approaches). These techniques are however extremely computationally demanding, making it virtually impossible to apply them efficiently to more complex systems. At contrary, DFT provides an appealing alternative by systematically mapping the many-body problem onto a single-body problem without interacting terms. In the following sections, the framework of DFT is covered in detail.

A.2 THE BORN-OPPENHEIMER APPROXIMATION

A preliminary observation is to notice that the nuclei are much heavier than electrons, since the mass of a proton is roughly 2000 times the one of an electron. This implies that the dynamics of the system can be decoupled between the electronic and the nucleic contributions

$$\Psi = \Psi_e(\vec{x}_1, ..., \vec{x}_{N_e})\Psi_n(\vec{R}_1, ..., \vec{R}_{N_n}) \tag{A.5}$$

where Ψ_e and Ψ_n are the electron and nuclei wave functions, respectively. As the change in electronic state occurs very rapidly compared to the nuclear motion, electrons are always in steady-state determined by the potential generated by the fixed nuclei. Within the Born-Oppenheimer approximation, one can completely separate the calcu-

lation of the electronic structure from that of the ionic motion. The many-body problem now reads

$$\hat{H}_e \Psi_e(\vec{x}_1, ..., \vec{x}_{N_e}) = E_e \Psi_e(\vec{x}_1, ..., \vec{x}_{N_e}) \tag{A.6}$$

with

$$\hat{H}_e = \hat{T}_e + \hat{V}_{en} + \hat{V}_{ee} \tag{A.7}$$

After determining the solutions of Eq.A.6, the nuclei positions are updated after solving

$$\hat{H}_n \Psi_n(\vec{R}_1, ..., \vec{R}_{N_n}) = E_n \Psi_n(\vec{R}_1, ..., \vec{R}_{N_n}) \tag{A.8}$$

where

$$\hat{H}_n = \hat{T}_n + \hat{V}_{en} + \hat{V}_{nn} \tag{A.9}$$

This approximation is the basis of the usual *ab initio* molecular-dynamics methods.

A.3 THE HOHENBERG-KOHN THEOREMS

At this stage, the electronic problem is still intractable due to the massive size of Ψ_e and to the many-body interacting terms in $\hat{H}_e$. A practical approach to overcome those issues would be to express the interacting part as a effective one-particle potential.

$$V_{ee} \approx \sum_i V^{eff}(\vec{x}_i) \tag{A.10}$$

In this configuration, the many-body wave function can be decoupled between N_e one-particle wave functions

$$\Psi_e(\vec{x}_1, ..., \vec{x}_{N_e}) = \psi_1(\vec{x_1}) \dots \psi_{N_e}(\vec{x_{N_e}}) \tag{A.11}$$

which makes the many-body problem tractable.

In this context, DFT expresses the interacting term as a mean-field potential that depends on the density. The exactness of this approach is based on two theorems demonstrated by Hohenberg and Kohn [96]

The first theorem shows that the external potential ($\hat{V}_{en}$) is a functional of the electron density ($\rho(\vec{x})$). The corollary is that all quantities

that may be know once the potential is fixed are also functional of $\rho(\vec{x})$. Naturally, the total energy is also a functional of the density

$$\begin{aligned} E[\rho] &= T_e[\rho] + E_{en}[\rho] + E_{ee}[\rho] \\ &= T_e[\rho] + \int \rho(\vec{r})\hat{V}_{en}(\vec{r})d\vec{r} + E_{ee}[\rho] \\ &= F[\rho] + \int \rho(\vec{r})\hat{V}_{en}(\vec{r})d\vec{r} \end{aligned} \tag{A.12}$$

where $F[\rho]$ is a universal functional of the electron density that is *a priori* not known explicitly.

The second theorem states that the ground-state energy can be obtained variationally, with the density that minimizes the total energy being the exact ground-state density. This result is expressed using the variational principle as

$$\begin{aligned} E_0 = E[\tilde{\rho}_0] \leq E[\rho] = T_e[\rho] + E_{en}[\rho] + E_{ee}[\rho] \\ \text{under the conditions that: } \int \rho(\vec{r})d\vec{r} = N_e \end{aligned} \tag{A.13}$$

where $\tilde{\rho}_0$ is the exact ground-state density.

The consequence of those theorems is that the determination of the many-body wave function can be achieved by computing variationally the ground-state density, simplifying tremendously the complexity of the many-body problem.

A.4 THE KOHN-SHAM EQUATIONS

Although the Hohenberg-Kohn theorems are extremely powerful, they do not indicate how to practically compute the ground-state density of a system. About one year after the seminal paper of Hohenberg and Kohn [96], Kohn and Sham proposed a simple method to carry-out DFT calculations [97].

The Kohn-Sham formulation is based on the mapping of the full interacting system with the real potential, onto a fictitious non-interacting system where electrons are moving within an effective "Kohn-Sham" single-particle potential (V_{KS}). The Kohn-Sham method is still exact since it yields the same ground-state density as the real system, but greatly facilitates the calculation.

In order to obtain the Kohn-Sham form of the Schrodinger expression, $F[\rho]$ is partitioned into three terms, the first two of which are known

exactly and constitute the majority of the energy, the third being a small unknown quantity

$$F[\rho] = T_s[\rho] + E_H[\rho] + E_{xc}[\rho] \tag{A.14}$$

In this process, the kinetic energy of the real interacting system is replaced by

$$T_s = -\frac{1}{2m_e}\sum_{i=1}^{N_e}\langle\Phi_i|\nabla_i^2|\Phi_i\rangle \tag{A.15}$$

where the Φ_i are the orbitals of the non-interacting system. The classical electron-electron interaction term is expressed by the Hartree potential

$$E_H = \frac{1}{2}\int\int\frac{\rho(\vec{r}_1)\rho(\vec{r}_2)}{|\vec{r}_1-\vec{r}_2|}d\vec{r}_1 d\vec{r}_2 \tag{A.16}$$

The third term is denoted as the exchange-correlation energy (E_{xc}). It represents the difference between the exact and non-interacting kinetic energies and accounts for non-classical contribution to the electron-electron interactions, such as the self-interaction correction or the exchange interaction. A formal definition of the exchange-correlation functional is

$$E_{xc}[\rho] = (T_e[\rho] - T_s[\rho]) + (E_{ee}[\rho] - E_H[\rho]) \tag{A.17}$$

which contains every information that is unknown.

The variational principle (see Eq.A.13) now turns into minimizing the functional

$$E[\rho] = T_s[\rho] + \int\rho(\vec{r})\hat{V}_{en}(\vec{r})d\vec{r} + E_H[\rho] + E_{xc}[\rho] \tag{A.18}$$

under the constraint of a fixed number of electrons

$$\int\rho(r)dr = N_e \tag{A.19}$$

This many-problem of N_e interacting electrons is now strictly equivalent to that of a system of non-interacting electrons with the same electronic density in an external potential, called Kohn-Sham potential

$$\hat{V}_{KS}(\vec{r}) = \hat{V}_{en}(\vec{r}) + \int\frac{\rho(\vec{r})}{|\vec{r}-\vec{r}_1|}d\vec{r}_1 + E_{ee}[\rho] + \frac{\partial E_{xc}[\rho]}{\partial\rho(\vec{r})} \tag{A.20}$$

where the second term is the Hartree potential and the last term is the exchange-correlation potential $\hat{V}_{xc}(\vec{r})$.

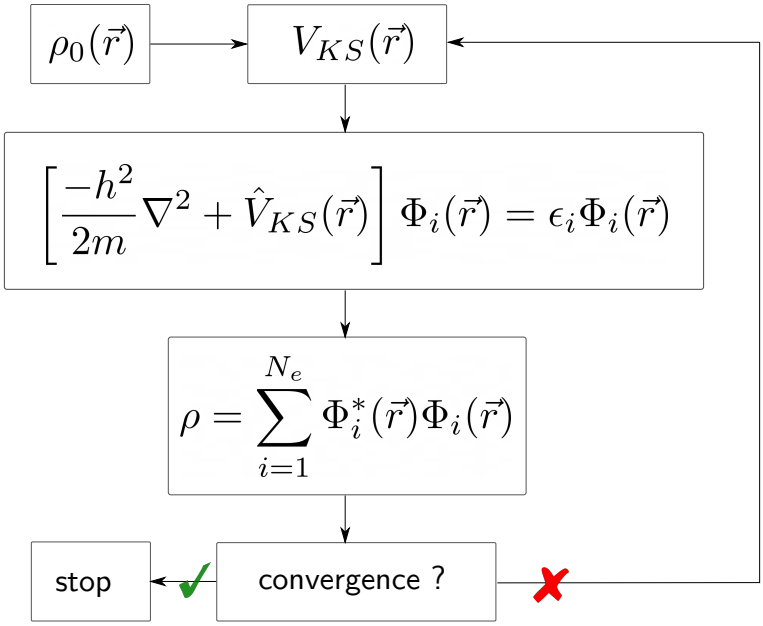

Figure A.1: Kohn-Sham algorithm for convergence. A initial guess for the Kohn-Sham potential (V_{KS}) is done based on a initial density $\rho_0(\vec{r})$. The single-electron Schrodinger equation is then solved in order to obtain the Kohn-Sham orbitals (Φ_i). The electronic density is updated by using the newly-computed Φ_i. A next iteration cycle is performed with the updated density until convergence is reached.

Similarly, calculating the electronic structure by solving Eq.A.6 is equivalent to solve self-consistently the single-electron Schrodinger equation (also called Kohn-Sham equation)

$$\left[\frac{-h^2}{2m}\nabla^2 + \hat{V}_{KS}(\vec{r})\right]\Phi_i(\vec{r}) = \epsilon_i\Phi_i(\vec{r}) \tag{A.21}$$

where the Φ_i are called the Kohn-Sham orbitals for obvious reasons. Note that eigenvalues (ϵ_i) do not correspond to the true eigenvalues of the interacting system.

From the one-electron wavefunction, one can define the electronic density

$$\rho = \sum_{i=1}^{N_e} \Phi_i^*(\vec{r})\Phi_i(\vec{r}) \tag{A.22}$$

Assuming that the exchange-correlation functional V_{Ks} is known, the many-body problem can be solved by the variational principle. The solution of the non-interacting electrons moving in the Kohn-Sham

potential is a Slater determinant constructed from the single-electron wave function that are solution to Eq.A.21. Once the Kohn-Sham eigenfunctions (Φ_i) are computed, the electron density is obtained by Eq.A.22. Owing to the dependence of V_{Ks} on the electron density, the problem has to be solved self-consistently, as illustrated in Fig.A.1. An initial guess ρ_0 is selected and the solution is iteratively improved by the self-consistent scheme. The procedure is stopped once the tolerance criterion on the electron density is reached.

The equivalence between the converged density and the one corresponding to the many-body problem is ensured by the Hohenberg-Kohn theorems.

A.5 THE EXCHANGE-CORRELATION FUNCTIONALS

The principal difficulty in the framework of DFT is to determine V_{xc}, since the exact form of the exchange-correlation is not known. From Euler relation, V_{xc} is derived as

$$V_{xc} = \frac{\partial E_{xc}[\rho(\vec{r})]}{\partial \rho(\vec{r})} \tag{A.23}$$

The corresponding functional is expressed as

$$E_{xc} = \int \rho(\vec{r}) \epsilon_{xc}(\vec{r}, \rho) d\vec{r} \tag{A.24}$$

where $\epsilon_{xc}(\vec{r}, \rho)$ is the local exchange-correlation per electron. While some properties of this energy density are known, its exact formulation is not. Some approximations are therefore required in order to estimate the form of $\epsilon_{xc}(\vec{r}, \rho)$.

The local-density approximation

The simplest functional for the exchange-correlation term is the local density approximation (LDA), where the value of $\epsilon_{xc}(\vec{r}, \rho)$ is assumed to depends solely on the local electronic density. In addition, $\rho(\vec{r})$ is modeled as in the case of an homogeneous electron gas. This approach was initially proposed in the seminal paper of Kohn and Sham [97]

$$E_{xc}^{LDA}[\rho(\vec{r})] = \int \rho(\vec{r}) \epsilon_{xc}^{hom}[\rho(\vec{r})] d\vec{r} \tag{A.25}$$

The exchange part of $\epsilon_{xc}^{hom}[\rho(\vec{r})]$ is analytically tractable while its correlation part can be computed numerically. The LDA functional provides

an accurate description of the atomic structure and the vibrational properties of most systems. However, the strong approximation of locality creates an overestimation of the binding energy in molecules and solid crystals.

The generalized gradient approximation

An natural improvement of the LDA method is to consider the dependence of ϵ_{xc} on the gradient of the density. This extension leads to the generalized gradient approximation (GGA) [343]

$$E_{xc}^{GGA}[\rho(\vec{r})] = \int \rho(\vec{r})\epsilon_{xc}[\rho(\vec{r}), \nabla\rho(\vec{r})]d\vec{r} \tag{A.26}$$

The GGA functional has brought significant improvements compared to the simpler LDA, for example in the description of energy barriers or binding energies. In this regard, it is important to point out that GGA provides a limited accuracy of roughly 50 meV/atom for the estimation of binding energies [344]. A noticeable failure of GGA is that long-range interactions such as vdW dispersion forces are overlooked [150]. However, semi-empirical corrections such as the ones implemented by Grimme *et al.* [150] allow to account for those interactions at low computational cost. Most of the results presented in this thesis were obtained using this functional.

Although both LDA and GGA tend to give a sufficient description of the electronic properties, other higher-order formalisms such as the GW method or hybrid functionals may be needed if a more stringent accuracy is required.

B

SEMI-EMPIRICAL TRANSPORT MODELS

B.1 THE WENTZEL-KRAMERS-BRILLOUIN APPROXIMATION

The Wentzel-Kramers-Brillouin (WKB) approximation is a technique for finding approximate solutions to linear differential equations, such as the time-independent Schrödinger equation in one dimension

$$\frac{d^2\psi}{dx^2} + \frac{2m}{\hbar^2}\left(E - U(x)\right)\psi = 0 \tag{B.1}$$

where $U(x)$ represents the potential energy term. If this term is not expressed in a simple form, the one-dimensional Schrödinger equation does not have an analytical solution. The WKB method yields an approximate solution represented as a modulated constant-potential wave function when $U(x)$ is assumed to vary slowly along the x-axis. This technique is typically used to characterize tunneling through a potential barrier such as in the case of scanning tunneling microscopy [202].

Definition of τ

Here we derive the expression of the decay length for charge carriers tunneling through a 1D potential barrier based on the WKB approximation. Those charge carriers are injected in a left electrode and collected in a right electrode.

Let us consider a potential barrier defined over a given distance along the transport direction

$$U(x) = \begin{cases} f(x) \text{ if } 0 \leq x \leq \Delta x \\ 0 \text{ elsewhere} \end{cases} \tag{B.2}$$

Here, the first and the second regions typically correspond to the vacuum region and the electrodes, respectively.

Let us first assume that $f(x) = U_0$. For this simplest case, the solution to the Schrödinger equation reads

$$\psi(x) = e^{ik_x x}/\sqrt{L} \tag{B.3}$$

where k_x is the momentum of the incoming wave and L is a normalization factor related to the length of the electrode. Inside the barrier, $\psi(x)$ can be written in a slightly different way that accounts for reflection and transmission at the potential interface

$$\psi(x) = te^{-\tau x}/\sqrt{L} \tag{B.4}$$

where t denotes the tunneling probability of the incoming wave and τ represents the decay length. If one considers particles whose energy lies in the classically forbidden region, the decay length has the form

$$\tau = \sqrt{\frac{2m\Phi}{\hbar^2}} \tag{B.5}$$

where $\Phi = U_0 - E_F$ is the barrier height experienced by the charge carrier whose energy is given E_F. This definition of τ satisfies Schrodinger equation for a eigenvector defined by Eq.B.4.

The previous results can easily be extended to the more general situation where the particle is a plane wave with non-zero momentum in the $\{k_y, k_z\}$ directions. In this case, the condition for the classically forbidden region becomes

$$\left(E_F - \frac{\hbar^2 k_{\mathbf{r}}^2}{2m}\right) < U_0 \tag{B.6}$$

and the decay length is

$$\tau = \sqrt{\frac{2m\Phi}{\hbar^2} + k_{\mathbf{r}}^2} \tag{B.7}$$

where $k_{\mathbf{r}}^2 = k_y^2 + k_z^2$.

Let us now assume that the potential varies only slowly along the x-axis. In this case, the eigenvectors should ressemble closely Eq.B.4. Consider the following solution

$$\psi(x) = te^{iu(x)}/\sqrt{L} \tag{B.8}$$

except that the function $u(x)$ is not anymore linear in x. Substituting $\psi(x)$ into Schrodinger equation gives us the relation

$$i\frac{d^2u}{dx^2} - \left(\frac{du}{dx}\right)^2 + k^2(x) = 0 \tag{B.9}$$

where

$$\hbar k(x) = \begin{cases} \sqrt{2m\left(E - U(x)\right)} \text{ if } E > U(x) \\ i\sqrt{2m\left(U(x) - E\right)} \text{ if } E < U(x) \end{cases} \tag{B.10}$$

has been introduced for the sake of clarity. Although Eq.B.9 is totally equivalent to Schrodinger equation, it might seem that little was gained, especially since the former equation is non linear. However, this last relation enables us to derive a simple approximation for $u(x)$ through an iterative procedure. Indeed, we know that $u''(x)$ is zero in the case of a free particle. Assumingly, this term would also remain small for a slowly varying potential $U(x)$. Assuming $u''(x) = 0$ in Eq.B.2 yields the zeroth order approximation

$$u_0(x) = \pm \int k(x)dx + C_0 \tag{B.11}$$

where C_0 is an constant. It is evident that for a constant potential, $u_0(x)$ gives Eq.B.4 for $\psi(x)$. An iterative procedure is then constructed by writing Eq.B.9 as

$$u^2(x) = k^2(x) + iu''(x) \tag{B.12}$$

This gives the iterative relation

$$u_{n+1}(x) = \pm \int \sqrt{k^2(x) + iu_n''(x)}\; dx + C_{n+1} \tag{B.13}$$

At the first order, $u_1(x)$ reads

$$u_1(x) = \pm \int \sqrt{k^2(x) \pm ik'(x)}\; dx + C_1 \tag{B.14}$$

Each sign is related to a particular solution of Eq.B.9. A general expression for $\psi(x)$ is formed by considering a superposition of those two solutions. As $u_1(x)$ is supposedly a small correction to u_0, $u(x)$ converges to the correct value if

$$|k'(x)| \ll |k^2(x)| \tag{B.15}$$

which is a central assumption of the WKB approximation. This convergence criterion is actually the original formulation of Eq.4.25. On those assumptions, the eigenvectors read

$$\psi(x) = \frac{t}{\sqrt{L\, k(x)}} \exp\left[\pm i \int k(x)dx\right] \tag{B.16}$$

after expanding Eq.B.14 under the condition of Eq.B.15

$$\begin{aligned} u_1(x) &= \int \left[\pm k(x) + \frac{i}{2} \frac{k'(x)}{k(x)} \right] dx \\ &= \pm \int k(x) dx + i/2 \ \ln k(x) \end{aligned} \tag{B.17}$$

where the renormalization factor related to C_1 is neglected.

B.2 TRANSPORT MODEL IN METAL-GRAPHENE JUNCTIONS

In this section, we provide a formal definition of the decay length κ introduced in the transport model in Sec.4.5.

Definition of κ

Let us consider the ratio between transmissions at distances d and $d + \delta d$ for any given energy. It follows from Eq.4.16 that the transmission ratio is expressed within our empirical transport model as

$$\frac{T(d + \delta d)}{T(d)} = \frac{\exp\left[-\kappa(d + \delta d - d_{eq})\right]}{\exp\left[-\kappa(d - d_{eq})\right]} \tag{B.18}$$

where κ measures the sensitivity of transport to small modifications in chemical bonding. This parameter depends as well on the distance (d) due to the intrinsic non-linear nature of chemical interactions. That is to say that bonding saturates at small separations while the interaction vanish exponentially with increasing metal-graphene distance. In that latter case, charge carriers are transferred through the graphene systems by hopping. We have assumed here that κ is identical for both separations as δd represents only a tiny variation in the bonding length. As transmissions are by definition probabilities, the following relation holds true

$$-\kappa = \frac{\log\left[T(d + \delta d)\right] - \log\left[T(d)\right]}{\delta d} \tag{B.19}$$

In the infinitesimal limit, the previous equation is expressed as

$$-\kappa = \frac{\partial \log(T)}{\partial d} \tag{B.20}$$

which corresponds to the logarithmic rate of change of the tunneling probabilities.

BIBLIOGRAPHY

[1] G. E. Moore *et al.*, Cramming more components onto integrated circuits (1965).

[2] S. I. Association, Market data, `semiconductors.org/data-resources/market-data/` (16th November 2021).

[3] O. W. in Data, Technological progress, `shttps://ourworldindata.org/technological-progress` (16th November 2021).

[4] R. H. Dennard, F. H. Gaensslen, H.-N. Yu, V. L. Rideovt, E. Bassous, and A. R. Leblanc, IEEE Solid-State Circuits Society Newsletter **12**, 38 (2007).

[5] M. M. Waldrop, Nature News **530**, 144 (2016).

[6] D. J. Frank, IBM Journal of Research and Development **46**, 235 (2002).

[7] S. Zeng, Z. Tang, C. Liu, and P. Zhou, Nano Research **14**, 1752 (2021).

[8] J.-P. Colinge *et al.*, *FinFETs and other multi-gate transistors*, Vol. 73 (Springer, 2008).

[9] X. Huang, W.-C. Lee, C. Kuo, D. Hisamoto, L. Chang, J. Kedzierski, E. Anderson, H. Takeuchi, Y.-K. Choi, K. Asano, *et al.*, in *International Electron Devices Meeting 1999. Technical Digest (Cat. No. 99CH36318)* (IEEE, 1999) pp. 67–70.

[10] B. Yu, Y. Tung, S. Tang, E. Hui, T. King, and C. Hu, in *Proc. Int. Semiconductor Device Research Symp* (1997) pp. 623–626.

[11] A. D. Franklin, Science **349** (2015).

[12] J. A. Del Alamo, Nature **479**, 317 (2011).

[13] A. R. Brill, E. Koren, and G. de Ruiter, Journal of Materials Chemistry C (2021).

[14] M. Chhowalla, D. Jena, and H. Zhang, Nature Reviews Materials **1**, 1 (2016).

[15] A. Castellanos-Gomez, Nature Photonics **10**, 202 (2016).

[16] D. Akinwande, C. Huyghebaert, C.-H. Wang, M. I. Serna, S. Goossens, L.-J. Li, H.-S. P. Wong, and F. H. Koppens, Nature **573**, 507 (2019).

[17] A. Gupta, T. Sakthivel, and S. Seal, Progress in Materials Science **73**, 44 (2015).

[18] K. S. Novoselov, A. K. Geim, S. Morozov, D. Jiang, Y. Zhang, S. Dubonos, , I. Grigorieva, and A. Firsov, Science **306**, 666 (2004).

[19] K. S. Kim, Y. Zhao, H. Jang, S. Y. Lee, J. M. Kim, K. S. Kim, J.-H. Ahn, P. Kim, J.-Y. Choi, and B. H. Hong, Nature **457**, 706 (2009).

[20] G. Fiori, F. Bonaccorso, G. Iannaccone, T. Palacios, D. Neumaier, A. Seabaugh, S. K. Banerjee, and L. Colombo, Nature Nanotechnology **9**, 768 (2014).

[21] G. Iannaccone, F. Bonaccorso, L. Colombo, and G. Fiori, Nature Nanotechnology **13**, 183 (2018).

[22] V. K. Sangwanand M. C. Hersam, Annual Review of Physical Chemistry **69**, 299 (2018).

[23] M. Zhao, Y. Ye, Y. Han, Y. Xia, H. Zhu, S. Wang, Y. Wang, D. A. Muller, and X. Zhang, Nature Nanotechnology **11**, 954 (2016).

[24] A. C. Neto, F. Guinea, N. Peres, K. S. Novoselov, and A. K. Geim, Reviews of Modern Physics **81**, 109 (2009).

[25] K. S. Novoselov, A. K. Geim, S. V. Morozov, D. Jiang, M. I. Katsnelson, I. Grigorieva, S. Dubonos, Firsov, and AA, Nature **438**, 197 (2005).

[26] K. S. Novoselov, Z. Jiang, Y. Zhang, S. Morozov, H. Stormer, U. Zeitler, J. Maan, G. Boebinger, P. Kim, and A. Geim, Science **315**, 1379 (2007).

[27] M. Katsnelson, K. Novoselov, and A. Geim, Nature Physics **2**, 620 (2006).

[28] M. Katsnelson, The European Physical Journal B-Condensed Matter and Complex Systems **51**, 157 (2006).

[29] V. V. Cheianov, V. Fal'ko, and B. Altshuler, Science **315**, 1252 (2007).

[30] J.-H. Chen, C. Jang, S. Xiao, M. Ishigami, and M. S. Fuhrer, Nature Nanotechnology **3**, 206 (2008).

[31] M.-Q. Long, L. Tang, D. Wang, L. Wang, and Z. Shuai, Journal of the American Chemical Society **131**, 17728 (2009).

[32] K. I. Bolotin, K. J. Sikes, Z. Jiang, M. Klima, G. Fudenberg, J. Hone, P. Kim, and H. Stormer, Solid State Communications **146**, 351 (2008).

[33] C. R. Dean, A. F. Young, I. Meric, C. Lee, L. Wang, S. Sorgenfrei, K. Watanabe, T. Taniguchi, P. Kim, K. L. Shepard, *et al.*, Nature Nanotechnology **5**, 722 (2010).

[34] F. Schedin, A. K. Geim, S. V. Morozov, E. Hill, P. Blake, M. Katsnelson, and K. S. Novoselov, Nature Materials **6**, 652 (2007).

[35] F. Xia, T. Mueller, Y.-m. Lin, A. Valdes-Garcia, and P. Avouris, Nature Nanotechnology **4**, 839 (2009).

[36] X. Li, H. Zhu, K. Wang, A. Cao, J. Wei, C. Li, Y. Jia, Z. Li, X. Li, and D. Wu, Advanced Materials **22**, 2743 (2010).

[37] F. Schwierz, Nature Nanotechnology **5**, 487 (2010).

[38] S. Bae, H. Kim, Y. Lee, X. Xu, J.-S. Park, Y. Zheng, J. Balakrishnan, T. Lei, H. R. Kim, Y. I. Song, *et al.*, Nature Nanotechnology **5**, 574 (2010).

[39] G. Eda, G. Fanchini, and M. Chhowalla, Nature Nanotechnology **3**, 270 (2008).

[40] J. S. Bunch, A. M. Van Der Zande, S. S. Verbridge, I. W. Frank, D. M. Tanenbaum, J. M. Parpia, H. G. Craighead, and P. L. McEuen, Science **315**, 490 (2007).

[41] C. Chen, S. Lee, V. V. Deshpande, G.-H. Lee, M. Lekas, K. Shepard, and J. Hone, Nature Nanotechnology **8**, 923 (2013).

[42] R. Murali, K. Brenner, Y. Yang, T. Beck, and J. D. Meindl, IEEE Electron Device Letters **30**, 611 (2009).

[43] A. Rycerz, J. Tworzydlo, and C. Beenakker, Nature Physics **3**, 172 (2007).

[44] D. Xiao, W. Yao, and Q. Niu, Physical Review Letters **99**, 236809 (2007).

[45] J. Williams, T. Low, M. Lundstrom, and C. Marcus, Nature Nanotechnology **6**, 222 (2011).

[46] P. Rickhaus, R. Maurand, M.-H. Liu, M. Weiss, K. Richter, and C. Schönenberger, Nature Communications **4**, 1 (2013).

[47] T. E. Commission, The graphene flagship, `graphene-flagship.eu` (16th November 2021).

[48] M. H. Gass, U. Bangert, A. L. Bleloch, P. Wang, R. R. Nair, and A. Geim, Nature Nanotechnology **3**, 676 (2008).

[49] F. Banhart, J. Kotakoski, and A. V. Krasheninnikov, ACS Nano **5**, 26 (2010).

[50] P. Y. Huang, C. S. Ruiz-Vargas, A. M. van der Zande, W. S. Whitney, M. P. Levendorf, J. W. Kevek, S. Garg, J. S. Alden, C. J. Hustedt, Y. Zhu, *et al.*, Nature **469**, 389 (2011).

[51] M. Wang, M. Huang, D. Luo, Y. Li, M. Choe, W. K. Seong, M. Kim, S. Jin, M. Wang, S. Chatterjee, *et al.*, Nature **596**, 519 (2021).

[52] O. V. Yazyev and Y. P. Chen, Nature Nanotechnology **9**, 755 (2014).

[53] V. H. Nguyen, S. Dechamps, P. Dollfus, and J.-C. Charlier, Physical Review Letters **117**, 247702 (2016).

[54] D. Gunlycke and C. T. White, Physical Review Letters **106**, 136806 (2011).

[55] V. Dal Lago and L. F. Torres, Journal of Physics: Condensed Matter **27**, 145303 (2015).

[56] A. Allain, J. Kang, K. Banerjee, and A. Kis, Nature Materials **14**, 1195 (2015).

[57] D. S. Schulman, A. J. Arnold, and S. Das, Chemical Society Reviews **47**, 3037 (2018).

[58] A. Giubileo, Filippo and Di Bartolomeo, Progress in Surface Science **92**, 143 (2017).

[59] S. Manzeli, D. Ovchinnikov, D. Pasquier, O. V. Yazyev, and A. Kis, Nature Reviews Materials **2**, 1 (2017).

[60] J. A. Wilson, F. Di Salvo, and S. Mahajan, Advances in Physics **24**, 117 (1975).

[61] W. Shi, J. Ye, Y. Zhang, R. Suzuki, M. Yoshida, J. Miyazaki, N. Inoue, Y. Saito, and Y. Iwasa, Scientific Reports **5**, 1 (2015).

[62] B. Sipos, A. F. Kusmartseva, A. Akrap, H. Berger, L. Forró, and E. Tutiš, Nature Materials **7**, 960 (2008).

[63] A. Splendiani, L. Sun, Y. Zhang, T. Li, J. Kim, C.-Y. Chim, G. Galli, and F. Wang, Nano Letters **10**, 1271 (2010).

[64] L. Xie, Nanoscale **7**, 18392 (2015).

[65] P. Johari and V. B. Shenoy, ACS Nano **6**, 5449 (2012).

[66] Y. Liu, Y. Gao, S. Zhang, J. He, J. Yu, and Z. Liu, Nano Research **12**, 2695 (2019).

[67] L. Britnell, R. M. Ribeiro, A. Eckmann, R. Jalil, B. D. Belle, A. Mishchenko, Y.-J. Kim, R. V. Gorbachev, T. Georgiou, S. V. Morozov, *et al.*, Science **340**, 1311 (2013).

[68] A. Ramasubramaniam, Physical Review B **86**, 115409 (2012).

[69] K. F. Mak, K. He, C. Lee, G. H. Lee, J. Hone, T. F. Heinz, and J. Shan, Nature Materials **12**, 207 (2013).

[70] A. K. A. Lu, G. Pourtois, M. Luisier, I. P. Radu, and M. Houssa, Journal of Applied Physics **121**, 044505 (2017).

[71] T. Agarwal, D. Yakimets, P. Raghavan, I. Radu, A. Thean, M. Heyns, and W. Dehaene, IEEE Transactions on Electron Devices **62**, 4051 (2015).

[72] F. Schwierz, J. Pezoldt, and R. Granzner, Nanoscale **7**, 8261 (2015).

[73] Y. Yoon, K. Ganapathi, and S. Salahuddin, Nano Letters **11**, 3768 (2011).

[74] W. Cao, J. Kang, D. Sarkar, W. Liu, and K. Banerjee, IEEE Transactions on Electron Devices **62**, 3459 (2015).

[75] A. Ayari, E. Cobas, O. Ogundadegbe, and M. S. Fuhrer, Journal of Applied Physics **101**, 014507 (2007).

[76] R. Frisenda, A. J. Molina-Mendoza, T. Mueller, A. Castellanos-Gomez, and H. S. Van Der Zant, Chemical Society Reviews **47**, 3339 (2018).

[77] K. Novoselov, o. A. Mishchenko, o. A. Carvalho, and A. C. Neto, Science **353** (2016).

[78] F. Capasso, Science **235**, 172 (1987).

[79] M. Heiblum, M. Nathan, D. C. Thomas, and C. Knoedler, Physical Review Letters **55**, 2200 (1985).

[80] F. Capasso, S. Sen, A. Gossard, A. Hutchinson, and J. English, in *1986 International Electron Devices Meeting* (IEEE, 1986) pp. 282–285.

[81] S. S. Iyer, G. L. Patton, J. M. Stork, B. S. Meyerson, and D. L. Harame, IEEE Transactions on Electron Devices **36**, 2043 (1989).

[82] P. K. Sahoo, S. Memaran, Y. Xin, L. Balicas, and H. R. Gutiérrez, Nature **553**, 63 (2018).

[83] O. Ávalos-Ovando, D. Mastrogiuseppe, and S. E. Ulloa, Journal of Physics: Condensed Matter **31**, 213001 (2019).

[84] H. Taghinejad, A. A. Eftekhar, and A. Adibi, Optical Materials Express **9**, 1590 (2019).

[85] C. Zhang, M.-Y. Li, J. Tersoff, Y. Han, Y. Su, L.-J. Li, D. A. Muller, and C.-K. Shih, Nature Nanotechnology **13**, 152 (2018).

[86] S. Xie, L. Tu, Y. Han, L. Huang, K. Kang, K. U. Lao, P. Poddar, C. Park, D. A. Muller, R. A. DiStasio, *et al.*, Science **359**, 1131 (2018).

[87] R. Landauer, IBM Journal of Research and Development **1**, 223 (1957).

[88] R. Landauer, Philosophical Magazine **21**, 863 (1970).

[89] M. Büttiker, Y. Imry, R. Landauer, and S. Pinhas, Physical Review B **31**, 6207 (1985).

[90] M. Büttiker, Physical Review Letters **57**, 1761 (1986).

[91] S. Datta, *Quantum transport: atom to transistor* (Cambridge University Press, 2005).

[92] K. D. Sattler, *21st Century Nanoscience–A Handbook: Nanophysics Sourcebook (Volume One)* (CRC Press, 2019).

[93] M. L. Sancho, J. L. Sancho, J. L. Sancho, and J. Rubio, Journal of Physics F: Metal Physics **15**, 851 (1985).

[94] J. Velev and W. Butler, Journal of Physics: Condensed Matter **16**, R637 (2004).

[95] C. Caroli, R. Combescot, P. Nozieres, and D. Saint-James, Journal of Physics C: Solid State Physics **4**, 916 (1971).

[96] P. Hohenberg and W. Kohn, Physical Review **136**, B864 (1964).

[97] W. Kohn and L. J. Sham, Physical Review **140**, A1133 (1965).

[98] L. Kleinman and D. Bylander, Physical Review Letters **48**, 1425 (1982).

[99] G. B. Bachelet, D. R. Hamann, and M. Schlüter, Physical Review B **26**, 4199 (1982).

[100] T. Ozaki, Physical Review B **67**, 155108 (2003).

[101] T. Ozaki and H. Kino, Physical Review B **69**, 195113 (2004).

[102] T. Ozaki, Physical Review B **75**, 035123 (2007).

[103] A. Williams, P. J. Feibelman, and N. Lang, Physical Review B **26**, 5433 (1982).

[104] J. Taylor, H. Guo, and J. Wang, Physical Review B **63**, 245407 (2001).

[105] H. J. Monkhorst and J. D. Pack, Physical Review B **13**, 5188 (1976).

[106] T. Ozaki and H. Kino, Physical Review B **72**, 045121 (2005).

[107] M. Brandbyge, J.-L. Mozos, P. Ordejón, J. Taylor, and K. Stokbro, Physical Review B **65**, 165401 (2002).

[108] J. Schwinger, Journal of Mathematical Physics **2**, 407 (1961).

[109] L. P. Kadanoff and G. A. Baym, *Quantum Statistical Mechanics Green's Function Methods in Equilibrium Problems* (Benjamin, 1962).

[110] L. V. Keldysh *et al.*, Sov. Phys. JETP **20**, 1018 (1965).

[111] E. Marin, M. Perucchini, D. Marian, G. Iannaccone, and G. Fiori, IEEE Transactions on Electron Devices **65**, 4167 (2018).

[112] P. Miró, M. Audiffred, and T. Heine, Chemical Society Reviews **43**, 6537 (2014).

[113] J. C. Slater and G. F. Koster, Physical Review **94**, 1498 (1954).

[114] G.-B. Liu, W.-Y. Shan, Y. Yao, W. Yao, and D. Xiao, Physical Review B **88**, 085433 (2013).

[115] S. Fang, R. K. Defo, S. N. Shirodkar, S. Lieu, G. A. Tritsaris, and E. Kaxiras, Physical Review B **92**, 205108 (2015).

[116] A. N. Rudenko and M. I. Katsnelson, Physical Review B **89**, 201408 (2014).

[117] C.-C. Liu, H. Jiang, and Y. Yao, Physical Review B **84**, 195430 (2011).

[118] V. M. Pereira, A. C. Neto, and N. Peres, Physical Review B **80**, 045401 (2009).

[119] L. E. F. Torres, J.-C. Charlier, and S. Roche, *Introduction to graphene-based nanomaterials: from electronic structure to quantum transport*, Vol. 1 (Springer, 2013).

[120] P. R. Wallace, Physical Review **71**, 622 (1947).

[121] F. Bloch, Zeitschrift Für Physik **52**, 555 (1929).

[122] R. Deacon, K.-C. Chuang, R. Nicholas, K. Novoselov, and A. Geim, Physical Review B **76**, 081406 (2007).

[123] A. Lherbier, S. M.-M. Dubois, X. Declerck, Y.-M. Niquet, S. Roche, and J.-C. Charlier, Physical Review B **86**, 075402 (2012).

[124] N. Papior, sisl: v0.10.0 (2021).

[125] A. McMahan and J. Klepeis, Physical Review B **56**, 12250 (1997).

[126] R. Saito, M. Fujita, G. Dresselhaus, and M. S. Dresselhaus, Physical Review B **46**, 1804 (1992).

[127] J. P. Perdew, K. Burke, and M. Ernzerhof, Physical Review Letters **77**, 3865 (1996).

[128] N. Troullier and J. L. Martins, Physical Review **43**, 1991 (1993).

[129] M. Posternak, A. Baldereschi, A. Freeman, E. Wimmer, and M. Weinert, Physical Review Letters **50**, 761 (1983).

[130] C. H. Lewenkopf and E. R. Mucciolo, Journal of Computational Electronics **12**, 203 (2013).

[131] J. Yang, P. Hu, and G. Yu, APL Materials **7**, 020901 (2019).

[132] T. Cusati, G. Fiori, A. Gahoi, V. Passi, M. C. Lemme, A. Fortunelli, and G. Iannaccone, Scientific Reports **7**, 5109 (2017).

[133] G. Giovannetti, P. Khomyakov, G. Brocks, V. v. Karpan, J. Van den Brink, and P. J. Kelly, Physical Review Letters **101**, 026803 (2008).

[134] B. J. Schultz, R. V. Dennis, V. Lee, and S. Banerjee, Nanoscale **6**, 3444 (2014).

[135] P. Khomyakov, G. Giovannetti, P. Rusu, G. v. Brocks, J. Van den Brink, and P. J. Kelly, Physical Review B **79**, 195425 (2009).

[136] A. Gahoi, S. Kataria, F. Driussi, S. Venica, H. Pandey, D. Esseni, L. Selmi, and M. C. Lemme, Advanced Electronic Materials **6**, 2000386 (2020).

[137] F. Xia, V. Perebeinos, Y.-M. Lin, Y. Wu, and P. Avouris, Nat. Nanotechnol. **6**, 179 (2011).

[138] Q. Ran, M. Gao, X. Guan, Y. Wang, and Z. Yu, Applied Physics Letters **94**, 103511 (2009).

[139] C. Shen, J. Liu, N. Jiao, C. Zhang, H. Xiao, R. Wang, and L. Sun, Physics Letters A **378**, 1321 (2014).

[140] K. H. Khoo, W. S. Leong, J. T. Thong, and S. Y. Quek, ACS Nano **10**, 11219 (2016).

[141] S. Barraza-Lopez, M. Vanević, M. Kindermann, and M.-Y. Chou, Physical Review Letters **104**, 076807 (2010).

[142] J. Maassen, W. Ji, and H. Guo, Applied Physics Letters **97**, 142105 (2010).

[143] H. Liu, H. Kondo, and T. Ohno, Physical Review B **86**, 155434 (2012).

[144] B. Ma, C. Gong, Y. Wen, R. Chen, K. Cho, and B. Shan, Journal of Applied Physics **115**, 183708 (2014).

[145] K. Stokbro, M. Engelund, and A. Blom, Physical Review B **85**, 165442 (2012).

[146] H. Liu, H. Kondo, and T. Ohno, The Journal of Chemical Physics **139**, 074703 (2013).

[147] M. A. Kuroda, J. Tersoff, D. M. Newns, and G. J. Martyna, Nano Letters **11**, 3629 (2011).

[148] X. Zhu, S. Lei, S.-H. Tsai, X. Zhang, J. Liu, G. Yin, M. Tang, C. M. Torres Jr, A. Navabi, Z. Jin, *et al.*, Nano Letters **18**, 682 (2018).

[149] P. Blaha, K. Schwarz, G. K. Madsen, D. Kvasnicka, J. Luitz, *et al.*, Wien2k : An Augmented Plane Wave Plus Local Orbitals Program For Calculating Crystal Properties **60** (2001).

[150] S. Grimme, J. Antony, S. Ehrlich, and H. Krieg, The Journal of Chemical Physics **132**, 154104 (2010).

[151] L. Vitos, A. Ruban, H. L. Skriver, and J. Kollar, Surface Science **411**, 186 (1998).

[152] I. Y. Sahalianov, T. M. Radchenko, V. A. Tatarenko, G. Cuniberti, and Y. I. Prylutskyy, Journal of Applied Physics **126**, 054302 (2019).

[153] M. Chelvayohan and C. Mee, Journal of Physics C: Solid State Physics **15**, 2305 (1982).

[154] R. Eastment and C. Mee, Journal of Physics F: Metal Physics **3**, 1738 (1973).

[155] G. Hansson and S. Flodström, Physical Review B **18**, 1572 (1978).

[156] P. Gartland, S. Berge, and B. Slagsvold, Physical Review Letters **28**, 738 (1972).

[157] G. D. Kubiak, Journal of Vacuum Science & Technology A: Vacuum, Surfaces, and Films **5**, 731 (1987).

[158] J. Zheng, Y. Wang, L. Wang, R. Quhe, Z. Ni, W.-N. Mei, Z. Gao, D. Yu, J. Shi, and J. Lu, Scientific Reports **3**, 2081 (2013).

[159] L. Adamska, Y. Lin, A. J. Ross, M. Batzill, and I. I. Oleynik, Physical Review B **85**, 195443 (2012).

[160] I. Hamada and M. Otani, Physical Review B **82**, 153412 (2010).

[161] M. Vanin, J. J. Mortensen, A. Kelkkanen, J. M. Garcia-Lastra, K. S. Thygesen, and K. W. Jacobsen, Physical Review B **81**, 081408 (2010).

[162] B.-R. Wu, Applied Physics Letters **98**, 263107 (2011).

[163] E. McCann, D. S. Abergel, and V. I. Fal'ko, The European Physical Journal Special Topics **148**, 91 (2007).

[164] T. Olsen and K. S. Thygesen, Physical Review B **87**, 075111 (2013).

[165] M. Andersen, L. Hornekær, and B. Hammer, Physical Review B **86**, 085405 (2012).

[166] C. Gong, S. McDonnell, X. Qin, A. Azcatl, H. Dong, Y. J. Chabal, K. Cho, and R. M. Wallace, ACS Nano **8**, 642 (2014).

[167] M. Yang, Y. Liu, T. Fan, and D. Zhang, Progress in Materials Science **110**, 100652 (2020).

[168] F. A. Chaves, D. Jiménez, A. W. Cummings, and S. Roche, Journal of Applied Physics **115**, 164513 (2014).

[169] F. A. Chaves, D. Jiménez, A. A. Sagade, W. Kim, J. Riikonen, H. Lipsanen, and D. Neumaier, 2D Materials **2**, 025006 (2015).

[170] J. Wang and S.-Q. Wang, Surface Science **630**, 216 (2014).

[171] E. Rutkov, E. Afanaseva, and N. Gall, Diamond and Related Materials **101**, 107576 (2020).

[172] O. Leenaerts, B. Partoens, F. Peeters, A. Volodin, and C. Van Haesendonck, Journal of Physics: Condensed Matter **29**, 035003 (2016).

[173] M. Klintenberg, S. Lebegue, C. Ortiz, B. Sanyal, J. Fransson, and O. Eriksson, Journal of Physics: Condensed Matter **21**, 335502 (2009).

[174] R. S. Mulliken, The Journal of Chemical Physics **23**, 1833 (1955).

[175] G. Giovannetti, P. A. Khomyakov, G. Brocks, P. J. Kelly, and J. Van Den Brink, Physical Review B **76**, 073103 (2007).

[176] J. B. Oostinga, H. B. Heersche, X. Liu, A. F. Morpurgo, and L. M. Vandersypen, Nature Materials **7**, 151 (2008).

[177] C. Romero-Muñiz, A. Nakata, P. Pou, D. R. Bowler, T. Miyazaki, and R. Pérez, Journal of Physics: Condensed Matter **30**, 505901 (2018).

[178] A. Varykhalov and O. Rader, Physical Review B **80**, 035437 (2009).

[179] M. Gao, Y. Pan, C. Zhang, H. Hu, R. Yang, H. Lu, J. Cai, S. Du, F. Liu, and H.-J. Gao, Applied Physics Letters **96**, 053109 (2010).

[180] S. Zhang, D. He, P. Huang, and F. Wang, Materials & Design , 109509 (2021).

[181] S. Nie, N. C. Bartelt, J. M. Wofford, O. D. Dubon, K. F. McCarty, and K. Thürmer, Physical Review B **85**, 205406 (2012).

[182] A. Pálinkás, P. Süle, M. Szendrő, G. Molnár, C. Hwang, L. P. Biró, and Z. Osváth, Carbon **107**, 792 (2016).

[183] P. Süle, M. Szendrő, C. Hwang, and L. Tapasztó, Carbon **77**, 1082 (2014).

[184] Y. Murata, E. Starodub, B. Kappes, C. Ciobanu, N. Bartelt, K. McCarty, and S. Kodambaka, Applied Physics Letters **97**, 143114 (2010).

[185] J. Hulse, J. Küppers, K. Wandelt, and G. Ertl, Applications of Surface Science **6**, 453 (1980).

[186] S. Datta, *Electronic transport in mesoscopic systems* (Cambridge University Press, 1997).

[187] J. Cayssol, B. Huard, and D. Goldhaber-Gordon, Physical Review B **79**, 075428 (2009).

[188] F. A. Chaves, D. Jiménez, J. E. Santos, P. Bøggild, and J. M. Caridad, Nanoscale **11**, 10273 (2019).

[189] V. V. Cheianov and V. I. Fal'ko, Physical Review B **74**, 041403 (2006).

[190] P. E. Allain and J.-N. Fuchs, The European Physical Journal B **83**, 301 (2011).

[191] X. Ji, J. Zhang, Y. Wang, H. Qian, and Z. Yu, Physical Chemistry Chemical Physics **15**, 17883 (2013).

[192] V. Karpan, G. Giovannetti, P. Khomyakov, M. Talanana, A. Starikov, M. Zwierzycki, J. Van Den Brink, G. Brocks, and P. J. Kelly, Physical Review Letters **99**, 176602 (2007).

[193] C. Ma, H. Sun, Y. Zhao, B. Li, Q. Li, A. Zhao, X. Wang, Y. Luo, J. Yang, B. Wang, *et al.*, Physical Review Letters **112**, 226802 (2014).

[194] W. Liu, W. Cao, J. Kang, and K. Banerjee, ECS Transactions **58**, 281 (2013).

[195] W. Mehr, J. Dabrowski, J. C. Scheytt, G. Lippert, Y.-H. Xie, M. C. Lemme, M. Ostling, and G. Lupina, IEEE Electron Device Letters **33**, 691 (2012).

[196] S. Vaziri, G. Lupina, C. Henkel, A. D. Smith, M. Ostling, J. Dabrowski, G. Lippert, W. Mehr, and M. C. Lemme, Nano Letters **13**, 1435 (2013).

[197] R. Golizadeh-Mojarad and S. Datta, Physical Review B **79**, 085410 (2009).

[198] K. Stokbro, D. E. Petersen, S. Smidstrup, A. Blom, M. Ipsen, and K. Kaasbjerg, Physical Review B **82**, 075420 (2010).

[199] J. Bardeen, Physical Review Letters **6**, 57 (1961).

[200] C. J. Chen, *Introduction to scanning tunneling microscopy*, Vol. 4 (Oxford University Press on Demand, 1993).

[201] G. Reecht, C. Lotze, D. Sysoiev, T. Huhn, and K. J. Franke, ACS Nano **10**, 10555 (2016).

[202] E. Merzbacher, *Quantum Mechanics. John Wiley & Sons* (1998).

[203] L. Tai, D. Zhu, X. Liu, T. Yang, L. Wang, R. Wang, S. Jiang, Z. Chen, Z. Xu, and X. Li, Nano-Micro Letters **10**, 1 (2018).

[204] M. S. A. Bhuyan, M. N. Uddin, M. M. Islam, F. A. Bipasha, and S. S. Hossain, International Nano Letters **6**, 65 (2016).

[205] K. S. Novoselov, V. Fal, L. Colombo, P. Gellert, M. Schwab, K. Kim, *et al.*, Nature **490**, 192 (2012).

[206] A. Isacsson, A. W. Cummings, L. Colombo, L. Colombo, J. M. Kinaret, and S. Roche, 2D Materials **4**, 012002 (2016).

[207] K. Kim, Z. Lee, W. Regan, C. Kisielowski, M. Crommie, and A. Zettl, ACS Nano **5**, 2142 (2011).

[208] J. Lahiri, Y. Lin, P. Bozkurt, I. I. Oleynik, and M. Batzill, Nature Nanotechnology **5**, 326 (2010).

[209] A. Luican-Mayer, J. E. Barrios-Vargas, J. T. Falkenberg, G. Autès, A. W. Cummings, D. Soriano, G. Li, M. Brandbyge, O. V. Yazyev, S. Roche, *et al.*, 2D Materials **3**, 031005 (2016).

[210] J. C. Koepke, J. D. Wood, D. Estrada, Z.-Y. Ong, K. T. He, E. Pop, and J. W. Lyding, ACS Nano **7**, 75 (2013).

[211] H. Song, S. Li, H. Miyazaki, S. Sato, K. Hayashi, A. Yamada, N. Yokoyama, and K. Tsukagoshi, Scientific Reports **2**, 337 (2012).

[212] V. Kochat, C. S. Tiwary, T. Biswas, G. Ramalingam, K. Hsieh, K. Chattopadhyay, S. Raghavan, M. Jain, and A. Ghosh, Nano Letters **16**, 562 (2015).

[213] A. W. Tsen, L. Brown, M. P. Levendorf, F. Ghahari, P. Y. Huang, R. W. Havener, C. S. Ruiz-Vargas, D. A. Muller, P. Kim, and J. Park, Science **336**, 1143 (2012).

[214] S. Park, M. A. Shehzad, M. F. Khan, G. Nazir, J. Eom, H. Noh, and Y. Seo, Carbon **112**, 142 (2017).

[215] Q. Yu, L. A. Jauregui, W. Wu, R. Colby, J. Tian, Z. Su, H. Cao, Z. Liu, D. Pandey, D. Wei, *et al.*, Nature Materials **10**, 443 (2011).

[216] Y. Ogawa, K. Komatsu, K. Kawahara, M. Tsuji, K. Tsukagoshi, and H. Ago, Nanoscale **6**, 7288 (2014).

[217] A. Kumari, N. Prasad, P. Bhatnagar, P. Mathur, A. K. Yadav, C. Tomy, and C. Bhatia, Diamond and Related Materials **45**, 28 (2014).

[218] A. W. Cummings, D. L. Duong, V. L. Nguyen, D. Van Tuan, J. Kotakoski, J. E. Barrios Vargas, Y. H. Lee, and S. Roche, Advanced Materials **26**, 5079 (2014).

[219] D. Van Tuan, J. Kotakoski, T. Louvet, F. Ortmann, J. C. Meyer, and S. Roche, Nano Letters **13**, 1730 (2013).

[220] L. Banszerus, M. Schmitz, S. Engels, J. Dauber, M. Oellers, F. Haupt, K. Watanabe, T. Taniguchi, B. Beschoten, and C. Stampfer, Science Advances **1**, e1500222 (2015).

[221] H. Zhou, W. J. Yu, L. Liu, R. Cheng, Y. Chen, X. Huang, Y. Liu, Y. Wang, Y. Huang, and X. Duan, Nature Communications **4** (2013).

[222] O. V. Yazyev and S. G. Louie, Nature Materials **9**, 806 (2010).

[223] L. Tapasztó, P. Nemes-Incze, G. Dobrik, K. Jae Yoo, C. Hwang, and L. P. Biró, Applied Physics Letters **100**, 053114 (2012).

[224] J. Tersoff, Physical Review Letters **61**, 2879 (1988).

[225] L. Lindsay and D. Broido, Physical Review B **81**, 205441 (2010).

[226] G. Gottstein, *Physical foundations of materials science* (Springer Science & Business Media, 2013).

[227] O. V. Yazyev and S. G. Louie, Physical Review B **81**, 195420 (2010).

[228] H. Seung and D. R. Nelson, Physical Review A **38**, 1005 (1988).

[229] P. Simonis, C. Goffaux, P. Thiry, L. Biro, P. Lambin, and V. Meunier, Surface Science **511**, 319 (2002).

[230] P. Koskinen, S. Malola, and H. Häkkinen, Physical Review Letters **101**, 115502 (2008).

[231] J. Zhang and J. Zhao, Carbon **55**, 151 (2013).

[232] S. B. Kumar and J. Guo, Nano Letters **12**, 1362 (2012).

[233] V. H. Nguyen, T. X. Hoang, P. Dollfus, and J.-C. Charlier, Nanoscale **8**, 11658 (2016).

[234] J. Zhang, J. Gao, L. Liu, and J. Zhao, Journal of Applied Physics **112**, 053713 (2012).

[235] H. Zhang, G. Lee, C. Gong, L. Colombo, and K. Cho, The Journal of Physical Chemistry C **118**, 2338 (2014).

[236] T.-H. Liu, G. Gajewski, C.-W. Pao, and C.-C. Chang, Carbon **49**, 2306 (2011).

[237] A. Mesaros, S. Papanikolaou, C. Flipse, D. Sadri, and J. Zaanen, Physical Review B **82**, 205119 (2010).

[238] S. Ihnatsenka and I. Zozoulenko, Physical Review B **88**, 085436 (2013).

[239] F. Gargiulo and O. V. Yazyev, Nano Letters **14**, 250 (2013).

[240] K. W. Clark, X.-G. Zhang, I. V. Vlassiouk, G. He, R. M. Feenstra, and A.-P. Li, ACS Nano **7**, 7956 (2013).

[241] A. Capasso, E. Placidi, H. Zhan, E. Perfetto, J. M. Bell, Y. Gu, and N. Motta, Carbon **68**, 330 (2014).

[242] G.-D. Lee, C. Wang, E. Yoon, N.-M. Hwang, D.-Y. Kim, and K. Ho, Physical Review Letters **95**, 205501 (2005).

[243] B. Yang, H. Xu, J. Lu, and K. P. Loh, Journal of the American Chemical Society **136**, 12041 (2014).

[244] J.-C. Charlier, T. Ebbesen, and P. Lambin, Physical Review B **53**, 11108 (1996).

[245] R. Tamura and M. Tsukada, Physical Review B **49**, 7697 (1994).

[246] K. Xu, P. Cao, and J. R. Heath, Nano Letters **9**, 4446 (2009).

[247] M. Seifert, J. E. Vargas, M. Bobinger, M. Sachsenhauser, A. W. Cummings, S. Roche, and J. A. Garrido, 2D Materials **2**, 024008 (2015).

[248] K. Kaasbjerg, K. S. Thygesen, and K. W. Jacobsen, Physical Review B **85**, 115317 (2012).

[249] W. Zhang, Z. Huang, W. Zhang, and Y. Li, Nano Research **7**, 1731 (2014).

[250] B. Radisavljevic, A. Radenovic, J. Brivio, V. Giacometti, and A. Kis, Nature Nanotechnology **6**, 147 (2011).

[251] S. Bertolazzi, J. Brivio, and A. Kis, ACS Nano **5**, 9703 (2011).

[252] K. E. Petersen, Proceedings of the IEEE **70**, 420 (1982).

[253] R. Roldán, A. Castellanos-Gomez, E. Cappelluti, and F. Guinea, Journal of Physics: Condensed Matter **27**, 313201 (2015).

[254] S. Deng, A. V. Sumant, and V. Berry, Nano Today **22**, 14 (2018).

[255] M. Ghorbani-Asl, S. Borini, A. Kuc, and T. Heine, Physical Review B **87**, 235434 (2013).

[256] M. Hosseini, M. Elahi, M. Pourfath, and D. Esseni, IEEE Transactions on Electron Devices **62**, 3192 (2015).

[257] A. Sengupta, R. K. Ghosh, and S. Mahapatra, IEEE Transactions on Electron Devices **60**, 2782 (2013).

[258] S. Mohammad Tabatabaei, M. Noei, K. Khaliji, M. Pourfath, and M. Fathipour, Journal of Applied Physics **113**, 163708 (2013).

[259] N. Harada, S. Sato, and N. Yokoyama, Journal of Applied Physics **115**, 034505 (2014).

[260] K. L. Seyler, D. Zhong, B. Huang, X. Linpeng, N. P. Wilson, T. Taniguchi, K. Watanabe, W. Yao, D. Xiao, M. A. McGuire, *et al.*, Nano Letters **18**, 3823 (2018).

[261] E. Calman, M. Fogler, L. Butov, S. Hu, A. Mishchenko, and A. Geim, Nature Communications **9**, 1 (2018).

[262] Y. Cao, V. Fatemi, S. Fang, K. Watanabe, T. Taniguchi, E. Kaxiras, and P. Jarillo-Herrero, Nature **556**, 43 (2018).

[263] A. K. Geim and I. V. Grigorieva, Nature **499**, 419 (2013).

[264] X. Ling, Y. Lin, Q. Ma, Z. Wang, Y. Song, L. Yu, S. Huang, W. Fang, X. Zhang, A. L. Hsu, *et al.*, Advanced Materials **28**, 2322 (2016).

[265] Y. Gong, J. Lin, X. Wang, G. Shi, S. Lei, Z. Lin, X. Zou, G. Ye, R. Vajtai, B. I. Yakobson, *et al.*, Nature Materials **13**, 1135 (2014).

[266] C. Huang, S. Wu, A. M. Sanchez, J. J. Peters, R. Beanland, J. S. Ross, P. Rivera, W. Yao, D. H. Cobden, and X. Xu, Nature Materials **13**, 1096 (2014).

[267] X. Duan, C. Wang, J. C. Shaw, R. Cheng, Y. Chen, H. Li, X. Wu, Y. Tang, Q. Zhang, A. Pan, *et al.*, Nature Nanotechnology **9**, 1024 (2014).

[268] M.-Y. Li, Y. Shi, C.-C. Cheng, L.-S. Lu, Y.-C. Lin, H.-L. Tang, M.-L. Tsai, C.-W. Chu, K.-H. Wei, J.-H. He, *et al.*, Science **349**, 524 (2015).

[269] J. P. Perdew, International Journal of Quantum Chemistry **28**, 497 (1985).

[270] D. Çakır, F. M. Peeters, and C. Sevik, Applied Physics Letters **104**, 203110 (2014).

[271] N. Wakabayashi, H. Smith, and R. Nicklow, Physical Review B **12**, 659 (1975).

[272] W. Schutte, J. De Boer, and F. Jellinek, Journal of Solid State Chemistry **70**, 207 (1987).

[273] C. Zhang, C. Gong, Y. Nie, K.-A. Min, C. Liang, Y. J. Oh, H. Zhang, W. Wang, S. Hong, L. Colombo, *et al.*, 2D Materials **4**, 015026 (2016).

[274] H. M. Hill, A. F. Rigosi, K. T. Rim, G. W. Flynn, and T. F. Heinz, Nano Letters **16**, 4831 (2016).

[275] M.-H. Chiu, C. Zhang, H.-W. Shiu, C.-P. Chuu, C.-H. Chen, C.-Y. S. Chang, C.-H. Chen, M.-Y. Chou, C.-K. Shih, and L.-J. Li, Nature Communications **6**, 1 (2015).

[276] T. Cheiwchanchamnangij and W. R. Lambrecht, Physical Review B **85**, 205302 (2012).

[277] D. Xiao, G.-B. Liu, W. Feng, X. Xu, and W. Yao, Physical Review Letters **108**, 196802 (2012).

[278] X.-Q. Zhang, C.-H. Lin, Y.-W. Tseng, K.-H. Huang, and Y.-H. Lee, Nano Letters **15**, 410 (2015).

[279] Y. Kobayashi, S. Yoshida, M. Maruyama, H. Mogi, K. Murase, Y. Maniwa, O. Takeuchi, S. Okada, H. Shigekawa, and Y. Miyata, ACS Nano **13**, 7527 (2019).

[280] J. Kang, S. Tongay, J. Zhou, J. Li, and J. Wu, Applied Physics Letters **102**, 012111 (2013).

[281] W. Wei, Y. Dai, C. Niu, and B. Huang, Scientific Reports **5**, 1 (2015).

[282] W. Wei, Y. Dai, Q. Sun, N. Yin, S. Han, B. Huang, and T. Jacob, Physical Chemistry Chemical Physics **17**, 29380 (2015).

[283] T. Ghani, M. Armstrong, C. Auth, M. Bost, P. Charvat, G. Glass, T. Hoffmann, K. Johnson, C. Kenyon, J. Klaus, *et al.*, in *IEEE International Electron Devices Meeting 2003* (IEEE, 2003) pp. 11–6.

[284] M. Chu, Y. Sun, U. Aghoram, and S. E. Thompson, Annual Review of Materials Research **39**, 203 (2009).

[285] H. J. Conley, B. Wang, J. I. Ziegler, R. F. Haglund Jr, S. T. Pantelides, and K. I. Bolotin, Nano Letters **13**, 3626 (2013).

[286] R. Schmidt, I. Niehues, R. Schneider, M. Drueppel, T. Deilmann, M. Rohlfing, S. M. De Vasconcellos, A. Castellanos-Gomez, and R. Bratschitsch, 2D Materials **3**, 021011 (2016).

[287] K. Alam, Micro & Nano Letters **15**, 81 (2020).

[288] L. Lucchesi, G. Calogero, G. Fiori, and G. Iannaccone, Physical Review Research **3**, 023158 (2021).

[289] J. Choukroun, M. Pala, S. Fang, E. Kaxiras, and P. Dollfus, Nanotechnology **30**, 025201 (2018).

[290] E. G. Marin, D. Marian, M. Perucchini, G. Fiori, and G. Iannaccone, ACS Nano **14**, 1982 (2020).

[291] S. Fang, S. Carr, M. A. Cazalilla, and E. Kaxiras, Physical Review B **98**, 075106 (2018).

[292] E. S. Kadantsev and P. Hawrylak, Solid State Communications **152**, 909 (2012).

[293] L. Wang, A. Kutana, and B. I. Yakobson, Annalen der Physik **526**, L7 (2014).

[294] N. Maand D. Jena, 2D Materials **2**, 015003 (2015).

[295] J. Ye, Y. J. Zhang, R. Akashi, M. S. Bahramy, R. Arita, and Y. Iwasa, Science **338**, 1193 (2012).

[296] P. Zhao, J. Yu, H. Zhong, M. Rösner, M. I. Katsnelson, and S. Yuan, New Journal of Physics **22**, 083072 (2020).

[297] H. Fang, M. Tosun, G. Seol, T. C. Chang, K. Takei, J. Guo, and A. Javey, Nano Letters **13**, 1991 (2013).

[298] A. E. Maniadaki, G. Kopidakis, and I. N. Remediakis, Solid State Communications **227**, 33 (2016).

[299] T. Shen, A. V. Penumatcha, and J. Appenzeller, ACS Nano **10**, 4712 (2016).

[300] A. Kormányos, G. Burkard, M. Gmitra, J. Fabian, V. Zólyomi, N. D. Drummond, and V. Fal'ko, 2D Materials **2**, 022001 (2015).

[301] L. Liu, S. B. Kumar, Y. Ouyang, and J. Guo, IEEE Transactions on Electron Devices **58**, 3042 (2011).

[302] D. Logoteta, J. Cao, M. Pala, P. Dollfus, Y. Lee, and G. Iannaccone, Physical Review Research **2**, 043286 (2020).

[303] D. Jariwala, T. J. Marks, and M. C. Hersam, Nature Materials **16**, 170 (2017).

[304] S. Manzeli, A. Allain, A. Ghadimi, and A. Kis, Nano Letters **15**, 5330 (2015).

[305] Y. Yang, W.-H. Fang, and R. Long, The Journal of Physical Chemistry Letters **8**, 5771 (2017).

[306] Z. Cao, M. Harb, S. Lardhi, and L. Cavallo, The Journal of Physical Chemistry Letters **8**, 1664 (2017).

[307] D. Neumaier, S. Pindl, and M. C. Lemme, Nature Materials **18**, 525 (2019).

[308] S.-H. Bae, H. Kum, W. Kong, Y. Kim, C. Choi, B. Lee, P. Lin, Y. Park, and J. Kim, Nature Materials **18**, 550 (2019).

[309] T. Wu, X. Zhang, Q. Yuan, J. Xue, G. Lu, Z. Liu, H. Wang, H. Wang, F. Ding, Q. Yu, *et al.*, Nature Materials **15**, 43 (2016).

[310] Y. S. Kim, K. Joo, S.-K. Jerng, J. H. Lee, D. Moon, J. Kim, E. Yoon, and S.-H. Chun, ACS Nano **8**, 2230 (2014).

[311] J. Li, Q. Guo, N. Zhang, S. Yang, Z. Liu, A. Xu, W. Tao, G. Wang, D. Chen, and G. Ding, Journal of Materials Chemistry C **6**, 9682 (2018).

[312] J. Ryu, Y. Kim, D. Won, N. Kim, J. S. Park, E.-K. Lee, D. Cho, S.-P. Cho, S. J. Kim, G. H. Ryu, *et al.*, ACS Nano **8**, 950 (2014).

[313] K. L. Grosse, V. E. Dorgan, D. Estrada, J. D. Wood, I. Vlassiouk, G. Eres, J. W. Lyding, W. P. King, and E. Pop, Applied Physics Letters **105**, 143109 (2014).

[314] V. Kochat, C. S. Tiwary, T. Biswas, G. Ramalingam, K. Hsieh, K. Chattopadhyay, S. Raghavan, M. Jain, and A. Ghosh, Nano Letters **16**, 562 (2016).

[315] T. Lehmann, D. A. Ryndyk, and G. Cuniberti, Physical Review B **92**, 035418 (2015).

[316] B. Mortazavi, M. Pötschke, and G. Cuniberti, Nanoscale **6**, 3344 (2014).

[317] K. R. Hahn, C. Melis, and L. Colombo, Carbon **96**, 429 (2016).

[318] A. Salehi-Khojin, D. Estrada, K. Y. Lin, M.-H. Bae, F. Xiong, E. Pop, and R. I. Masel, Advanced Materials **24**, 53 (2012).

[319] K. Nagashio, T. Nishimura, K. Kita, and A. Toriumi, in *2009 IEEE International Electron Devices Meeting (IEDM)* (Ieee, 2009) pp. 1–4.

[320] N. F. Thissen, R. H. Vervuurt, A. J. Mackus, J. J. Mulders, J.-W. Weber, W. M. Kessels, and A. A. Bol, 2D Materials **4**, 025046 (2017).

[321] M. T. Ghoneim, C. E. Smith, and M. M. Hussain, Applied Physics Letters **102**, 183115 (2013).

[322] A. Hsu, H. Wang, K. K. Kim, J. Kong, and T. Palacios, IEEE Electron Device Letters **32**, 1008 (2011).

[323] J. A. Robinson, M. LaBella, M. Zhu, M. Hollander, R. Kasarda, Z. Hughes, K. Trumbull, R. Cavalero, and D. Snyder, Applied Physics Letters **98**, 053103 (2011).

[324] O. Balci and C. Kocabas, Applied Physics Letters **101**, 243105 (2012).

[325] W. Li, Y. Liang, D. Yu, L. Peng, K. P. Pernstich, T. Shen, A. Hight Walker, G. Cheng, C. A. Hacker, C. A. Richter, *et al.*, Applied Physics Letters **102**, 183110 (2013).

[326] S. Gahng, C. Ho Ra, Y. Jin Cho, J. Ah Kim, T. Kim, and W. Jong Yoo, Applied Physics Letters **104**, 223110 (2014).

[327] J. T. Smith, A. D. Franklin, D. B. Farmer, and C. D. Dimitrakopoulos, ACS Nano **7**, 3661 (2013).

[328] L. Anzi, A. Mansouri, P. Pedrinazzi, E. Guerriero, M. Fiocco, A. Pesquera, A. Centeno, A. Zurutuza, A. Behnam, E. A. Carrion, *et al.*, 2D Materials **5**, 025014 (2018).

[329] A. D. Franklin, S.-J. Han, A. A. Bol, and V. Perebeinos, IEEE Electron Device Letters **33**, 17 (2011).

[330] H.-Y. Park, W.-S. Jung, D.-H. Kang, J. Jeon, G. Yoo, Y. Park, J. Lee, Y. H. Jang, J. Lee, S. Park, *et al.*, Advanced Materials **28**, 864 (2016).

[331] S. Wang, D. Mao, Z. Jin, S. Peng, D. Zhang, J. Shi, and X. Wang, Nanotechnology **26**, 405706 (2015).

[332] S. Venica, F. Driussi, A. Gahoi, P. Palestri, M. C. Lemme, and L. Selmi, IEEE Transactions on Electron Devices **65**, 1589 (2018).

[333] R. Kappera, D. Voiry, S. E. Yalcin, B. Branch, G. Gupta, A. D. Mohite, and M. Chhowalla, Nature Materials **13**, 1128 (2014).

[334] Z. Zhang, P. Chen, X. Duan, K. Zang, J. Luo, and X. Duan, Science **357**, 788 (2017).

[335] M.-L. Tsai, M.-Y. Li, J. R. D. Retamal, K.-T. Lam, Y.-C. Lin, K. Suenaga, L.-J. Chen, G. Liang, L.-J. Li, and J.-H. He, Advanced Materials **29**, 1701168 (2017).

[336] X. Chen, Y. Qiu, H. Yang, G. Liu, W. Zheng, W. Feng, W. Cao, W. Hu, and P. Hu, ACS Applied Materials & Interfaces **9**, 1684 (2017).

[337] Z. Zhang, Y. Xie, Q. Peng, and Y. Chen, Scientific Reports **6**, 1 (2016).

[338] H. Ghadiri and A. Saffarzadeh, Journal of Applied Physics **123**, 104301 (2018).

[339] J. Lee, J. Huang, B. G. Sumpter, and M. Yoon, 2D Materials **4**, 021016 (2017).

[340] Z.-Q. Fan, X.-W. Jiang, J.-W. Luo, L.-Y. Jiao, R. Huang, S.-S. Li, and L.-W. Wang, Physical Review B **96**, 165402 (2017).

[341] J.-W. Jiang, Acta Mechanica Solida Sinica **32**, 17 (2019).

[342] H. Qin, Q.-X. Pei, Y. Liu, and Y.-W. Zhang, Physical Chemistry Chemical Physics **21**, 15845 (2019).

[343] J. P. Perdew and W. Yue, Physical Review B **33**, 8800 (1986).

[344] B. Hammer, L. B. Hansen, and J. K. Nørskov, Physical review B **59**, 7413 (1999).